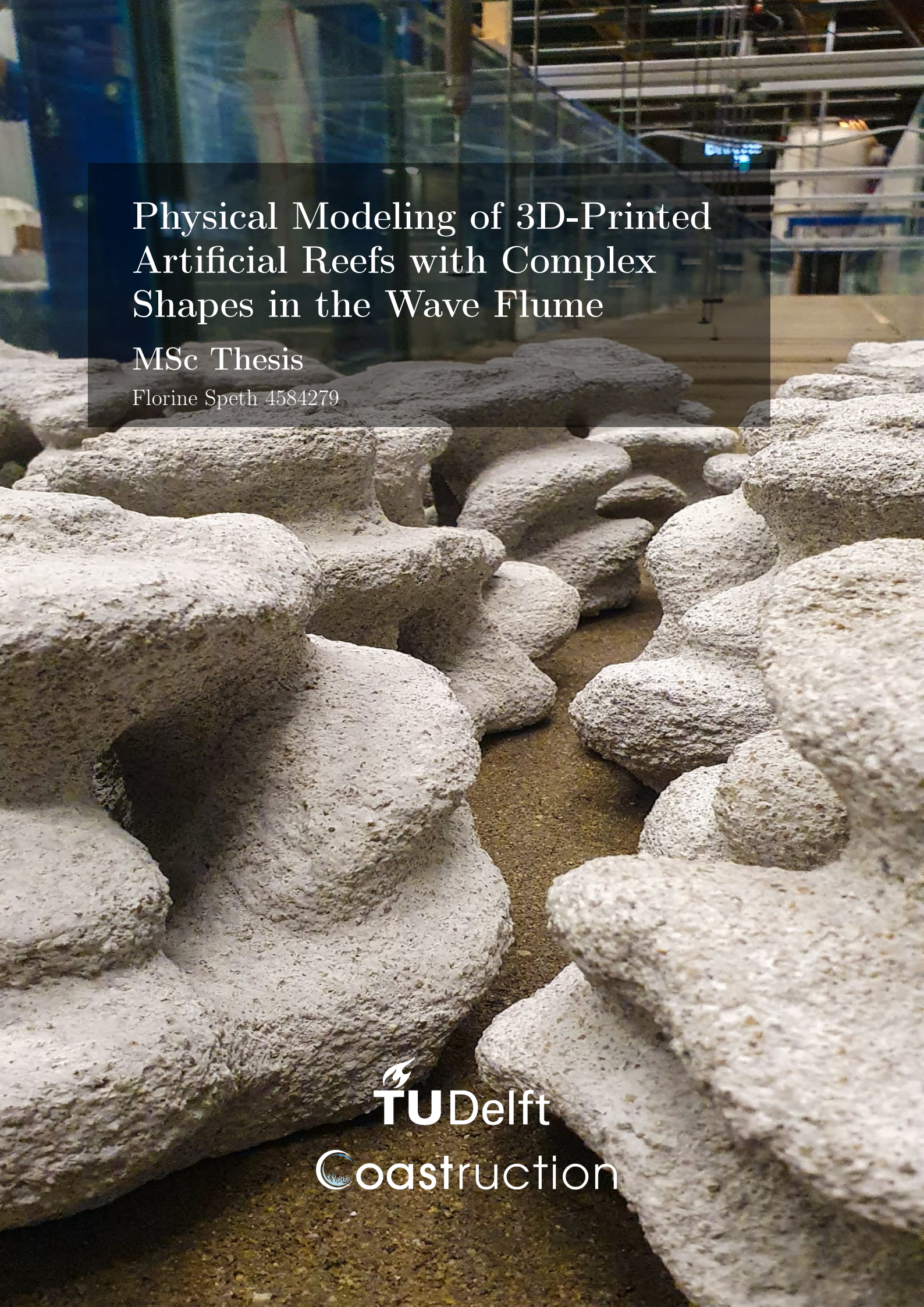

Physical Modeling of 3D-Printed Artificial Reefs with Complex Shapes in the Wave Flume

MSc Thesis

Florine Speth 4584279

TU Delft

Coastruction

Monday 1st May, 2023

Physical Modeling of 3D-Printed Artificial Reefs with Complex Shapes in the Wave Flume

MSc Thesis

Florine Speth 4584279

Delft University of Technology


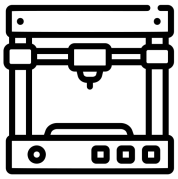


Thesis committee:

Dr. Marion Tissier	*TU Delft (Chair)*
Dr. ir. Alessandro Antonini	*TU Delft*
Prof. dr. ir. Marcel van Gent	*TU Delft, Deltares*
Dr. Nadia Fani	*Coastruction*

TU Delft Delft University of Technology

Coastruction

Acknowledgements

I would like to take this opportunity to express my sincere gratitude to the many people who have supported me throughout my master's thesis journey. First and foremost, I would like to thank Marion Tissier, the chair of my thesis committee, who has been an invaluable guide and mentor to me. Her weekly meetings and feedback kept me motivated and steered me in the right direction for the past 8 months. I would also like to extend my appreciation to Marcel van Gent, a thesis committee member who works for Deltares. Marcel was a great asset in the initial planning and design stages of the experiments, and his expertise was instrumental in shaping the direction of my research. And of course thank you Alessandro Antonini, the third member of my thesis committee, who alway asked critical questions during our meetings, helping me to improve and ensuring that no detail was left behind.

I am especially grateful to Nadia Fani, founder of Coastruction, who provided me with the opportunity to perform my thesis at her company. Nadia made me feel comfortable and was always enthusiastic about my work. Her trust in my abilities helped me become more secure in my decision-making. She also provided me with invaluable support throughout the entire thesis process, and connected me with her network to help me further my research.

I would also like to thank Astrid Kramer, who worked for Coastruction during the first part of my thesis and taught me a great deal about corals and their great importance. Andries Koopmans, lead engineer at Coastruction, provided me with tremendous help during the preparation phase of the experiments. His support with 3D-printing during my time at Coastruction was greatly appreciated.

Next I would like to extend my gratitude to Alex Capel and Vera van Bergeijk, employees from Deltares, for their expertise in the field of physical modeling and providing feedback and improvements to my test setup. I am also grateful to them for allowing me, on behalf of Coastruction, to stay longer than two weeks in the test facility, which enabled me to obtain more data.

Then I would like to thank David Lennon, an expert in the design of artificial reefs and reef layouts from Australia, for his assistance with the design of the artificial reefs. Even with the time difference, we managed to have productive discussions in the initial phase of my thesis. Lastly, I would like to thank Paolo Carboni, a civil engineer from Italy, for his expertise in the development of parametric algorithms which are essential for creating modular artificial coral reefs. His help with the computational design of the structures was invaluable.

To everyone who supported me during the last 8 months, thank you for being there for me throughout this challenging but rewarding experience. Without the guidance and support of these individuals, my thesis would not have been possible. I am very grateful for their contributions and will cherish their help in this great milestone in my academic journey.

Florine Speth,
1 May 2023

Abstract

Coral reefs are considered to be a crucial ecosystem and form of natural coastal protection. They owe their effectiveness to their high structural complexity. This complexity, which positively influences aspects like species richness, coral recovery, live coral cover, and coastal protection, is often quantified using parameters such as porosity and rugosity as has been done in this thesis. However, coral reefs are currently facing decline due to both natural processes and human activities. To address this issue, artificial reefs (ARs) have been proposed as a potential solution. Coastruction, a start-up specializing in 3D printing, has developed a 3D printer capable of creating artificial reefs in any shape. In this thesis, biomimicry-inspired complex ARs were designed and printed to examine the impact of structural complexity on wave attenuation.

Data was collected through physical model tests in a wave flume at Deltares, using Froude scaling with a length scale of n_L=4. The experiments involved 1 to 2-meter-long reefs composed of three distinct structures with different geometrical complexity levels: design 1 (medium complexity), design 2 (maximum complexity), and cubes (low complexity). These structures were tested under similar, primarily non-breaking wave conditions. The aim was to determine if the dissipation observed resulted from friction rather than wave breaking.

The results of the conducted experiments showed that structural complexity does not significantly affect wave transmission. Overall, high transmission coefficient were observed across the different structures, ranging from 0.96-0.99. Additionally, no significant differences in dissipation were found among the three structure types, with dissipation ranging from 5.5% to 13.5% of the incoming wave energy. However, increased reef coverage positively impacts transmission reduction and spectral wave dissipation, exhibiting a linear decrease in transmission coefficients and a simultaneous increase in dissipation.

In summary, the various artificial reefs examined in this study demonstrated minimal effectiveness in wave attenuation, with negligible differences among reefs featuring different degrees of structural complexity. Despite the similar wave attenuation effects, the environmental benefits of a highly structurally complex reef suggest that it should be considered a viable solution.

Table of contents

1 Introduction **2**
- 1.1 Research motivation and relevance . . . 2
- 1.2 Coastruction . . . 2
- 1.3 Objectives . . . 3
- 1.4 Research questions . . . 3
- 1.5 Chapter content . . . 4

2 Literature **5**
- 2.1 Coral reefs in nature . . . 5
  - 2.1.1 Maldives wave climate and morphology . . . 6
  - 2.1.2 Structural complexity of coral reefs . . . 7
  - 2.1.3 Quantification of structural complexity . . . 9
- 2.2 Artificial reefs and submerged breakwaters . . . 10
  - 2.2.1 Wave transmission over submerged structures . . . 11
  - 2.2.2 Existing empirical formula . . . 12
- 2.3 Hydrodynamic processes at (artificial) reefs . . . 15

3 Physical model **18**
- 3.1 Experimental set-up . . . 18
  - 3.1.1 Properties of the Scheldt flume . . . 18
  - 3.1.2 Foreshore . . . 18
  - 3.1.3 Measuring devices . . . 19
- 3.2 Scaling . . . 21
- 3.3 Reef structures . . . 22
  - 3.3.1 Element designs . . . 22
  - 3.3.2 Reef configurations . . . 23
- 3.4 Wave conditions . . . 24

4 Data Processing and Extraction Techniques **27**
- 4.1 Pre-processing and spectral characteristics . . . 27
- 4.2 Decomposition methods . . . 28
  - 4.2.1 Co-located decomposition . . . 28
  - 4.2.2 Least square method . . . 29
  - 4.2.3 Comparison of decomposition methods . . . 30
- 4.3 Parameter definition . . . 32
  - 4.3.1 Normalized Transmission Coefficient . . . 32
  - 4.3.2 Relative dissipation . . . 33

5 Data Analysis **35**
- 5.1 Wave transformation in the empty flume . . . 35
- 5.2 Wave transmission over the artificial reef . . . 37
  - 5.2.1 Overall comparison of Transmission coefficient . . . 38
  - 5.2.2 Relative water depth . . . 39
  - 5.2.3 Incoming wave steepness . . . 39
  - 5.2.4 Relative reef length . . . 40
  - 5.2.5 Reef set-up/density . . . 41
  - 5.2.6 Combining wave parameters . . . 41
  - 5.2.7 Summary wave transmission . . . 42
- 5.3 Spectral evolution and dissipation . . . 43
  - 5.3.1 Overall comparison of spectral dissipation . . . 43
  - 5.3.2 Analysis characteristic wave periods . . . 44
  - 5.3.3 Influence of reef lay-out on spectral dissipation . . . 47

5.3.4 Summary spectral evolution and dissipation 49

6 Discussion **51**
6.1 Physical model 51
6.2 Wave theory approximation 51
6.3 Data analysis 52
6.3.1 Comparison with existing empirical formulae 52
6.3.2 Empty flume dissipation 54
6.3.3 Reflection coefficient 55
6.3.4 Consistency wave spectra 56
6.3.5 Evolution of characteristic wave periods and wave run-up 58

7 Conclusions and Recommendations **59**
7.1 Conclusions 59
7.2 Recommendations 62

A Foreshore assessment **69**

B Printing process **71**

C Test cases **73**

D Signal disturbance **75**

List of Figures

1.1 Overview of the different phases in this thesis 4

2.1 Visual representation of the three reef types 5
2.2 Reef zonation 5
2.3 Map of the Maldives 6
2.4 Overview of measured significant wave height H_s and peak period T_p values at reef flat of Maldives 7
2.5 Meta-analysis results from study performed by Ferrario et al. (2014) 9
2.6 Visualisation of chain-tape method (Walbridge et al., 2018) 10
2.7 Few examples of the many artificial reefs 11
2.8 Definition sketch of the important transmission parameters over breakwaters. (Brancasi et al., 2022) 12

3.1 Definition sketch, including axis orientation. Note that the sketch is not to scale. 18
3.2 Experimental set-up of the physical model in the wave flume, including foreshore dimensions and instrumentation positions in x and y dimensions. 19
3.3 Detail sketches of Figure 3.2. Units are in metres 19
3.4 Visualisations of the two geometrical complex designs and cube. 22
3.5 Visualisations of the various reef lay-out as used in the experiments. 23
3.6 Pictures of the reef lay-out in the Scheldt flume at Deltares. 24

4.1 Two scatter plots of the incoming significant wave height (H_s) and the transmission coefficient (K_T) decomposed using two different decomposition methods. 31

5.1 Wave spectra at location 2 and 3 of a breaking and non-breaking test case. 35
5.2 Scatter plot of the total and the incoming significant wave height along the wave flume for a breaking and a non-breaking test case. 36
5.3 Wave set-up and set-down along the wave flume for a breaking and a non-breaking test case. 36
5.4 Root mean square orbital velocity $U^{rms}(z)$ along the wave flume for a breaking and a non-breaking test case. 37
5.5 Box-plot of the transmission coefficient K_T and the normalised transmission coefficient $K_{T,norm}$ corresponding to the seven non-breaking test cases. Distinguishing between the three structure types (D1, D2, C1) and the reference tests (C0). 38
5.6 Influence of the relative water depth on the normalised wave transmission coefficient ($K_{T,norm}$) depicting the three different structures: Design 1, Design 2, Cubes. 39
5.7 Influence of the incoming wave steepness on the wave transmission coefficient (K_T) depicting the three different structures: Design 1, Design 2, Cubes. 40
5.8 Influence of the relative reef length on the wave transmission coefficient (K_T) depicting the three different structures: Design 1, Design 2, Cubes. 40
5.9 Influence of the reef coverage on the normalised wave transmission coefficient (K_T) depicting two different wave conditions. 41
5.10 The effect of wave steepness H_s/L and relative water depth h/H_s on the normalized transmission coefficient K_T for the three structure types: design 1, design 2 and cubes . 42
5.11 Box-plot of the energy dissipation and the relative energy dissipation corresponding to the seven non-breaking test cases. Distinguishing between the three structure types (D1, D2, C1) and the reference tests (C0). 43
5.12 Bar chart of the relative dissipation of all seven non-breaking test cases per structure type: Design 1, design 2, cubes and empty flume. 44
5.13 Plot of the incident energy density spectra at location 2 and 3 per structure type: D1 , D2, C1 and the reference case C0 for test case h70H5T5. 45

5.14 Plot of the incident energy density spectra at location 2 and 3 per structure type: D1, D2, C1 and the reference case C0 for test case h80H10T25. 46
5.15 Scatter plot of the transmitted (i.e. at location 3) mean energy period of a specific structure ($T_{m_{-1,0}(structure)}$) divided by the mean energy period of the corresponding reference test ($T_{m_{-1,0}(empty)}$) versus the relative spectral dissipation for the seven non-breaking test cases. And corresponding box plot depicting the range of the scatter. 47
5.16 Energy density spectra at location 3 of decreasing reef coverage: RL8-D12-A=100%, RL8-D12-B=62.5%, and RL8-D12-C=31.25%. Corresponding to test case h80H10T25, and h70H5T5, including mean energy periods ($T_{m_{-1,0}}$). 48
5.17 Figure showing the relationship between relative dissipation and reef coverage for two distinct test cases, namely h70H5T5 and h80H10T25. 49

6.1 Comparison of calculated K_T values using the empirical formula from Seabrook & Hall (1998) and measured normalised K_T, showing the scatter and a plot of K_T with respect to h/Hs. 53
6.2 Figure indicating the distribution of the empty flume dissipation along with the measured root mean square orbital velocity in the flume. 54
6.3 Reflection coefficient at location 2 for all seven non-breaking cases, of the three structures: Design 1 (D1), Design 2 (D2) and cubes (C1). As well as the empty flume (C0) 56
6.4 Normalised transmission coefficient for all seven non-breaking test cases, of the three structures: Design 1 (D1), Design 2 (D2) and cubes (C1). 56
6.5 Plot of the reflection coefficient values at location 2 $K_{R,2}$ with respect to the relative reef length B/L. Corresponding to test case h80H10T25. 57
6.6 Incident energy density spectrum of 7 different reef lay-outs at location 2 corresponding to test case h80H10T25 ($R_c = 0.25m$, $H_s = 0.09m$, $T_p = 2.5s$). Including Energy flux ($F_2 = C_g E$) 57
6.7 Incident energy density spectrum of 7 different reef lay-outs at location 2 corresponding to test case h70H5T5 ($R_c = 0.15m$, $H_s = 0.05m$, $T_p = 5s$). Including Energy flux ($F_2 = C_g E$) 58

A.1 Plots of Ursell values to peak period (Tp), displaying the possible Tp values for different foreshore height (h_{FS}) and water depth (h) combinations. The water depth above the foreshore is equal to 0.3 m in all situations. 69
A.2 Plot of significant wave height (H_s) for different wave conditions with a foreshore slope of 1:1 and 1:10. 70

B.1 Figure depicting the different steps per layer. (a) the material is lowered, creating space for new dry material, (b) new material being deposited on the top layer, (c) the nozzle precisely deposited water at the area of interest, (d) the bottom is lowered, so the process can be repeated from (a). 71
B.2 Printing process showing one layer of water deposited in the specific shape. 72
B.3 Pictures depicting the result of the cleaning process of the structures from beginning (a) to end (c). 72

D.1 Water surface elevation time series of the group of four wave gauges located at location 3: WHM11, WHM12, WHM93, WHM13. Only showing a short time range. The signals are obtained from the empty flume test case with wave condition label h80H22T25 . . . 75

List of Tables

2.1 Wave characteristics and structural parameters as found in Figure 2.8 13

3.1 Froude scale factors for commonly used variables. 21
3.2 Porosity and rugosity values of the two structural complex designs 23
3.3 Overview of the wave conditions that have been performed in this study. 26

5.1 Overview of wave conditions corresponding to the seven non-breaking test cases. 38
5.2 Difference of mean wave period $\Delta T_{m_{0,1}}$ and mean energy period $\Delta T_{m_{-1,0}}$. Corresponding to test case h70H5T5. 45
5.3 Difference of mean wave period $\Delta T_{m_{0,1}}$ and mean energy period $\Delta T_{m_{-1,0}}$. Corresponding to test case h80H10T25. 46

7.1 Structural complexity parameters of the two designs 60

C.1 Overview of the wave conditions for all test cases as applied in the steering file for the wave paddle, with a total of 47 tests. Crest submergence: R_c, Significant wave height H_s, peak period T_p, structure C0: empty flume, D1: design 1, D2: design 2, C1: cubes . 74

List of symbols

$()^*$	Complex conjugate of the enclosed quantity
α	Structure seaward slope
$\epsilon_{f,j}$	Rate of dissipation due to bottom friction
$\epsilon_{j,p}$	Error in matching the jth Fourier coefficient $A_{j,p}$ at wave gauge p
η	Water surface elevation
$\eta_p(t)$	Surface elevation time series at wave gauge p
γ	Breaker parameter
ω	Angular frequency
ω_j	Wave radian frequency corresponding to the jth frequency component
ω_r	Representative wave radian frequency
$\overline{\eta}$	Set-up/down
ϕ_j	phase angle between the bottom shear stress and the near-bed horizontal orbital velocity corresponding to the jth frequency component
$\phi_{j,p}$	Absolute phase corresponding to the jth frequency component
ρ	Density
ξ	Iribarren number
$A_{j,p}$	Fourier coefficient for amplitude for the jth frequency
a_{Lj}	Amplitude of left traveling wave corresponding to the jth frequency component
a_{Rj}	Amplitude of right traveling wave corresponding to the jth frequency component
B	Crest width
B_{eff}	Relative crest width
c_g	Group velocity
$c_{g,j}$	Group velocity corresponding to the jth frequency component
D_{eff}	Effective diameter
D_{n50}	Nominal armor diameter
$E(f)$	Variance density spectrum
E_f	Wave energy flux
E_{energy}	Energy density spectrum
F	Energy flux for the full spectrum
f	Frequency
f_e	Energy dissipation factor
F_i	Incident energy flux for the full spectrum
F_j	Energy flux corresponding to the jth frequency component
F_r	Reflected energy flux for the full spectrum
F_u	Complex Fourier components of velocity component
f_w	Wave friction factor
F_η	Complex Fourier components of water elevation
$f_{e,j}$	Energy dissipation factor corresponding to the jth frequency component
$f_{e,r}$	Representative energy dissipation factor
$f_{w,j}$	Wave friction factor corresponding to the jth frequency component

$f_{w,r}$	Representative wave friction factor
g	Gravitational acceleration
h	Still water depth
h_c	Structure height
h_c	Water depth at the toe of the structure
H_i	Incident wave height
H_s	Significant wave height
H_t	Transmitted wave height
h_u	Height above the bed where the velocity is measured
$H_{s,i,2}$	Incoming significant wave height at location 2
$H_{s,i,3}$	Incoming significant wave height at location 3
K_T	Transmission coefficient
K_u	Velocity response function
k_w	hydraulic roughness length
$K_{R,2}$	Reflection coefficient at location2
K_R	Reflection coefficient
$k_{shoaling}$	Shoaling coefficient
$K_{T,norm}$	Normalised transmission coefficient
L_{op}	Local wave length
m_0	Variance of the water surface elevation
m_n	The n^{th} moment of the variance density spectrum
n	Porosity
n_L	Length scale parameter
N_{max}	Maximum amount of structures that could fill that stretch of the reef
$N_{structures}$	Number of structures
N_{Ursell}	Ursell number
R^2	Coefficient of determination
R_c	Crest freeboard
S	Wave steepness
T	Length of the total time series
t	Time
T_p	Peak wave period
$T_{m-1,0}$	Mean energy period
$T_{m0,1}$	Mean wave period
U	The amplitude of the bed velocity variations
$u(z)$	Orbital velocity at depth z
U^{rms}	Root-mean-square orbital velocities
$u_{b,j}$	Velocity corresponding to the jth frequency component
$u_{b,r}$	Maximum near-bed horizontal orbital velocity
V_o	Volume occupied by the length, width and height of the bounding box
V_t	Total volume of the structure

$W_{j,p}$	Weighting coefficient for wave gauge p at frequency j
z	z-coordinate
a	Amplitude
k	Wave number
x	x-coordinate
z	z-coordinate

Chapter 1 | Introduction

1.1 Research motivation and relevance

Coral reef communities are among the most important ecosystems on our planet, constituting a vital ecological resource (Sorokin, 2013), often referred to as the "rainforests of the sea". Although they only cover 0.2% of the ocean bed, they support an extraordinary variety of marine life, hosting approximately 25% of all marine life, thereby contributing significantly to global biodiversity. Coral reefs also provide critical economic and societal benefits, as research has estimated that they deliver a yearly net benefit income of nearly $30 billion through goods and services, including fishery, tourism, and coastal protection (Cesar et al., 2003). With almost 40% of the world's population residing within 100 km of the coast, as stated by Ferrario et al. (2014), these ecosystems hold immense value for both people and the environment. Thus their importance as an ecological, economic, and societal resource cannot be overstated.

However, these invaluable ecosystems are under severe threat. Over the past couple of years coral reefs have experienced alarming rates of decline due to natural processes, such as coastal storms, and anthropogenic causes, including increasing sea temperature. If the present rates of destruction persist, 60% of the world's coral reefs will be permanently lost within the next 30 years (Cesar et al., 2003). Although natural processes are beyond human control, anthropogenic causes can and should be mitigated. Examples of these factors include climate change, ocean acidification, overfishing, pollution, and destructive coastal development practices. Despite the need for drastic reductions in carbon emissions to avert an environmental catastrophe, the 2022 IPCC report states that the globe is expected to approach the 1.5 °C threshold over the next two decades, even with the most extreme emission reduction measures (Pörtner et al., 2022). The degradation of coral reefs not only affects marine biodiversity and the essential services they provide but also has profound implications for the well-being and prosperity of human societies that depend on them. As such, alternative solutions are necessary to help restore coral reefs and safeguarding these essential ecosystems for future generations. One potential solution for addressing the decline of coral reefs is the implementation of artificial reefs

(ARs), which have been extensively designed and researched to facilitate the restoration of these valuable ecosystems. ARs promote the regrowth of natural corals on artificial structures, typically constructed of concrete. In addition to supporting coral reef restoration, ARs also serve as an effective form of coastal protection by dissipating a significant portion of energy from incoming waves, much like breakwaters. Notably, (Ferrario et al., 2014) demonstrated that, on average, the costs associated with coral restoration projects using ARs were considerably lower than those incurred while constructing tropical breakwaters. Consequently, artificial reefs may provide a cost-effective and environmentally sustainable approach to safeguarding both coastal areas and coral reefs, preserving the invaluable services they offer to the natural world and human society.

1.2 Coastruction

Coastruction, founded in 2021, is a startup that designs, produces, and installs 3D printed ARs as well as the 3D printers themselves. Because of the powder bed technology of the 3D printer, complex shapes can be produced, which is a key factor that distinguishes this company from other AR startups. The shape of the printed element is only limited by the maximum capacity of the material to hold its own weight, as well as the maximum resolution of the printer, which is 2.5mm. The printer uses local and raw materials for the fill material, such as local beach sand, dredged material, and recycled concrete. Subsequently, it is possible to use either seawater or freshwater as a liquid binder. This way, the supply chain is optimised by shortening transportation routes and reducing harmful emissions to the environment. Additionally, this optimization in the supply chain reduces the costs of 3D printing

as well.

As of this point, *Coastruction* owns a 3D printer that is able to print individual elements with dimensions of 25x25x15 cm (wxdxh). Note that this printer will be used in this research. However, the company is currently in the process of designing and producing a larger printer that is able to print individual elements up to one cubic meter (100x100x100 cm). For this research, it should be taken into account that in the near future, *Coastruction* will print with this larger printer, and thus the physical model in the flume should be scaled according to this parameter. In the far future, Coastruction will aim at producing a 3D printer that fits a sea container.

1.3 Objectives

This MSc thesis aims to investigate the influence of various artificial reefs, characterized by high structural complexity, on wave transmission and wave dissipation. The research will involve conducting physical experiments using wave flume models at Deltares, a world-renowned research facility. The primary objective of this study is to generate novel data that will help establish an optimal balance between enhancing biodiversity and effectively dissipating wave energy.

The artificial reefs considered in this research are comprised of elements inspired by biomimicry principles, ensuring that their shape and design closely resemble the structural complexity of natural habitats. This approach aims to improve the artificial reefs' ability to support biodiversity by emulating the intricate features and functions of natural ecosystems. By assessing the performance of these biomimetic artificial reefs, the study hopes to shed light on their potential as a viable solution for both coastal protection and coral reef restoration.

Through a comprehensive analysis of wave transmission and dissipation characteristics of these biomimetic artificial reefs, this research will provide valuable insights into their effectiveness in various scenarios. The findings can inform future design and implementation strategies for artificial reefs, ultimately contributing to the sustainable management and preservation of coral reef ecosystems and coastal areas worldwide.

1.4 Research questions

Taking into account the objective of this thesis, the main research question is:

What is the relationship between structural complexity of elements in artificial reefs and their effectiveness in dissipating and attenuating wave energy?

With the following sub-questions:

1. What is the added value of structural complexity in natural coral reefs, and how is it quantified?
2. On which hydrodynamic processes does the structural complexity of coral have an influence, and how can tests in a wave tank be best designed to investigate this?
3. In what way is the wave transmission influenced by different wave parameters and do the different structures show a different behaviour?
4. In what way is the wave transmission influenced by different reef set-ups?

5. How does the presence of different artificial reef structures affect the spectral evolution and dissipation?

6. How do various reef configurations influence the spectral evolution and dissipation under different wave conditions?

1.5 Chapter content

The second chapter of this thesis provides an overview of the relevant background and literature on the key concepts related to the research. Subsequently, in chapter three, the physical model set-up and all relevant details including the design and layout of the printed elements will be discussed in-depth. The fourth Chapter elaborates on the data processing steps that have been taken to analyse and clean up the data. Chapter five includes a quality control of the measured data, followed by an in depth analysis of the results of the physical model tests. Additionally, chapter six offers a comprehensive discussion of the findings. Finally, chapter seven provides conclusions that can be drawn based on the research presented in this thesis followed by recommendations for future research. Figure 1.1 provides a visual representation of the different phases that this thesis is organized into.

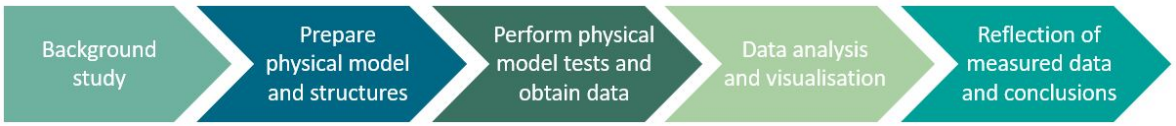

Figure 1.1: Overview of the different phases in this thesis

Chapter 2 | Literature

2.1 Coral reefs in nature

In nature, three different types of coral reef formations can be distinguished; fringing reefs, barrier reefs and atolls. Fringing reefs are most commonly found, and can morphologically be divided into three zones; forereef, reef crest, and reef flat or backreef. Because a fringing reef grows straight from the shoreline, the reef flat reaches all the way to the beach and there is no backreef. The barrier reef, just like the fringing reef, is also parallel to the coastline, however this reef is separated by a much deeper and wider lagoon. Finally, atolls are similar to barrier reefs, except at atolls the island is fully submerged due to either sinking of the land or rising sea levels. Atolls can be described as a ring-like shaped reef that encircles a lagoon. See Figure 2.1 for an overview of the three reef types.

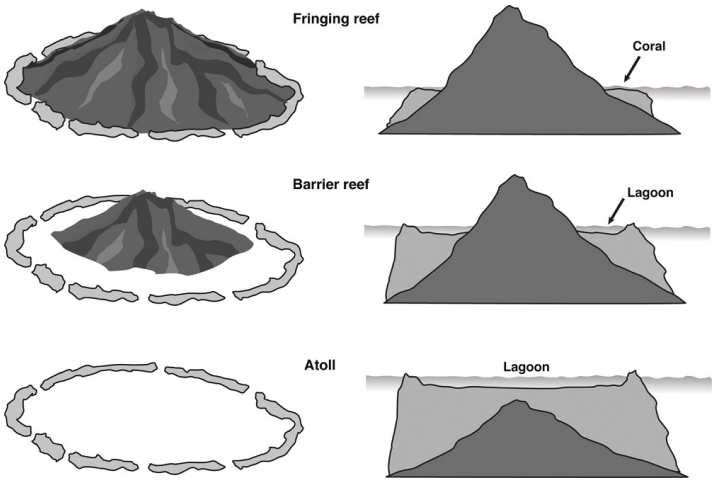

Figure 2.1: Visual representation of the three reef types

Coral reefs often form a steep transition from relatively deep to shallow water. From offshore to onshore, the morphology of a typical atoll reef is divided into three main regions (1) a steep sloping fore reef, (2) a reef flat where the bottom slope is minimal and the water depth is low, and (3) a deep lagoon (Lowe et al., 2005). Figure 2.2 shows a visual representation of these regions. Note that for fringing reefs, the lagoon is not present and water depths above the reef flat remain very shallow.

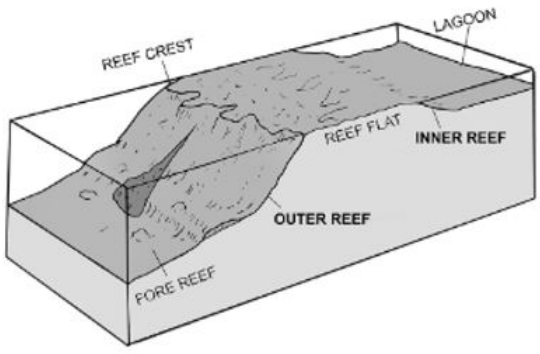

Figure 2.2: Reef zonation

2.1.1 Maldives wave climate and morphology

The 3D-printed structures will most likely be installed in the Maldives in the near future, this site and its corresponding wave climate will be used as a reference for this thesis. The Maldives, located in the central Indian Ocean, consist of about 1200 individual islands that are grouped in about 20 larger atolls (Mörner et al., 2004). The Maldives archipelago is located in a predominantly storm-free environment (East et al., 2020), where swell waves dominate. From previous performed field studies at the Maldives, average significant wave height and peak periods can be gathered at both off-shore and above the reef flat. Field studies in this specific area have been performed by Kench et al. (2006, 2009); Beetham & Kench (2014); East et al. (2020).

Kench et al. (2006) have performed field measurements on the reef flats of three different island in the South Maalhosmadulu Atoll of the Maldives, namely Dhakandhoo, Hulhudhoo and Thiladhoo, see Figure 2.3b. At these locations reef flat elevation ranged from 0.97 m below mean sea level (MSL) on the northwest edge of Thiladhoo to 1.85 m below MSL on the eastern edge of Dhakandhoo. Kench et al. obtained information on the deep water wave climate from a 10-year satellite altimetry wave climate data of I. Young (1999) and an independent shorter 3-year record by Harangozo (1992). These data sets indicated a dominant swell approach from southerly direction. Kench et al. has distinguished two seasons within the wave climate data based on the wave direction. They extracted a swell from April till November from the south-southwest with a peak significant wave height (Hs) of 1.8m and a peak period (T_p) of 10.5 s in June and from November till March from the south to southeast with a minimum H_s of 0.75 and a T_p of 9.5 s in February. To obtain the wave height at the reef flat, Kench et al. have conducted two 14-day measurements in June 2002 and February 2003. At all three locations H_s ranged between 0.13 and 0.42 m with a T_p range of 3.43 - 5.43 s in June. In February H_s varied between 0.08 and 0.17 m with a T_p range between 4.14 and 6.14 s.

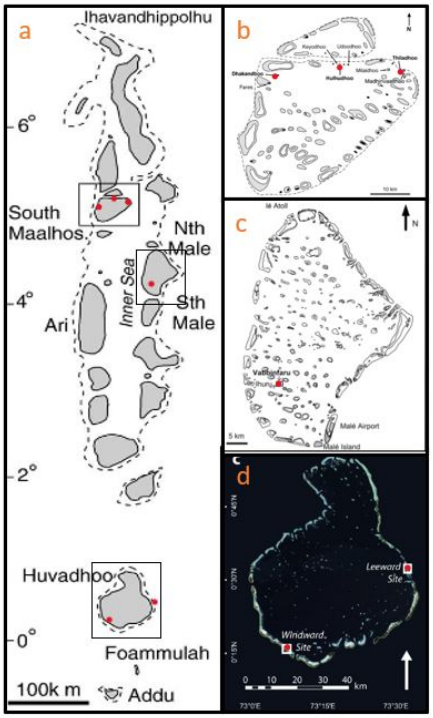

Figure 2.3: Map of Maldives (a), with detailed map of South Maalhos (b), North Male (c) and Huvadhoo (d)

East et al. (2020) have performed both offshore and nearshore field measurements at two locations at the Huvadhoo Atoll rim of the Maldives, see Figure 2.3d. At the first of the two locations, which corresponds to the windward site of the Huvadhoo Atoll, East et al. have measured H_s of 1.55 m with a T_p of 10.9 s at offshore location and above the reef flat a H_s of 0.12 m with a T_p of 9.1 s. At the leeward site, which was the second location, they have measured an offshore H_s of 1.35 m with a T_p of 9.5 s and at the reef flat they have not performed field measurements, at this location they obtained the values with the use of linear wave theory. These values correspond to a H_s of 0.6 m with a T_p of 4.3 s.

Kench et al. (2009) performed field studies at a circular reef platform in South Maalhosmadulu atoll, see Figure 2.3b. The reef flat depth varies between 0.73 m below MSL and 1.20 m below MSL. Kench et al. have used the same offshore values as for their previous field study (Kench et al., 2006). Wave

characteristics at two locations on the reef flat have been obtained during two different seasons, namely the West monsoon and the Northeast monsoon. On the reef flat H_s ranges between 0.06 and 0.23 m with a T_p varying between 6.14 and 11.71 s.

Lastly, Beetham & Kench (2014) have performed an experiment on the Vabbinfaru platform, an oval-shaped coral reef inside North Malé Atoll of the Maldives, see Figure 2.3c. The reef flat elevation at this atoll ranges between 1 and 1.5 m below MSL. Near-continuous field measurements of wave height and water level were collected over 19 days on Vabbinfaru reef platform, during the westerly monsoon in June to July 2010. Wave heights at the reef flat vary between 0.18 and 0.5 m and T_p range between 4.0 and 8.5 s. Figure 2.4 represents a summary of the wave climate data obtained.

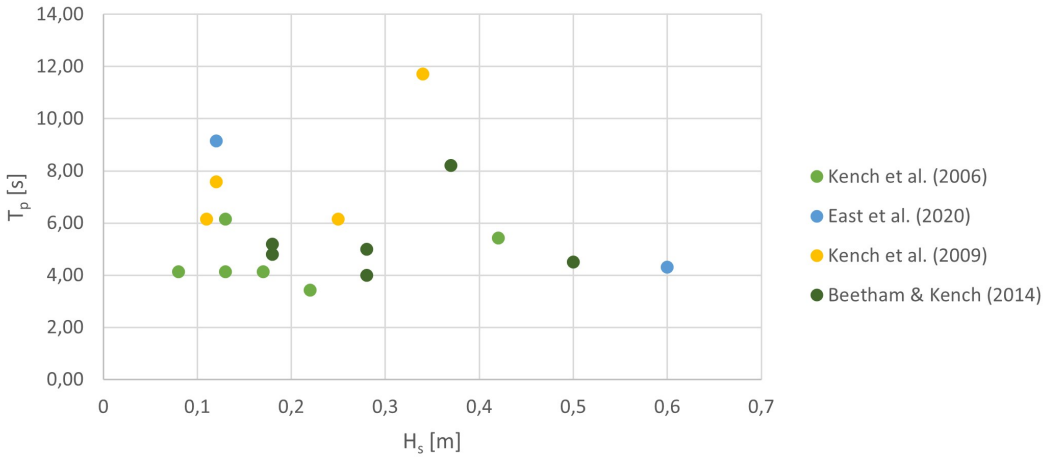

Figure 2.4: Overview of measured significant wave height H_s and peak period T_p values at reef flat of Maldives, data obtained from performed field measurements at the Maldives. Note that the comma is used as a decimal separator in this graph.

2.1.2 Structural complexity of coral reefs

Coral reefs, dominated by scleractinian corals, are intricate three-dimensional structures typically found in shallow waters (Bellwood et al., 2004). Each coral species exhibits unique variations in these three-dimensional structures. According to House et al. (2018) the 3D metrics surface area and volume play a significant role in estimating the ecosystem services and functions performed by corals. Structural complexity has been established as a critical determinant of coral reef biodiversity. Multiple studies have substantiated the existence of a positive correlation between structural complexity and various factors, including species richness, coral growth, and coastal defense (Graham & Nash, 2013; Yanovski et al., 2017; Riera, 2020; Ribas-Deulofeu et al., 2021; Ferrario et al., 2014).

Species richness

Coral reefs are one of the most bio-diverse ecosystems in the world. Over 25% of all marine fish species can be classified as reef fish, as these fish are associated with coral reefs (Allen, 2008). However, not all reef fish are reliant on live corals. Coker et al. (2014) showed that 8% of these reef fish, comprising over 320 species of fishes, use live coral for habitat. Multiple researches have proven that this large biodiversity is largely a result of the structural complexity and variety of these natural corals (Graham & Nash, 2013; Yanovski et al., 2017; Riera, 2020). Because of the wide range of cavities, branching, and density in natural coral reefs, species richness is created. In the research by Graham & Nash (2013) an assessment has been made using results of numerous studies regarding the role of structural complexity in coral reef ecosystems. According to this assessment fish density is positively correlated with structural complexity. One of the reasons is that complex corals provide effective refuge and

shelter place for small fish species to evade predators, which enhances individual survivorship and species co-existence. However, some fish species are dependent on live coral for food. Fish species that are not directly dependent on live coral, such as large predator fish, can still be attracted to areas of live coral if they contain high densities of small prey fish (Coker et al., 2014).

Coral growth

In an investigation of reef complexity dynamics in the context of climate change, Bozec et al. (2015) quantified reef topographical complexity using a roughness index referred to as reef rugosity. Their findings revealed a strong correlation between reef rugosity and total coral cover. Given that coral cover is a widely utilized metric in evaluating reef health (Leujak & Ormond, 2007), it can be deduced that coral reef ecosystems with greater structural complexity are comparatively healthier. The study by Graham & Nash (2013) also demonstrated a positive correlation between live coral cover and heightened structural complexity. In addition to increasing coral growth, high structural complexity enhances coral recovery by allowing small broken pieces of coral to remain sheltered within these complex structures rather than floating away (Graham & Nash, 2013).

In addition to the physical aspects of reef recovery, research has also explored the relationship between enhanced reef recovery and larval settlement on more complex reef structures, as exemplified by the study conducted by Hata et al. (2017). Their investigation revealed that certain topographic structures can generate turbulent flows, which are essential for capturing larvae from plankton and facilitating their delivery to the substratum as well as settlement. This mechanism is amplified by increased structural complexity, ultimately promoting reef recovery. Coral recruitment plays a crucial role in maintaining the resilience of the reef, as it supplies the primary architects of the ecosystem, which in its turn attracts other reef organisms which further increases structural complexity, creating thus a positive feedback loop (Yanovski et al., 2017). To understand natural reef resilience abilities structural complexity has been identified as a critical factor (Ribas-Deulofeu et al., 2021).

Coastal defence

Numerous studies have proven that natural coral reefs contribute to the process of wave attenuation (Costa et al., 2016; Ferrario et al., 2014; Monismith et al., 2015; Harris et al., 2018). The effect of reef roughness on monochromatic wave breaking and transmission over fringing reefs was studied by Yao et al. (2021) for example. Their study was undertaken through the conduct of laboratory experiments within a wave flume. The results of this study have demonstrated that, among various parameters associated with wave breaking, reef roughness has a significant impact on wave transmission. Specifically, their results illustrated that reefs with high levels of roughness result in lower wave transmission compared to those characterized by smoothness. The research of Harris et al. (2018) has revealed that preserving the structural complexity of coral reefs is crucial for ensuring coastal protection in tropical island regions in the future. This is owing to the high structural complexity of coral reefs, which leads to a high degree of hydraulic roughness and substantial frictional wave dissipation over relative short distances when compared to other coastal systems.

A study by Carlot et al. (2023) shows the relationship between the 2% wave run-up and the structural complexity of coral reefs. By quantifying the dissipation rates of incoming wave energy, their study shows that for a run-up height of 0.85m, which would have a return period of 100 years for a healthy reef, the return period would be reduced to 2 years if the structural complexity were halved. Lowe et al. (2005) performed a 2-week field experiment on a barrier reef in Hawaii, showing that the spectral dissipation on the reef flat was dominated by friction values, much larger than at normal sandy beaches. Relating this large frictional dissipation to the large roughness of high structural complexity of natural coral reefs. Lowe et al. (2007) showed that wave energy is dissipated more efficiently among the shorter-period motion in permeable canopies where flow can go through. Ferrario et al. (2014) performed a meta-analysis revealing that coral reefs provide substantial protection against natural hazards by reducing wave energy by an average of 97%. Their study showed that reef crests dissipate most of this energy (86%), see Figure 2.5.

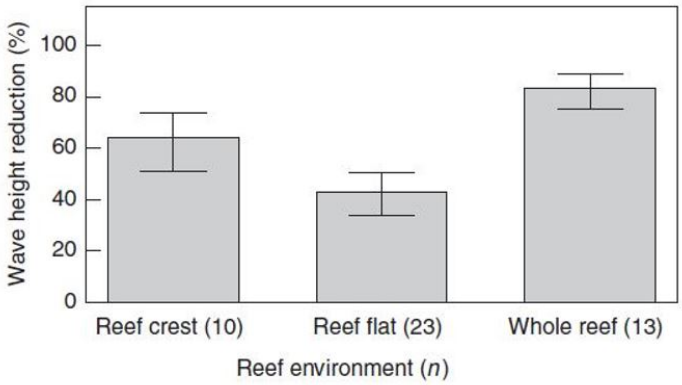

Figure 2.5: Meta-analysis results from study performed by Ferrario et al. (2014). Values are the average percentage of wave height reduction in the different reef environments. Error bars represent 95% confidence interval. 'n' reflects the number of independent experiments.

Pomeroy et al. (2023) proposed a pragmatic framework to estimate the ratio of horizontally-averaged velocities within the canopy and near the surface for various coral reef ecosystems. This study delineates three distinct reef morphologies and quantifies their geometrical configurations through the employment of diverse parameters. The findings demonstrated a linear relationship between coral cover, defined as the proportion of total coral colony planar area to the entire reef surface area, and the parameter β, which represents the rate of velocity well above the canopy relative to the velocity within the canopy itself. Furthermore, the investigation revealed that coral formations with branching morphologies exhibited the most substantial flow attenuation in comparison to their more spherically-shaped counterparts. Lastly they showed that up until a submergence of $h/h_{coral} > 6$ the flow attenuation increases with water depth.

2.1.3 Quantification of structural complexity

Structural complexity is challenging to quantify because its definition is ambiguous. Various studies have attempted to quantify geometrical complexity by employing a diverse array of parameters, yet no unified framework has been established, with each research group devising their own methodology for assessing structural complexity (Zawada et al., 2019; Riera, 2020; Yanovski et al., 2017). Zawada et al. (2019), for instance, utilized parameters such as volume, surface area, sphericity, convexity, packing, fractal dimension, and the first moments of area and volume. In contrast, Riera (2020) employed porosity, topography, rugosity, fractal dimension, and the standard deviation of the normal, while Yanovski et al. (2017) incorporated the rugosity index, coefficient of variation, and neighbor's distance as metrics for structural complexity. Upon reviewing numerous studies attempting to quantify structural complexity of (artificial) reefs it was determined that rugosity, porosity, and fractal dimension are the most frequently cited characteristics in the literature (Sherman et al., 2002; Knudby & LeDrew, 2007; Graham & Nash, 2013; Reichert et al., 2017; Yanovski et al., 2017; Harris et al., 2018; Riera, 2020; Ribas-Deulofeu et al., 2021).

Porosity is a measure of the proportion of voids to solids of a structure. Riera (2020) has developed a more precise framework to guide on the choice of design of artificial reef structures to optimize the effectiveness. In this study porosity is defined by the ratio of cavities volume to the occupied volume, or also called the volume of the bounding box, and it can be computed according to:

$$n = (V_o - V_t)/V_o \tag{2.1}$$

where:

- V_t: total volume of the structure

- V_o: volume occupied by the length, width and height of the bounding box

This value is often used when designing structural complex artificial reefs, since it is fairly simple to apply on digital models of artificial reefs. However, for existing natural coral reef, this value is difficult to compute, as one cannot obtain the value of the total volume of a structure without large errors, because the coral is fixed to the seabed and cannot be disturbed. The porosity index can be computed either for a single structure, or for the full reef as a whole.

Rugosity is another index often used to quantify structural complexity of coral. This index can be measured using the 'Chain-tape method', which is widely used on natural coral, as it is an in-situ and low cost method (Walbridge et al., 2018). To obtain the rugosity index with this method, a chain of known length is laid along the contours of the seabed. The ratio of its draped length to its undraped length gives a rugosity value (G. Young et al., 2017), see Figure 2.6. The scale of the rugosity measurement depends on the size of the links. A smaller link size will capture more detail in surface variations and thus results on a rugosity index for a smaller scale (Knudby & LeDrew, 2007).

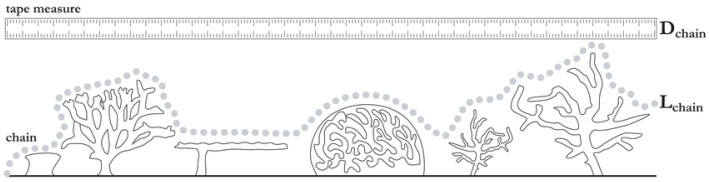

Figure 2.6: Visualisation of chain-tape method (Walbridge et al., 2018)

Fractal dimension is a measure that defines the way of branching of a structure or translates the way an object fills the space (Riera, 2020). For a given surface, the value falls between 2 and 3, with higher values indicating greater structural complexity. This approach enables the investigation of structural complexity within predefined size categories. For instance, researchers can define a size category based on the specific habitat requirements of a particular species of interest or calculate complexity for multiple categories within a reef area (G. Young et al., 2017).

2.2 Artificial reefs and submerged breakwaters

There are various types of artificial reefs that have been constructed around the world. One kind of artificial reef that is used widely are submerged breakwaters, these structures are developed from an engineering perspective, with little to no ecological added value, such as consideration for creating a habitat for marine life (Armono, 2004). The hydrodynamic effect of (submerged) breakwaters on wave attenuation has been widely studied. Submerged breakwaters are vital coastal protection structures for recreational and residential coastal regions since they have a lower negative environmental and aesthetic impact and cost to build (Kurdistani et al., 2022). These structures can be constructed using ordinary rock type, with a certain D_{50} (Van der Meer & Daemen, 1994). However, recent studies have demonstrated the potential for utilizing alternative types of blocks, such as perforated concrete blocks, geosynthetic tubes, reef balls, and wave breaker coral restoration (WABCORE) systems, to provide ecological value in marine environments (Safari, 2018).

On the other hand, other types of artificial reefs have been developed which have been based on an ecological viewpoint and are designed to act as a habitat for fish and promote marine biodiversity, these reef types however are oftentimes less effective in dissipating wave energy than the submerged breakwater structures. Examples are The MOdular SEalife System (MOSES) made by Reefsystem, and Modular Artificial Reef Structure (MARS) designed by Reef Design Lab. According to the Guidelines for the Placement of Artificial Reefs, the purpose of an artificial reef is to emulate the functions of a natural reef, which includes protecting, regenerating, concentrating, and/or enhancing

populations of living marine resources. The objectives of constructing an artificial reef can also include promoting research, restoring and regenerating aquatic habitats, and creating recreational and educational opportunities. (UNEP, 2009) And according to Baine (2001), these objectives can be achieved by constructing artificial reefs and placing them on the seabed to mimic the characteristics of natural coral reefs, both hydrodynamically and ecologically. Figure 2.7 shows a few of the artificial reefs named above.

(a) Reef Ball

(b) WABCORE

(c) MOSES

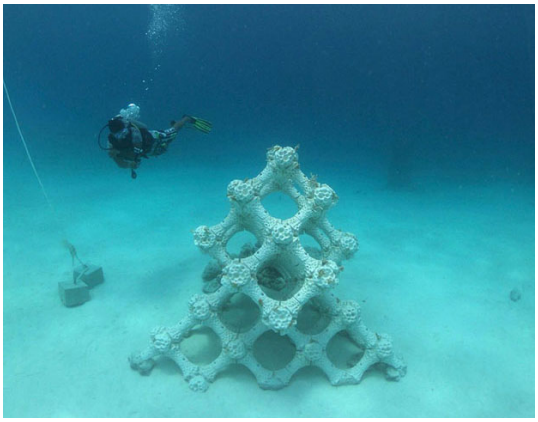

(d) MARS

Figure 2.7: Few examples of the many artificial reefs

To summarize, the design of an artificial reef depends on its intended goal. In some cases an artificial reef may be constructed in the form of a submerged breakwater, where its main function is to attenuate incoming waves and reduce coastal erosion. These types of reefs are typically designed from an engineering perspective and do not prioritize the function as fish habitat or support marine biodiversity. In contrast, other artificial reefs are designed to serve as a replacement for the broken or diminished natural coral reef, and to fill up these spaces to account for regrowth and re-stabilization of natural coral and fish species. These types of reefs are constructed with an ecological point of view and serve as a habitat for marine organisms, supporting marine biodiversity, and promoting the restoration and regeneration of marine life and habitats.

2.2.1 Wave transmission over submerged structures

The transmission coefficient is a value that often is used to describe the effectiveness of submerged hydraulic structures that aim to reduce wave height or wave energy, such as submerged breakwaters. It is a factor that relates the transmitted wave height (H_t) to the incoming wave height (H_t) in the

following form;

$$K_T = \frac{H_t}{H_i} \tag{2.2}$$

The lower the transmission coefficient, the more effective the structure is at attenuating wave energy. However, the transmission coefficient does not give information on what processes have contributed to the reduction in wave height. Much research has been done to derive empirical relationships that relate certain wave conditions to their influence on wave transmission. These empirical relationships are often derived only for structures with a specific type of block and they all have their own Validity range.

Various studies have included the effect of porosity on wave transmission such as Dick & Brebner (1968), who have studied both permeable and impermeable breakwaters and showed that a submerged permeable breakwater for depths of submergence greater than 5% of the total depth transmits less wave energy than the solid with the same dimensions. Huang et al. (2003) performed numerical tests for porous breakwaters and found out that if the breakwater width is small in comparison to the incoming wave length, the permeability of the structure has no significant effect on the wave transformation. However for wider porous breakwaters they showed that an increase in porosity results in a smaller reduction coefficient. They argue that an optimum porosity value seems to exist, at which the transmitted wave height is minimized. The results of their study found that for breakwaters with $B/h \leq 5$, (B=crest width and h=still water level) the structure permeability has no apparent effect upon the wave reflection. Ting et al. (2004) examined the impact of porosity in submerged breakwaters on the transformation of non-breaking waves. Their findings demonstrated that submerged breakwaters with higher porosity led to a reduced reflection coefficient (K_R). Additionally they found that the model width has little effect on wave reflection and transmission when the model heights are fixed. They also demonstrated that the energy loss is minimal for structures with higher porosity. Kondo & Toma (1972) revealed that the reflection coefficient does depend on the model width and reaches its maximum value for B/L (L=local wave length) ratios of approximately 0.2 to 0.25, before decreasing as the B/L ratio increases, and remains relatively constant for B/L ratios greater than 0.6. Conversely, the transmission coefficient (K_T) declines almost exponentially as the B/L ratio increases.

2.2.2 Existing empirical formula

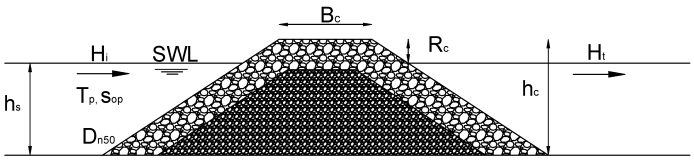

Figure 2.8: Definition sketch of the important transmission parameters over breakwaters. See Table 2.1 for an overview of the parameters. (Brancasi et al., 2022)

As previously discussed, numerous empirical formulas have been developed to estimate the transmission coefficient over a submerged breakwater. The primary objective of these formulas is to offer a general prediction method for assessing the effectiveness of (submerged) breakwaters in reducing wave heights, given a set of wave parameters. However, these prediction methods are primarily tailored to datasets focusing on breakwaters rather than coral reefs and also mainly include wave breaking. In the current study, a distinction is made between various structure types with different porosity and thus permeability levels. A selection of some existing empirical formulas predicting K_T over (submerged) structures is provided below, including their respective ranges of validity, with an emphasis on equations applicable to submerged permeable structures. Note that there are many more empirical equations, and the selection is based on providing a wide variety of parameters and their dependencies. Figure 2.8 displays a definition sketch containing the parameters of the formulae.

Symbol	Unit	Definition
H_i	[m]	Incident significant wave height at the toe of the structure
T_p	[s]	Peak wave period
h_s	[m]	Water depth at the toe of the structure
h_c	[m]	Structure height
R_c	[m]	Crest freeboard $R_c = h_c - h_s$, negative for submergence
B	[m]	Crest width
$tan\alpha$	[-]	Structure seaward slope
S	[-]	Wave steepness, $S = 2\pi H_i / g T_p^2$
ξ	[-]	Iribarren number, $\xi = tan\alpha / \sqrt{S}$
D_{n50}	[m]	Nominal armor diameter, $D_{n50} = (M_{50}/\rho_a)^{1/3}$
n	[-]	Porosity of the structure

Table 2.1: Wave characteristics and structural parameters as found in Figure 2.8

In 1990, van der Meer obtained an empirical formula for emerged and submerged breakwaters, which only depended on R_c/H_i, where an increase in R_c/H_i resulted a decrease in transmission coefficient, according to:

$$K_T = 0.46 - 0.3\frac{R_c}{H_i}, \qquad \text{for } -1.13 < \frac{R_c}{H_i} < 1.2 \tag{2.3}$$

In their formula the transmission coefficient is limited to $0.1 \leq K_T \leq 0.8$. A little later Van der Meer & Daemen (1994) obtained practical design formulas for dynamically stable reef breakwaters. Which they defined as a low-crested homogeneous pile of stones without a filter layer or core, which is allowed to reshape due to wave attack. This design formula was as follows:

$$K_T = \left(0.031\frac{H_i}{D_{n50}} - 0.24\right)\frac{R_c}{D_{n50}} - 2.6S - 0.05\frac{H_i}{D_{n50}} + 0.85 \tag{2.4}$$

The range of validity of this equation is $1 < H_i/d_{n50} < 6$ and $0.01 < S < 0.05$. Van der Meer & Daemen (1994) included the relative wave height in the form of H_i/D_{n50} and relative crest height in the form of R_c/D_{n50}. Results of their study showed that an increase in R_c/D_{n50} or steepness (S) results in a decrease in K_T. Additionally, for a submerged breakwater, where R_c/D_{n50} is negative, a larger H_i/D_{n50} produces smaller wave transmission.

Later d'Angremond et al. (1996) continued with the formula by Van der Meer & Daemen (1994) and improved this by including a dimensionless expression of the crest width and the wave height (B/H_i) as well as the Irribaren number (ξ). Their empirical formula for transmission coefficient for a permeable structure is:

$$K_T = -0.4\frac{R_c}{H_i} + 0.64\left(\frac{B}{H_i}\right)^{-0.31}(1 - e^{-0.5\xi}) \tag{2.5}$$

Considering the range of validity of Equation (5.5) as: $0.075 < K_T < 0.8$ and $B_c/H_i < 10$. With an increase of R_c/H_i or B/H_i, the transmitted wave height decreases. Seabrook & Hall (1998) performed physical model studies including a large number of wide crested structures, which was previously not included yet. Their study found that the relative submergence (R_c/H_i), incident wave height (H_i) and structure crest width (B) are the most important design variables. The newly improved empirical formula as resulted from their study is:

$$K_T = 1 - \left(e^{-0.65\frac{R_c}{H_i} - 1.09\frac{H_i}{B}} + 0.047\frac{BR_c}{LD_{n50}} + 0.067\frac{R_c H_i}{BD_{n50}}\right) \tag{2.6}$$

Again an increase in R_c/H_i or B/H_i resulted in a decrease of the transmitted wave height. This formula is applicable to wider structures and has the following limitations: $0.56 < h/d < 1$, $0 \leq$

$BR_c/LD_{n50} \leq 7.08$ and $0 \leq R_cH_i/BD_{n50} \leq 2.14$. In this formula BR_c/LD_{n50} signifies the effect of drag losses within the structure and R_cH_i/BD_{n50} the frictional dissipation on the surface of the structure.

Much later Tomasicchio & D'alessandro (2013) improved existing equations of Goda & Ahrens (2009) by basing it on a much more extensive database for low-crested rubble-mound structures. And refined the existing formulas to the following form:

$$(K_t)_{\text{over}} = \max\left\{0, \left(1 - \exp\left[a\left(\frac{R_c}{H_i} - R_{c,0}\right)\right]\right)\right\} \tag{2.7}$$

$$(K_t)_{\text{thru}} = \frac{1}{\left[1 + C\left(\frac{H_i}{L}\right)^{0.5}\right]^2} \tag{2.8}$$

$$(K_t)_{\text{all}} = \min\left\{1.0, \sqrt{(K_t)^2_{\text{over}} + K_h^2(K_t)^2_{\text{thru}}}\right\} \text{ with } K_h = \min\left\{1.0, \frac{h_c}{h_s + H_i}\right\} \tag{2.9}$$

where:

$$K_h = \left\{ 0.8; \quad \tfrac{h_c}{h_s + H_i} \right. \tag{2.10}$$

$$R_{c,0} = \begin{cases} 1.0, & \text{for } D_{\text{eff}} = 0 \\ \max\left\{0.6; \min\left\{0.8, \frac{H_i}{D_{\text{eff}}}\right\}\right\}, & \text{for } D_{\text{eff}} > 0 \end{cases} \tag{2.11}$$

$$C = 3.450\left(\frac{B_{\text{eff}}}{D_{\text{eff}}}\right)^{0.65} \tag{2.12}$$

In this context, B_{eff} and D_{eff} denote the relative crest width and the effective diameter of the materials constituting the low-crested structure, respectively. From this set of equations it can be seen that increasing the effective width B_{eff} or decreasing the effective depth D_{eff} will lead to a lower transmission coefficient. Additionally increasing H_i/L will lead to a lower transmission coefficient, simultaneously increasing R_c/H_i will lead to a lower transmission coefficient.

Later Sindhu et al. (2015) obtained a semi-empirical prediction method of wave transmission coefficient over submerged reef-type breakwaters. Their empirical relation was defined as follows:

$$K_T = (0.02\frac{-R_c}{B} + 0.025\frac{h_c}{h_s})\left(\frac{h_s}{D_{n50}} + \frac{0.45}{\sqrt{S}}\right) \tag{2.13}$$

Their study showed that for increasing relative reef submergence h_c/h_s the transmission coefficient K_T increases. They also showed that K_T decreases with increasing steepness.

Another method for predicting the wave transmission coefficient exclusively applicable to submerged structures, was developed by Kurdistani et al. (2022). Their formula incorporates the pore pressure distribution within the mound. Notably, this formula introduces the consideration of the structure's porosity for the first time.

$$K_T = 0.576\ln\left(0.428(1+\alpha)^{0.042}\left(1 + \frac{R_c}{H_i}\right)^{0.75}\left(\frac{B_{\text{eff}}}{D_{n50}}\right)^{0.125} L^{*0.39}\omega^{0.413}\phi^{-0.18}\right) + 0.923 \tag{2.14}$$

where α is the seaward slope, $L^* = L/B_{\text{eff}}$, $\omega = 1/2\pi\tanh(2\pi h_s/L)$, $\phi = (n0.5h_sx)/(B_cH_i)$, n is the porosity of the structure, and x is the horizontal coordinate inside the breakwater core. From this empirical equation it can be deducted that an increase in porosity, while all other parameters remain constant, leads to a decrease in transmission coefficient.

Below an overview of the dependencies of how the mentioned parameters influence the wave transmission coefficient K_T or $(K_t)_{\text{all}}$ based on the different empirical formulas presented can be found:

- $\frac{R_c}{H_i}$: An increase in $\frac{R_c}{H_i}$ results in a decrease in K_T, according to Equations (2.3), (2.5) to (2.7), (2.13) and (2.14). Note that a negative value for R_c means a larger submergence, similarly this means that a decrease of submergence results a decrease in K_T.
- $\frac{H_i}{D_{n50}}$: For a submerged breakwater, a larger $\frac{H_i}{D_{n50}}$ produces smaller wave transmission, according to Equation (2.4).
- $\frac{R_c}{D_{n50}}$: An increase in $\frac{R_c}{D_{n50}}$ results in a decrease in K_T, as proven by Equation (2.4). Note again that a negative value for R_c means submergence. Similarly Equation (2.13) confirms this dependency, as an increase in reef submergence h_c/h_s, results an increase in K_T.
- $\frac{B}{H_i}$: According to Equations (2.5) and (2.6) an increase in $\frac{B}{H_i}$ results in a decrease in the transmitted wave height.
- $\frac{H_i}{L}$: An increase in steepness (S) results in a decrease in K_T, according to Equations (2.4), (2.9) and (2.13).
- n: In Equation (2.14) it shows that an increase in porosity leads to a decrease in transmission coefficient.

2.3 Hydrodynamic processes at (artificial) reefs

A deep water wave crossing a reef undergoes several physical transitions as a result of the changing bathymetry (see Figure 2.2). When an onshore propagating wave length is roughly equal to the water depth, it starts to interact with the forereef. The wave initially begins to steepen due to a process known as shoaling, until eventually at a specific critical water depth (h), the wave breaks. This water depth is dependent on the wave height and thus a maximum allowable wave height can exist according to the following relationship:

$$H_s \leq \gamma h \tag{2.15}$$

where h represents the local water depth and γ is known as the breaker parameter This parameter can be estimated roughly based on local water depth and typically ranges between 0.75 and 0.83, with an average of 0.78 (Galvin, 1972; Holthuijsen, 2010; Bosboom & Stive, 2021). This means that an individual wave height in an irregular wave field in shallow water cannot exceed $0.75h$ and will thus break when reaching that value due to shoaling and arriving at shallow water depth. Breaking of waves happens in a finite zone which is called the surf zone. At natural reefs, most waves tend to break close to or at the reef crest as this is the shallowest part of the reef. After the largest waves have broken, only waves with height ratios that are smaller than the breaker limit will continue to propagate towards the coast over the reef flat. As stated by Lowe et al. (2005) it could be said that the reef crest serves as a low-pass wave height filter by filtering out waves larger than a certain height-depth ratio.

Next to wave dissipation due to wave breaking, the small waves that are free to pass the reef crest and propagate over the reef flat will also dissipate, only not due to wave breaking but due to bottom friction caused by the hydraulic rough reef. The large structural complexity of coral reefs results in high hydraulic roughness and subsequently greater frictional dissipation of waves (Harris et al., 2018). In this research, the 3D printed AR units will be designed such that they mimic the structural complexity of natural corals. As a result, the ARs of this study are intended to be positioned at the reef flat; thus, roughness dissipation will be the focus of this thesis.

This frictional energy dissipation is frequently parameterized using an energy dissipation factor f_e or the related wave friction factor f_w (Nunes & Pawlak, 2008). The frictional dissipation can be calculated according to the following equation (Jonsson, 1967),

$$\frac{dE_f}{dx} = \frac{2}{3\pi}\rho f_e U^3 \tag{2.16}$$

where E_f is the wave energy flux and U is the amplitude of the bed velocity variations (Nelson, 1996) or the maximum horizontal wave velocity above roughness (Lowe et al., 2007). To compute f_e the total energy loss at a known distance should be measured. As stated by Nelson (1996) in a constant water depth the loss rate of wave energy per unit surface area (the left hand side of Equation (2.16)) can be expressed as,

$$\frac{dE_f}{dx} = \frac{\rho g c_g}{8} \frac{dH_s^2}{dx} \tag{2.17}$$

Where c_g represents the group velocity. Combining Equation (2.16) and Equation (2.17), and rearranging the parameters the following expression results,

$$f_e = \frac{3g}{8\pi^2} \frac{(H_1 - H_2)}{H_1 H_2} \frac{c_g}{\Delta x} (T_p sinh(kh))^3 \tag{2.18}$$

From this expression an energy dissipation factor averaged over the full spectrum can be computed by comparing the wave heights in front of the reef (H_1) and at the rear end (H_2).

Madsen (1994) has developed a model to predict the rate of energy dissipation due to friction in turbulent wave boundary layer flows for spectral wave conditions. The depicted flow parameters in this model are defined by taking a weighted average of the provided parameter and giving greater weight to the frequency components that contain more wave energy. In this model, the representative maximum near-bed horizontal orbital velocity $u_{b,r}$ is defined as,

$$u_{b,r} = \sqrt{\sum_{j=1}^{N} u_{b,j}^2} \tag{2.19}$$

$u_{b,j}$ represents the velocity corresponding to the jth frequency component. Similarly a representative wave radian frequency (ω_r) can be defined as,

$$\omega_r = \frac{\sum_{j=1}^{N} \omega_j u_{b,j}^2}{\sum_{j=1}^{N} u_{b,j}^2} \tag{2.20}$$

By implementing Equations 2.19 and 2.20, the dissipation due to bottom friction for spectral wave conditions then becomes,

$$\epsilon_{f,j} = \frac{1}{4} \rho f_{e,j} u_{b,r} u_{b,j}^2 \tag{2.21}$$

Here $\epsilon_{f,j}$ represents the rate of dissipation due to bottom friction for a given wave frequency and $f_{e,j}$ corresponds to the jth component of the energy dissipation factor. In the same theory, Madsen (1994) related the energy dissipation factor ($f_{e,j}$) to the wave friction factor ($f_{w,j}$) according to,

$$f_{e,j} = \sqrt{f_{w,r}} \sqrt{f_{w,j}} cos\phi_j \tag{2.22}$$

Here $f_{w,j}$ corresponds to the jth component of the wave friction factor and $f_{w,r}$ to the representative wave friction factor. ϕ_j is the phase angle between the bottom shear stress and the near-bed horizontal orbital velocity. Finally a representative energy dissipation factor can be obtained by using the weighted average approach, according to,

$$f_{e,r} = \frac{\sum_{j=1}^{N} f_{e,j} u_{b,j}^2}{\sum_{j=1}^{N} u_{b,j}^2} \tag{2.23}$$

This gives a single energy dissipation factor that is representative of the spectral wave conditions.

Madsen (1994) and Nielsen (1992) have developed formulas to predict wave friction factors as a function of the hydraulic roughness length k_w. Madsen (1994 extended already existing monochromatic friction formulas to spectral conditions according to:

$$f_{w,j} = exp\left[a_1\left(\frac{u_{b,r}}{k_w\omega_j}\right)^{a2} + a3\right] \tag{2.24}$$

where the empirical coefficients are $a_1 = 5.5$, $a_2 = -0.2$ and $a_3 = -6.3$ according to Nielsen's (1992) research and $a_1 = 7.02$, $a_2 = -0.078$ and $a_3 = -8.82$ according to Madsen's (1994). With these predictive wave friction formulas a predicted dissipation factor can be computed with:

$$f_{e,r} = f_{w,r}cos\phi_j \tag{2.25}$$

where,

$$\phi_j = 33 - 6.0log_{10}\left(\frac{u_{b,r}}{k_w\omega_r}\right) \tag{2.26}$$

Chapter 3 | Physical model

3.1 Experimental set-up

To test the influence of structural complexity on the amount of wave attenuation, physical tests have been performed in a wave flume at Deltares. In this physical model, three different designs were distinguished and tested under the same wave conditions. More detail regarding the design will be provided in Section 3.3.1. Figure 3.1 shows a definition sketch illustrating how different parameters are defined in the physical model. More details on the set-up of the flume and its measuring devices will be given in sections 3.1.2 and 3.1.3.

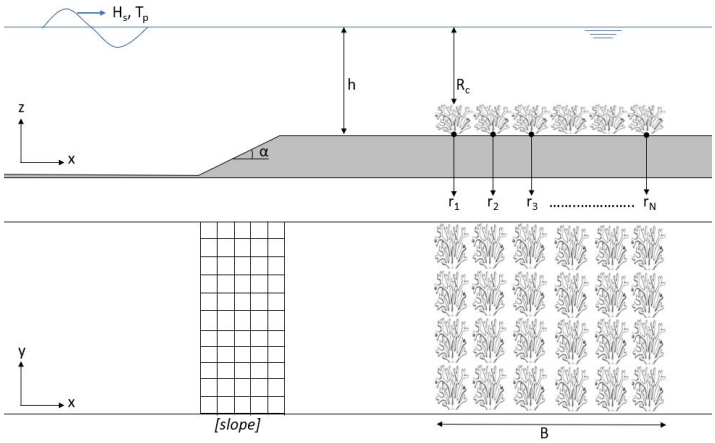

Figure 3.1: Definition sketch, including axis orientation. Note that the sketch is not to scale.

3.1.1 Properties of the Scheldt flume

The Eastern Scheldt flume at Deltares is 55 m long, 0.996 m wide, and 1.25 m tall. The waves are generated at one side of the flume by a piston-type wave generator, which is capable of generating both regular and irregular waves. An Active Reflection Compensation (ARC) is present in the wave board; it identifies any reflected waves and compensates the wave board motion to absorb these reflected waves (Deltares, 2015). At the end of the flume, a wave absorber is located, which minimises the amount of wave reflection. The maximum water depth that can be achieved in the Scheldt Flume is 0.8 m.

3.1.2 Foreshore

A unique foreshore has been constructed in the wave flume. Including a foreshore in the flume allows for waves to break and shoal on the slope, as happens in reality. The height of the foreshore affects the variety of possible wave conditions to be performed during the tests when taking the Ursell number into account. The Ursell number quantifies the degree of non-linearity of waves and is defined as (Holthuijsen, 2010),

$$N_{Ursell} = \frac{HL^2}{d^3} \tag{3.1}$$

If this number is less than 26, linear wave theory and 2nd order Stokes theory can be applied. The wave paddle can generate waves up to 2nd order Stokes, therefore this limit should be applied. In order to find the optimum dimensions, a rapid assessment of this maximum Ursell number was carried out to determine the possible wave conditions for different dimensions of the foreshore. The results

of the rapid Ursell number assessment can be found in Appendix A. The foreshore has a total length of 20.72m and height of 0.4m, with two 1:1 slopes. The final dimensions of the foreshore can also be found in Figure 3.2, which provides a detailed sketch of the flume test set-up.

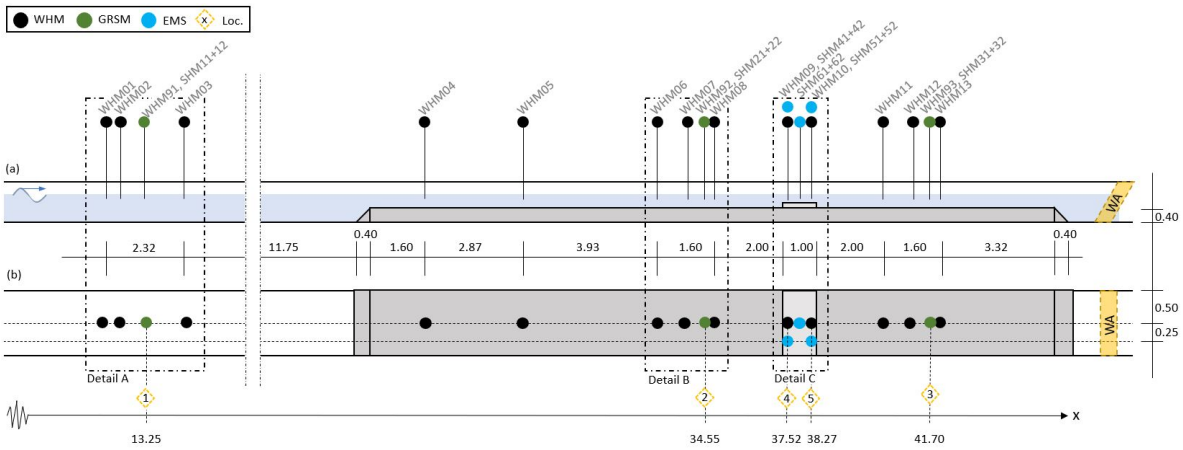

Figure 3.2: Experimental set-up of the physical model in the wave flume, including foreshore dimensions and instrumentation positions in x and y dimensions. (a) side view, (b) top view. Units are in metres. WA stands for wave absorber. Note that the x axis does not start at the origin. Z locations of all the velocity measurements at location 1, 2 and 3 is z=0.05m above the (foreshore) bed, while at location 4 and 5 the Electromagnetic Velocity Meter (EMS) devices are placed at z=0.20m above the foreshore bed. The EMS device located between location 4 and 5 is placed at z=0.07m above the foreshore bed. The figure includes the device names, WHM corresponds to a wave gauge and SHM to a velocity device.

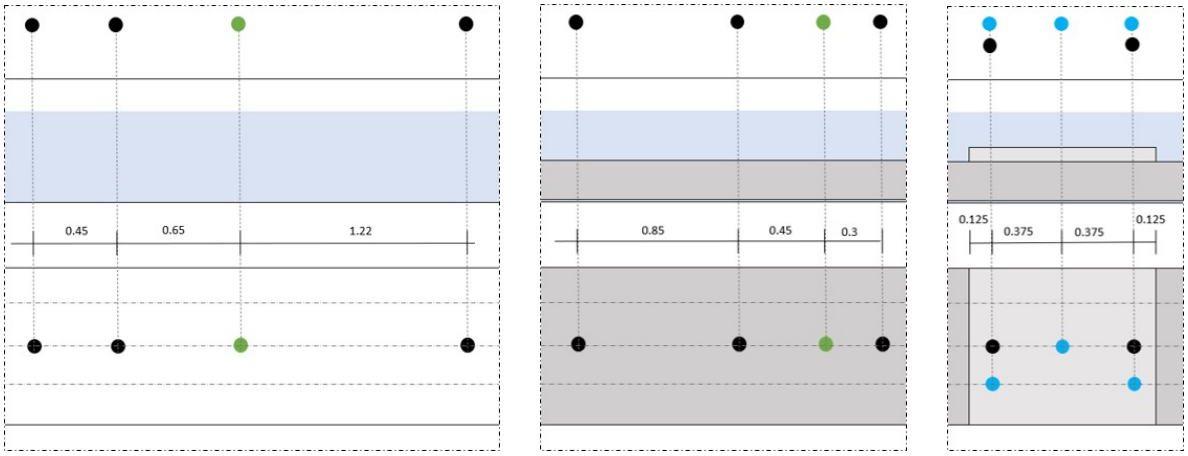

(a) Detail A *(b) Detail B* *(c) Detail C*

Figure 3.3: Detail sketches of Figure 3.2. Units are in metres

3.1.3 Measuring devices

In order to determine wave dissipation, data is collected by measuring and comparing surface elevation time series in front of and behind a reef. There are multiple methods of measuring the surface elevation such that incident and reflected time series can be extracted. In this thesis two of these methods will be applied. The first method involves the use of multiple wave gauges, for this method four wave gauges need to be placed in close proximity to one another (Lin & Huang, 2004). For the second method it is necessary to measure orbital flow velocity and surface elevation at the same x location. This can be

achieved by placing a wave gauge and velocity meter at the same x location in a flume (Buckley et al., 2015). More information on these two methods will be given in Section 4.2. In addition to measuring surface elevation, the orbital velocity within the reef was also measured. This was done by placing a velocity measurement device at the midpoint of the reef's height and width. In total the set-up includes 13 Wave gauges (WHM), 3 Wave Height and Direction Meters (GRSM), 3 Electromagnetic Velocity Meters (EMS) and 1 camera. All EMS devices have been placed at 5 cm above the (foreshore) bed, except for the two EMS devices above the reef (location 4 and 5), these have been placed at 20cm above the foreshore bed and the single EMS device in the middle of the reef, this device is placed at 7cm above the foreshore bed.

Wave Height Meter (WHM)

A wave height meter or wave gauge is a device that measures the surface elevation of waves in water. It uses an electric conduction meter to measure the electrical conductivity of the water between two parallel stainless steel rods, which act as electrodes. As the water level changes, the distance between the rods changes, and with it, the electrical conductivity. The device's electronics convert this electrical conductivity into a voltage signal, which is proportional to the water level (distance between the rods). To establish a correlation between the voltage signal and the surface elevation, a calibration process is needed. A reference electrode is also used to compensate for variations in the water conductivity, ensuring accurate measurements. The mathematical relationship between the voltage signal and the surface elevation is established during the calibration process, which is typically done by measuring the voltage signal while the water level is known at different water levels. The accuracy of the WHM is equal to 0.5 % of the measuring range.

The wave gauge meter can be used as a standalone probe or in conjunction with a control unit. The control unit allows for adjustments to the output signal's gain and zero shift, as well as providing power to the probe. The probe consists of two parallel stainless steel rods mounted on a small box containing electronics for sensor excitation, signal detection, amplification, and galvanic isolation. The device has fast dynamic response and a wide range of 0.5 meters (with other ranges available) (Deltares, 2012a).

Electromagnetic Velocity Meter (EMS)

The electromagnetic velocity meter is a device that measures the bi-directional flow velocity of conductive liquids in two perpendicular directions. The measurement principle is based on the movement of conductive liquid through a magnetic field, which is induced by electrical current flowing through a small coil located inside the body of the probe. The probe features two pairs of diametrically opposed platinum electrodes that sense the induced voltages produced by the flow past the probe. The design of the probe ensures that these voltages are proportional to the liquid velocity parallel to the plane of the electrodes.

The probes measure liquid velocity using a magnetic field beneath the probe and should not be disturbed. The probes must be connected to a control unit to function. The control unit for the electromagnetic liquid velocity meter can be used with different types of probes, and its various functions can be controlled by three keys on the front panel. The accuracy of the measurements is +/- 0.01 m/s +/- 1 % of the measured value. The control unit, however, does not include data handling software. The electromagnetic velocity meter is a useful tool in many industries to measure the flow of conductive liquids (Deltares, 2012b).

Wave Height and Direction Meter (GRSM)

The wave height and direction meter measures both surface elevation and orbital velocity simultaneously by combining two probes at the same spot. One probe measures the surface elevation, while the other probe measures orbital velocity. The main purpose of this instrument is to measure wave direction and directional spreading. Each probe is connected to a dedicated control unit by a power signal cable. Both control units are mounted in the same universal carrying case (UCC). The output signals for surface

elevation and x- and y-velocities are in analog form. The electromagnetic velocity probe is mounted underneath the wave height probe, and the two instruments share the same measurement principle. Both the wave height and direction meter and the electromagnetic velocity meter are designed to measure the bi-directional flow velocity of conductive liquids in two perpendicular directions and use a magnetic field beneath the probe to measure the liquid velocity (Deltares, 2012c).

3.2 Scaling

When creating a physical model, scaling is necessary to ensure that the model accurately represents the behaviour of the real system it is intended to represent. There are several types of scaling. Froude scaling and Reynolds scaling are two different scaling methods often used in fluid dynamics experiments. The choice between these scaling methods depends on the specific problem being studied and the experimental resources available. While studying the behaviour of waves in wave flume experiments, Froude scaling is a type of dynamic scaling that is frequently used. The wave height, wave period, and water depth are all scaled according to the actual system being represented. Froude scaling is a useful option for wave flume experiments because it enables the precise representation of wave dynamics in a smaller-scale physical model, which can aid in lowering the cost and complexity of the experiment. Reynolds scaling, on the other hand, is frequently employed for researching smaller-scale fluid dynamics problems, such as the behaviour of fluids around small objects or in microfluidic systems. This is because Reynolds scaling incorporates the effects of viscosity, which is more important at smaller scales. (Briggs, 2013)

In this research the choice has been made to apply Froude scaling, since the viscosity and surface tension do not play a significant role when looking at wave tests. The range of the Reynolds values in the model corresponding to the wave conditions performed in the current study is Re = 10,000 - 40,000. In the physical model inertia and gravitational forces are the governing forces. In this scaling law, the Froude number should be equal in prototype and model according to the following relationship

$$\frac{u_m}{\sqrt{g_m L_m}} = \frac{u_p}{\sqrt{g_p L_p}} \tag{3.2}$$

Where u is the velocity, g the gravitational force and L a length. Models are typically undistored, meaning that all length scales should be scaled according to a constant scale factor $n_L = L_p/L_m$. Assuming a gravitational scale of g of 1, the scale of the velocity becomes $n_v = u_p/u_m = \sqrt{n_L}$. In Table 3.1 some typical scale quantities according to the Froude scaling are given.

Variable	Unit	Similitude	Froude scaling
Length	L	G	n_L
Time	T	K	$n_L^{0.5}$
Velocity	LT^{-1}	K	$n_L^{0.5}$
Energy	ML^2T^{-2}	D	$n_L^4 n_\rho$

Table 3.1: Froude scale factors for commonly used variables. M=Mass, L=Length, T=Time. G=Geometric, K=Kinematic and D=Dynamic.

In this research, the artificial reef structures where printed using the 3D printer of Coastruction. As mentioned previously, this printer can print structures of dimensions 25x25x15 cm. In the near future, the second scaled up printer of Coastruction will be constructed, which can print elements of 100x100x100 cm. Based on this information, a Froude scale factor of $n_L = 4$ has been applied to the physical model.

3.3 Reef structures

This chapter provides further details on the designs of two distinct complex structures. The degree of structural complexity has been measured using two parameters: porosity and rugosity. Additionally, the various reef configurations utilized in the experiments will be expounded upon. The two structural complex designs were printed with the 3D-printer from Coastruction. Appendix B provides an elaborated explanation of the printing process.

3.3.1 Element designs

The objective of this study is to investigate the relationship between structural complexity and the extent of wave attenuation. The structures were designed to enhance biodiversity through two main categories: coral growth and fish species richness. To promote coral growth, the structures were designed with horizontal ledges that provide exposure to light, as corals require light for growth (Osinga et al., 2011). To increase fish species richness, the structures were designed with a variety of hollow shelters and tunnels of varying sizes, providing a diverse range of habitats for different species to inhabit the reef.

In this research, structural complexity is defined with the use of two parameters: rugosity and porosity. In literature, rugosity in natural coral reefs is often measured using the so called chain link method, which measures the difference between the distance covered by a fine-link chain closely laid over a section of coral reef and its known linear distance (Ribas-Deulofeu et al., 2021; Bleck, 2006; Yanovski et al., 2017). This method has accordingly been used in this research to identify the rugosity of the reefs. The second parameter which has been utilised to identify the structural complexity in this study is porosity. This value can be computed by dividing the volume of the structure by its smallest surrounding solid cube. This means, that by increasing rugosity, the porosity will be increased as well, since certain volume of the cube needs to be extracted to increase rugosity. As the printer can print 25x25x15 cm, the designs of the two different prints have been originated from this rectangular cube. The rectangular cube (Figure 3.4a) can be treated as a reference design, where both porosity and rugosity are equal to zero.

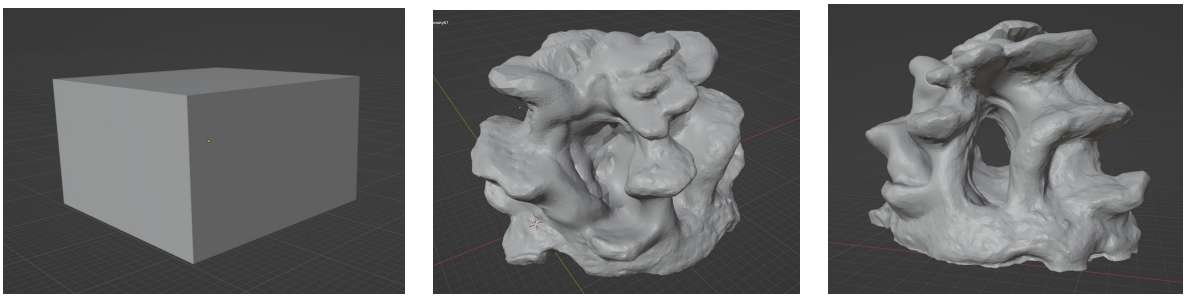

(a) Rectangular cube *(b) Design 1* *(c) Design 2*

Figure 3.4: Visualisations of the two geometrical complex designs (b) and (c) that have been tested in the wave flume. (a) shows the rectangular cube that has been used as a structure with zero structural complexity.

By increasing the rugosity of the rectangular cube, the first design was created (Figure 3.4b). Ridges and ledges have been used to accomplish this. There are no voids and tunnels which means the structure is solid. The second design was then based on the first, implying that the rugosity remained constant. The second design, on the other hand, includes voids and tunnels, see Figure 3.4c. When comparing design 2 to design 1, this implies that the porosity has increased.

Table 3.2 shows an overview of the values of the two parameters, including the volume and the weights of the two designs.

Design	Porosity* [%]	Rugosity** [-]	Volume [cm^3]	Weight [kg]
1	67	2.02	3557.94	6.05
2	73	2.18	3036.77	4.8

*Table 3.2: Porosity and rugosity values of the two structural complex designs. Additionally the volume and weight of the two structures is given. *The porosity is computed for one single element. **In this case, the rugosity has been computed for a fully packed 4x4 reef, meaning with a 100% coverage.*

3.3.2 Reef configurations

In this study, several distinct reef configurations were tested to evaluate the effect of the density of structures within a reef on wave attenuation. The goal was to understand how the arrangement of these structures within the reef can influence wave dissipation. To determine the specific influence of each individual structure on wave attenuation, the reefs used in the tests were comprised exclusively of one type of structure. The reef configurations used in these experiments correspond to the reefs where 4 rows have been used, this lay-out is labeled as RL4-D1, RL4-D2, RL4-C1. Where RL stands for Reef Length, followed by a number representing the amount of structures in length, i.e. 4 indicates a reef with a length of 4 consecutive rows. The label is followed by the type of structure the reef consists of, design 1 (D1), Design 2 (D2), Cubes (C1) or both structure 1 and 2 (D12). Figure 3.5 shows an overview of all the various reef set-up that have been used in the tests.

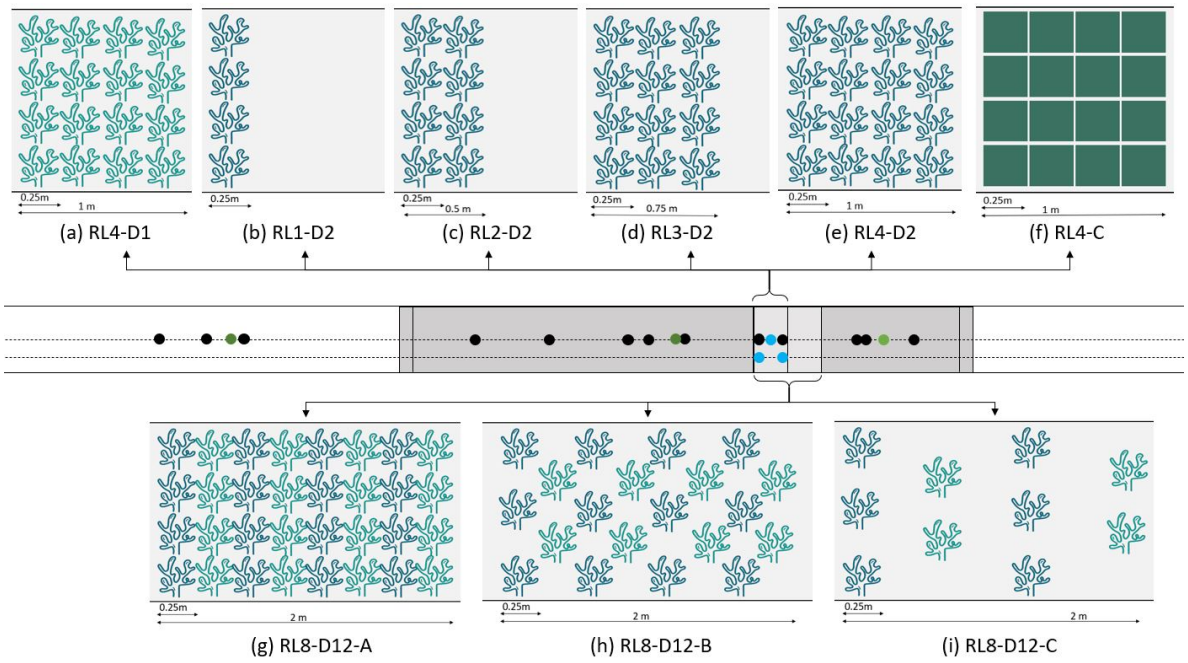

Figure 3.5: Visualisations of the reef lay-out of 4 rows comprised exclusively of (a) design 1 (RL4-D1), (e) design 2 (RL4-D2) and (f) cubes (RL4-C1). Additionally shows the reef lay-out of design 2 with (b) 1 row (RL1-D2), (c) 2 rows (RL2-D2) and (d) 3 rows (RL3-D2). (g-i) visualises reef lay-out used in test cases where the effect of reef coverage was tested

In specific test cases, the reef was composed of both designs in combination, see Figure 3.5(g-i). These experiments aimed to investigate the effect of the length of the reef, when greater than 4 rows, and the density or coverage of the reef on wave attenuation. In case of a full reef comprising of 8 rows (RL8-X), the two structures alternate row by row, see Figure 3.5 (g). These reef lay-outs are labelled as RL8-D12-A, RL8-D12-B and RL8-D12-C. Figure 3.6 shows pictures of these three reef set-ups in the flume at Deltares.

It should be noted that the measuring devices remained on the exact locations, according to Figure 3.2 during all experiments. This was due to the fact that the devices were mounted on a cart with a fixed distance above the reef. This made it impossible to replace the measuring devices above the reef according to the reef length.

(a) RL8-D12-A *(b) RL8-D12-B* *(c) RL8-D12-C*

Figure 3.6: Pictures of the reef lay-out in the Scheldt flume at Deltares.

3.4 Wave conditions

The wave conditions depend on the limits of the wave flume. The maximum achievable significant wave height (H_s) that the wave paddle can generate in the Scheldt flume is equal to one-third of the water depth at the wave paddle (h+0.4m), where h corresponds to the still water depth above the foreshore. Therefore, the following relationship holds:

$$H_s \leq \frac{h + 0.4}{3} \tag{3.3}$$

In other words, this means that when a maximum water depth of 0.8m at the wave board or h=0.4m at the foreshore is used for a testing scenario, the maximum possible significant wave height that the paddle can generate is $H_s = 0.25m$. Subsequently, as stated before. the wave paddle can only generate waves up to second order stokes. Which relates to an Ursell number of $N_{Ursell} \leq 26$, where N_{Ursell} can be computed according to Equation (3.1).

Next to the physical limits of the flume, the wave loadings to be used in the experiments are based on water levels and wave conditions commonly observed on reef flats in nature. In the Maldives, the wave climate is dominated mainly by swell waves. A typical swell spectrum is narrowly banded in the lower frequencies. In the JONSWAP this can be achieved with a large T_p and $\gamma = 5$, where γ is the peak enhancement factor (Bosboom & Stive, 2021). These values show that the steepness of a typical swell wave is less than 1%. In the wave flume however, it is not possible to recreate a spectrum transformation as happens in reality. This is due to the fact that the natural reef bathymetry cannot be entirely reproduced in this experiment. It is impossible to recreate the very steep forereef with a length scale of 4. As a result, the spectrum was simply used to see what effect the structures have on the change in spectrum shape. Therefore the choice had been made to perform the tests with a JONSWAP spectrum, which corresponds to a spectral shape parameter (γ) of 3.3.

For the experiments concerning the frictional dissipation, it should be noted that there is no wave breaking present, which means that the dissipation is only an effect of the friction. Therefore the following wave conditions have been obtained, see Table 3.3.

Note that the values for H_s and T_p have been used to create the run file for the wave paddle of the wave flume. It is possible that the wave paddle generates these exact values, however that demands extra calibration and optimisation which can take up extra time. As the available test time was limited to two weeks, the decision had been made to accept small discrepancies. For the significant wave height (H_s) and the peak period (T_p) a distinction has been made between the values as used to generate waves at the wave paddle (black) and values that were measured at location two (green) in front of the reef. All tests have also been performed with an empty flume, to serve as a reference test. In Appendix C a complete overview of each test case can be found.

The testID is labeled in a systematic way, where h denotes the water depth at the wave paddle in cm, thus always 40cm larger than h at the foreshore, H denotes the significant wave height in cm and T denotes the peak period in s, all without punctuation, as this would disturb the filenames.

- h: 70;75;80
- H: 5;75;10;22
- T: 25;4;5

h70H5T5 thus corresponds to a wave condition with water depth h=0.70m, $H_s = 0.05m$ and $T_p = 5s$. In Table 3.3 the H_s and T_p denoted in black are the target values at the wave paddle, as used in the steering file. And the green values depict the measured values in front of the reef (location 2).

TestID	R_c [m]	H_s [m]	T_p [s]	Breaking	Structure	Reef lay-out
h70H5T5	0.15	0.05 0.05	5.0 4.9	NB	C0, C1, D1, D2, D1+D2	RL4-D1, RL4-D2, RL4-C1, RL8-D12-A, RL8-D12-B, RL8-D12-C, empty
h70H22T25	0.15	0.20 0.13	2.5 2.5	B	C0, D2	RL1-D2, RL4-D2, empty
h75H5T5	0.2	0.05 0.05	5.0 5.2	NB	C0, C1, D1, D2	RL4-D1, RL4-D2, RL4-C1 empty
h80H5T25	0.25	0.05 0.05	2.5 2.5	NB	C0, C1, D1, D2	RL4-D1, RL4-D2, RL4-C1 empty
h80H5T4	0.25	0.05 0.05	4.0 4.1	NB	C0, C1, D1, D2	RL4-D1, RL4-D2, RL4-C1 empty
h80H5T5	0.25	0.05 0.05	5.0 5.2	NB	C0, C1, D1, D2	RL4-D1, RL4-D2, RL4-C1 empty
h80H75T25	0.25	0.075 0.068	2.5 2.5	NB	C0, C1, D1, D2	RL4-D1, RL4-D2, RL4-C1 empty
h80H10T25	0.25	0.10 0.09	2.5 2.5	NB	C0, C1, D1, D2, D1+D2	RL4-D1, RL1-D2, RL2-D2, RL3-D2, RL4-D2, RL4-C1, RL8-D12-A, RL8-D12-B, RL8-D12-C, empty
h80H22T25	0.25	0.22 0.16	2.5 2.5	B	C0, D2	RL1-D2, RL4-D2, empty

Table 3.3: Overview of the wave conditions that have been performed in this study. The green values represent the values at location 2, in front of the reef. Including crest submergence (R_c), significant wave height (H_s), peak period (T_p), Structure (C0: empty flume, C1: cubes, D1: design 1, D2: design 2, D1+D2: a reef comprised of both D1 and D2) and reef lay-out. Each test duration was approximately 35 min. For a more detailed overview per test case, see Appendix C

Chapter 4 | Data Processing and Extraction Techniques

4.1 Pre-processing and spectral characteristics

The raw data extracted from the measuring devices need to undergo several filtering and pre-processing steps before accurate analysis can be performed. These steps include:

1. The offset of each wave gauge was determined by measuring the average surface elevation of the first 15-25 sec. In these first seconds the measurement device started recording while the wave paddle had not been activated yet. The measured offset was then subtracted from the full data set, so that the surface elevation time series starts at zero.

2. Spin-up and spin-down times were cut out of the time series by removing the first 90 seconds and the last 60 seconds of the time series data.

3. The output of the velocity time series were checked to determine which of the two outputs of the EMS device measured the orbital velocity in the x-direction. This depends on the orientation of the EMS device and was hard to see from the flume set-up.

4. The phase relationship between the orbital velocity and surface elevation time series was checked, and where necessary, flipped 180 deg to ensure that both were in phase.

After these first pre-processing steps have been performed for all the time-series according to above, the variance density spectrum could be computed. The computation of a variance density spectrum from the surface elevation time-series involves several processing steps to ensure accurate spectral estimates. First the incident surface elevation time-series was decomposed with use of the co-located decomposition method, where a cut-off frequency of $f = 0.05$Hz was applied. (See Section 4.2.1 for more information). Subsequently the time-series was divided into 25 overlapping blocks of equal length, with a 50% overlap between consecutive blocks using, resulting a frequency scale of $\Delta f \approx 0.01$, before applying a Fast Fourier Transformation (FFT).

The significant wave height is computed using the variance density spectrum. This is done by first computing the zeroth-order moment (m_0) from the variance density spectrum according to

$$m_n = \int_0^\infty f^n E(f) df, \qquad n = ... - 1, 0, 1, ... \tag{4.1}$$

where m_n is the n^{th} moment of the variance density spectrum and $E(f)$ is the variance density spectrum. The significant wave height, denoted as H_s, is then calculated based on the zeroth order moment m_0.

$$H_s = 4\sqrt{m_0} \tag{4.2}$$

From the wave spectrum various characteristic wave periods can be extracted, such as the peak period T_P, mean wave period $T_{m0,1}$ and the mean energy period $T_{m-1,0}$. The peak period is the period that corresponds to the peak of the wave spectrum. The mean wave and energy periods are computed with use of the spectral moments according to:

$$T_{m0,1} = \frac{m_0}{m_1}, \quad T_{m-1,0} = \frac{m_{-1}}{m_0} \tag{4.3}$$

4.2 Decomposition methods

The wave paddle generates waves according to a specified steering file. Initially, these waves propagate along the flume in a single direction. However, due to the slope of the foreshore and the presence of structures on the foreshore, the waves are reflected back towards the wave paddle. Although the wave paddle is equipped with an Active Reflection Compensation (ARC) system, a certain degree of re-reflection will inevitably occur. As stated by Andersen et al. (2016), this is typically within the range of 0-10%. Additionally, some reflection is also present at the passive wave absorber, situated at the end of the flume. The reflected wave heights induced by the passive wave absorber are generally between 5-15% of the incident wave height (Andersen & Eldrup, 2021). During the tests conducted in the current study, the reflection coefficient behind the reef, specifically located at the wave absorber, ranged from 25 - 35%, which is notably higher. Further information on this phenomenon can be found in Section 6.3.3.

The measurement instruments thus record a signal that is a combination of incoming and reflected waves, in other words waves travelling in two opposite directions. The raw time series extracted from the wave gauges is therefore called the 'total' surface elevation time series. In this thesis two methods to extract incoming and reflected waves from the total surface elevation time series are distinguished and applied. The first method uses co-located velocity and surface elevation measurements at the same x location while the second method makes use of four individual wave gauges placed in a group. Both methods assume linear wave theory and thus some errors arise when the wave series are transformed to incoming and reflected waves. The subsequent sections will delineate the two methods individually, followed by a comparative analysis of the obtained results.

4.2.1 Co-located decomposition

According to linear wave theory the dispersion relation is an implicit wave number expression which requires an iterative procedure to calculate the wave number for a given frequency and depth (Holthuijsen, 2010).

$$\omega_i^2 = gk_i tanh(k_i d) \tag{4.4}$$

Here ω_i is the angular frequency for the band with, g is the acceleration due to gravity, k_i is the wave number for the specific band width, and d is the water depth. This means that each component in a wave time series travels at its own speed. With the horizontal particle velocity computed according to:

$$u = \frac{\partial}{\partial x}\left(a\frac{g}{\omega}\frac{cosh(kh_u)}{cosh(k(h+\overline{\eta}))}cos(kx-\omega t)\right) \tag{4.5}$$

Here h_u is defined as the height above the bed where the velocity is measured, k is the wave number, h is the still water level, a is the amplitude and $\overline{\eta}$ is the set-up or set-down. The linear wave theory velocity response function, K_u, is computed as follows:

$$K_u = \frac{cosh(kh_u)}{cosh(k(h_0+\overline{\eta}))} \tag{4.6}$$

After taking the derivative with respect to x and rewriting of Equation (4.5) with use of Equation (4.6) and the solution for harmonic wave propagation as $\eta(x,t) = asin(\omega t - kx)$, Equation (4.5) becomes

$$u = \frac{gk}{2\pi f}K_u\eta \tag{4.7}$$

where η denotes the surface elevation and f the frequency. This solution is applicable to one single wave component belonging to frequency f. To extract incoming or shoreward-propagating ($^+$) and reflected or seaward-propagating ($^-$) waves from the measured time series a frequency domain algorithm needs to be used. Guza et al. (1984) and Buckley et al. (2015) solved this by relating incoming and reflected

complex Fourier components of water elevation time series (F_η^+, F_η^-) to the observed total complex Fourier component (F_η) as well as the velocity components (F_u) as

$$\begin{aligned} F_\eta &= F_\eta^+ + F_\eta^- \\ F_u &= F_u^+ + F_u^- \end{aligned} \tag{4.8}$$

Likewise Equation (4.7) can be written with its incoming and reflecting Fourier components according to:

$$\begin{aligned} F_u^+ &= \tfrac{gk}{2\pi f} K_u F_\eta^+ \\ F_u^- &= \tfrac{gk}{2\pi f} K_u F_\eta^- \end{aligned} \tag{4.9}$$

Now a system of four equations (Equation (4.8) and 4.9) and four unknowns (F_η^+, F_η^-, F_u^+, F_u^-) can be solved according to:

$$\begin{aligned} F_\eta^+ &= \tfrac{1}{2}\left(F_\eta + \tfrac{2\pi f}{gkK_u} F_u\right) \\ F_\eta^- &= \tfrac{1}{2}\left(F_\eta - \tfrac{2\pi f}{gkK_u} F_u\right) \end{aligned} \tag{4.10}$$

To obtain incoming and reflected time series, the inverse Fourier transformation needs to be applied. The decomposition of incident waves using this method can be carried out at five discrete sites within the wave flume, designated as locations 1 through 5, respectively.

4.2.2 Least square method

When the surface elevation $\eta_p(t)$ is measured of a wave field at a series of locations $\{x_p\}$, p=1, 2, 3, ..., P, the elevation can be expressed as a summation of discrete, harmonically related Fourier components, according to

$$\eta_p(t) = \sum_{j=-N/2}^{N/2} A_{j,p} e^{i\omega_j t} \tag{4.11}$$

With, $\omega_j = 2\pi j/T$. $A_{j,p}$ is the Fourier coefficient for amplitude for the jth frequency, T is the length of the total time series an t is discrete for a sampled signal ($t \rightarrow m\Delta t$, for m=0, 1, ..., N-1, with $\Delta t = T/N$). When assumed that the waves are one-dimensional, there is no dissipation present and linear wave theory is valid, the water elevation at a wave gauge p can be approximated by a Fourier sum of left and right traveling waves (a_{Lj}, a_{Rj}) by

$$\eta(x_p, t) = \sum_{j=-N/2}^{N/2} \left\{ a_{Lj} e^{i\phi_{j,p}} + a_{Rj} e^{-i\phi_{j,p}} \right\} e^{i\omega_j t} \tag{4.12}$$

Here $\phi_{j,p} \equiv k_j x_p$. Equating the coefficients in Equation (4.11) and (4.12) results

$$A_{j,p} = a_{Lj} e^{i\phi_{j,p}} + a_{Rj} e^{-i\phi_{j,p}}, p = 1, 2, ..., P \tag{4.13}$$

If p=2, the above equation can be solved exactly, however for p>2, the equation is over-determined, meaning that there are more unknowns than equations and thus the values must be estimated by an approximate technique. This has been done using a least square method using uniform weighing for p=3 (Mansard & Funke, 1980), but also for p>3 by Zelt & Skjelbreia (1992). Zelt & Skjelbreia (1992) applied this by using a weighted least squares method. They minimize the value of an appropriate 'merit' function, in order for Equation (4.13) to hold approximately for each wave gauge p. This is done by setting Equation (4.13) to

$$\epsilon_{j,p} = a_{Lj} e^{i\phi_{j,p}} + a_{Rj} e^{-i\phi_{j,p}} - A_{j,p} \tag{4.14}$$

Here $\epsilon_{j,p}$ represents the error in matching the jth Fourier coefficient $A_{j,p}$ at wave gauge p. Additionally a merit function needs to be introduced which is as follows

$$E_j \equiv \sum_{p=1}^{P} W_{j,p} \epsilon_{j,p} \epsilon_{j,p}^* \tag{4.15}$$

In this equation, the weighting coefficient for wave gauge p at frequency j is denoted by $W_{j,p} > 0$, where $()^*$ denotes the complex conjugate of the enclosed quantity. The reliability of the estimates of a_{Lj} and a_{Rj} at a given jth frequency depends on several factors, including the spacing between the wave gauges. From this point the following relation holds

$$\sum_{p=1}^{P} W_{j,p}\epsilon_{j,p}e^{-i\phi_{j,p}} = 0 \tag{4.16}$$

$$\sum_{p=1}^{P} W_{j,p}\epsilon_{j,p}e^{i\phi_{j,p}} = 0 \tag{4.17}$$

Substituting Equation (4.14) into Equations 4.16 and 4.17 and substituting absolute phases $\phi_{j,p}$ for phase differences $\Delta\phi_{j,p}$ according to

$$\Delta\phi_{j,pq} \equiv \phi_{j,p} - \phi_{j,q} = k_j(x_p - x_q) \tag{4.18}$$

will lead to the following equations for a_{Lj} and a_{Rj}

$$a_{Lj} = \sum_{p=1}^{P} C^*_{j,p}A_{j,p} \tag{4.19}$$

$$a_{Rj} = \sum_{p=1}^{P} C_{j,p}A_{j,p} \tag{4.20}$$

where

$$C_{j,p} = 2iW_{j,p}\frac{e^{i\phi_{j,1}}}{D}\sum_{p=1}^{P} W_{j,p}sin\Delta\phi_{j,pq}e_{i\Delta\phi_{j,pq}} \tag{4.21}$$

and

$$D = 4\sum_{p=1}^{P}\sum_{q<p} W_{j,p}W_{j,q}sin^2\Delta\phi_{j,pq} \tag{4.22}$$

In this equation $W_{j,p}$ is the weighting coefficient for wave gauge p at the jth frequency and can be defined as

$$W_{j,p} = \sum_{p=1}^{P}\frac{sin^2\Delta\phi_{j,pq}}{1 + (\Delta\phi_{j,pq}/\pi)^2} \tag{4.23}$$

This decomposition method can be applied at three locations in the flume, locations 1, 2 and 3 respectively. Due to the necessary distance between the 4 wave gauges, this method was not applicable on top of the merely 1 meter long reef. The spatial constraints of the measuring equipment make it impossible to install it at the location in question.

4.2.3 Comparison of decomposition methods

The two decomposition techniques described in the previous two sections were used to compare the results and determine whether one was preferable to the other. As stated before, both methods assume linear wave theory. The difference between the co-located decomposition method over the least square method is that the latter method assumes that the wave does not deform over the stretch where the array of wave gauges is present. This assumption is not needed for the first decomposition method.

To allow for comparison between the two methods, they have both been applied to the measured surface elevation time series to extract an incoming surface elevation time series. From these decomposed time series the variance density spectra was computed corresponding to the incoming signal only. With

use of this spectrum the incoming significant wave height could be calculated at location 2 and 3 for all tests performed in this study. These incoming significant wave heights were calculated with use of both separation techniques and the results were then plotted against each other in a scatter plot, as illustrated in Figure 4.1. To quantitatively assess the degree of agreement between the different

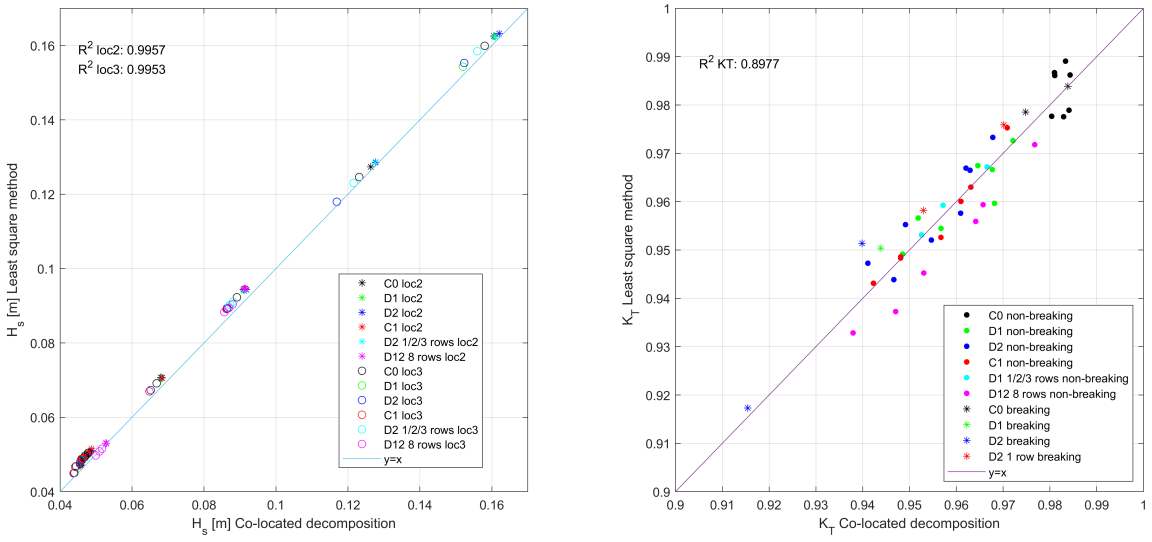

Figure 4.1: Two scatter plots of (left) the incoming significant wave height (H_s) and (right) the transmission coefficient (K_T) decomposed using two different methods at location 2 to 3 for all test cases, using both co-located decomposition and the least square method.

methods, the plots include the coefficient of determination (R^2). This is an measure of the degree of correlation and is computed according to Equation (4.24). The value ranges from 0-1 with values closer to 1 indicating a better fit, and values closer to 0 suggesting that the model does not explain much of the variation in the dependent variable.

$$R^2 = 1 - \frac{\sum_{i=1}^{N}(p_{1,i} - p_{2,i})^2}{\sum_{i=1}^{N}(p_{1,i} - \bar{p}_1)^2} \tag{4.24}$$

In this equation p_1 and p_2 denote the two data sets that are compared in the scatter and the over-bar represents the mean and N equals the total amount of data points. Figure 4.1 shows that the values for the incoming significant wave heights of both methods have a strong positive linear correlation. This can be determined visually, as the plot shows that the data points are closely located to the line y=x, but the coefficient of determination (R^2) also confirms this. At location 2 measurements $R^2 = 0.996$ and at location 3 $R^2 = 0.996$. These values are nearly identical and thus it can be said that there is no difference of the decomposed signals of both methods between the two locations.

Next to R^2 the root-mean-square error (RMSE) was calculated according to Equation (4.25).

$$\text{RMSE} = \sqrt{\frac{\sum_{i=1}^{N}(p_{2,i} - p_{1,i})^2}{N}} \tag{4.25}$$

The RMSE of incoming significant wave height is equal to 0.0024m for location 2 and 0.0023m for location 3. Dividing this RMSE by the mean H_s results in a relative RMSE. The relative RMSE equals 3.2% for both data sets, indicating that the RMSE is 3.2% of the mean value. Additionally the scatter plot reveals that, for the majority of the H_s values, the least square method produced larger

estimates compared to the co-located decomposition method. This can be quantified by computing the bias of the scatter plot. Which is done by taking the mean of the difference between all results according to:

$$\text{Bias} = \frac{\sum_{i=1}^{N}(p_{2,i} - p_{1,i})}{N} \tag{4.26}$$

In this case p_1 are the values of the least square method and p_2 are the values of the co-located method. The value of the bias for the incoming significant wave heights of all test cases equals -0.0022m, which substantiates the statement that the values of the least square method are systematically larger than the corresponding results obtained with use of the co-located decomposition technique.

With the extracted incoming wave heights at location 2 and 3, a transmission coefficient was computed for all individual tests according to $K_T = H_{s,i,3}/H_{s,i,2}$. The right side of Figure 4.1 shows a scatter plot of the calculated transmission coefficients K_T with use of both methods. The figure includes both breaking and non-breaking test cases.

This scatter plot too shows a relatively strong positive linear correlation between the K_T values of the two decomposition methods. However the linear relation is smaller than compared to the left hand side scatter plot, which is also true due to a smaller value for R^2 as $R^2 = 0.898$. The RMSE of this scatter plot equals 0.0048. Similarly as for the H_s scatter a relative RMSE error was computed, which equals 0.5%. Again the bias was measured for this scatter plot according to Equation (4.26). The value of the bias for the K_T scatter from Figure 4.1 equals -3.6E-04. Which is significantly closer to zero when compared to the bias of the scatter of the significant wave height (-0.0022m). This bias shows that there is no systematical difference between the two methods in terms of transmission coefficient.

After careful consideration of the results obtained using different methods of wave decomposition, a decision has been made to continue the research using the co-located decomposition method. While there were small discrepancies observed between the different methods, particularly when examining the transmission coefficient (K_T), the significantly small value of the bias of the K_T scatter shows no systematic under- or overestimation of the results. Another advantage to apply this method over the least square method is that incoming waves can be decomposed at more locations in the flume, respectively location 1-5, according to Figure 3.2.

4.3 Parameter definition

In this section definitions of the parameters used to analyse the results in Chapter 5 are given and explained. Reference tests have been performed with an empty flume, allowing for normalizing or subtraction with these values. How this is done will be elaborated in the following sections.

4.3.1 Normalized Transmission Coefficient

As stated in Chapter 2 the transmission coefficient K_T is a rate of the incoming significant wave height at location 3 downstream ($H_{s,i,3}$) to the incoming significant wave height at location 2 upstream ($H_{s,i,2}$). In equation:

$$K_T = \frac{H_{s,i,3}}{H_{s,i,2}} \tag{4.27}$$

The reference tests, meaning the tests where no artificial reef was present and the flume was empty, showed presence of dissipation. More detail on this is given in Section 6.3.2. However, to compare the results of different test cases with different wave conditions and thus different values for the dissipation as measured at the reference tests, the decision has been made to normalize the measured values to the values of the reference case. This is done by dividing the transmission coefficient of the specific test (K_T) where an artificial reef is present, by the transmission coefficient of the corresponding reference

test ($K_{T,ref}$).

$$K_{T,norm} = \frac{K_T}{K_{T,ref}} \tag{4.28}$$

where the transmission coefficient of the reference test ($K_{T,ref}$) is computed by:

$$K_{T,ref} = \frac{H_{s,i,3,ref}}{H_{s,i,2,ref}} \tag{4.29}$$

In the flume set-up, the wave gauge device that measures the upstream wave height is located at 2.3m in front of the start of the artificial reef (see Figure 3.2). Therefore, the measured wave height should all be equal for different tests with the same imposed wave conditions, regardless of whether an artificial reef was present or not; $H_{s,i,2} = H_{s,i,2,ref}$. This results in the following relationship:

$$K_{T,norm} = \frac{H_{s,i,3}/H_{s,i,2}}{H_{s,i,3,ref}/H_{s,i,2,ref}} = \frac{H_{s,i,3}}{H_{s,i,3}, ref} \tag{4.30}$$

Additionally, a reflection coefficient at location 2 can be calculated. This is done with use of the following equation

$$K_{R,2} = \frac{H_{s,r,loc2}}{H_{s,i,loc2}} \tag{4.31}$$

Here $K_{R,2}$ is the reflection coefficient, which represents the ratio between the reflected significant wave height at location 2 ($H_{s,r,loc2}$) and the incident significant wave height at location 2 ($H_{s,i,loc2}$)

4.3.2 Relative dissipation

From the variance density spectrum, the energy density spectrum can be computed according to:

$$E_{energy} = \rho g \int_0^\infty E_{variance}(f) df \tag{4.32}$$

In case of the flume, the waves of all frequency components propagate either in the positive or negative x direction, therefore the one-dimensional wave energy equation is

$$\frac{\partial F_j}{\partial x} = -\epsilon_{b,j} - \epsilon_{f,j} \tag{4.33}$$

$$F_j = E_j c_{g,j} \tag{4.34}$$

Here F_j is the energy flux per frequency component j, E_j is the wave energy density, $c_{g,j}$ the group velocity and $\epsilon_{b,j}$ and $\epsilon_{f,j}$ the rate of energy dissipation per unit area. In this part of the results, only non-breaking test cases will be researched, which translates to $\epsilon_{b,j} = 0$. The group velocity can be computed according to

$$c_{g,j} = \frac{1}{2}\left(1 + \frac{2k_j h}{sinh 2k_j h}\right)\frac{\omega_j}{k_j} \tag{4.35}$$

To determine a comprehensive value for the energy flux, or rate of dissipation that accounts for the entire frequency spectrum, all individual values corresponding to each frequency component are summed to derive a single value for the rate of dissipation, denoted by F and ϵ_f.

By measuring the change of the incoming energy flux and the transmitted energy flux around the artificial reef, the dissipation (ΔF) can be computed. This is done by taking a reference volume around the artificial reef and equating the incoming ($F_{i,2}$, $F_{r,3}$) and outgoing ($F_{r,2}$, $F_{i,3}$) energy fluxes from this reference volume. In equation form this is as follows:

$$\Delta F = F_{i,2} + F_{r,3} - F_{r,2} - F_{i,3} \tag{4.36}$$

Here the subscript i relates to the incoming spectrum and r the reflected spectrum. Subscript 2 and 3 indicate the location, as can be seen from Figure 3.2 location 2 corresponds to upstream from the reef and 3 downstream. From this equation a relative dissipation can be computed by dividing all individual fluxes by the incoming flux at location 2 as follows:

$$\frac{\Delta F}{F_{i,2}} = \frac{F_{i,2}}{F_{i,2}} + \frac{F_{r,3,}}{F_{i,2}} - \frac{F_{r,2}}{F_{i,2}} - \frac{F_{i,3}}{F_{i,2}} \tag{4.37}$$

This relative dissipation is thus a percentage of energy change compared to the incoming energy. A positive value for ΔF or $\Delta F/F_{i,2}$ corresponds to energy decrease, or dissipation.

Chapter 5 | Data Analysis

5.1 Wave transformation in the empty flume

The objective of this section is to acquire information on to the hydrodynamic behavior along the empty wave flume, in order to establish a level of quality control over the test outcomes. This preliminary step is critical in validating the integrity of the gathered data, prior to undertaking any subsequent analysis. During the research many tests have been performed corresponding to many different wave conditions. However, this section will concentrate on two test cases: a breaking case and a non-breaking case. The following two test cases have been used in this section, where the target wave conditions are as follow:

- Breaking: $R_c = 0.25m$, $H_s = 0.22m$, $T_p = 2.5s$ (h80H22T25)
- Non-breaking: $R_c = 0.25m$, $H_s = 0.10m$, $T_p = 2.5s$ (h80H10T25)

Figure 5.1 displays the variance density spectra of the two distinct experimental cases at location 2 and 3. This variance density spectrum is computed using the water elevation time series obtained from the measuring devices. Figure 5.1 shows that the spectrum transforms from location 2 to location 3. It also illustrates presence of dissipation in an empty flume, due to the difference in variance density spectra when comparing location 2 and 3.

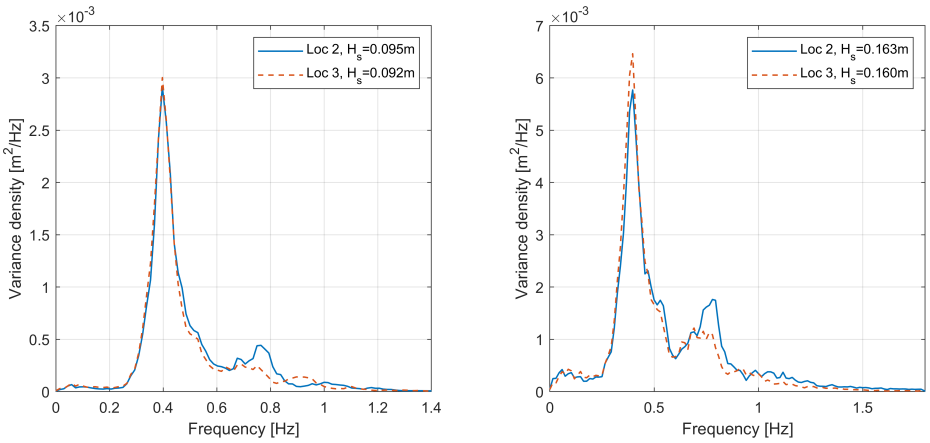

Figure 5.1: Wave spectrum of (left) a non-breaking test case with testID: h80H10T25 and (right) breaking test-case with testID: h80H22T25. Both plots show the variance density spectrum at location 2 (blue) and location 3 (red).

The significant wave height along the length of the flume, including both the total (blue) and incoming (red) wave height, is presented in Figure 5.2. It is noteworthy that the incoming wave height could only be extracted from the total time series at locations 1-5, resulting in fewer data points for these particular cases. As illustrated in the figure, the non-breaking test case (left) exhibited a small increase in wave height after passing over the bathymetry step. This phenomenon can be attributed to shoaling, resulting from the reduction in water depth. The shoaling coefficient corresponding to a bathymetry change is computed with:

$$k_{shoaling} = \sqrt{\frac{c_{g,1}}{c_{g,2}}} \tag{5.1}$$

With the values from the bathymetry change in the flume, the shoaling coefficient was calculated as 1.05. This coefficient is in line with the significant wave height increase from the total significant wave height test results, but not for the incoming significant test results. In contrast, the right plot reveals a decrease in significant wave height for the breaking test case, which can be attributed to wave breaking

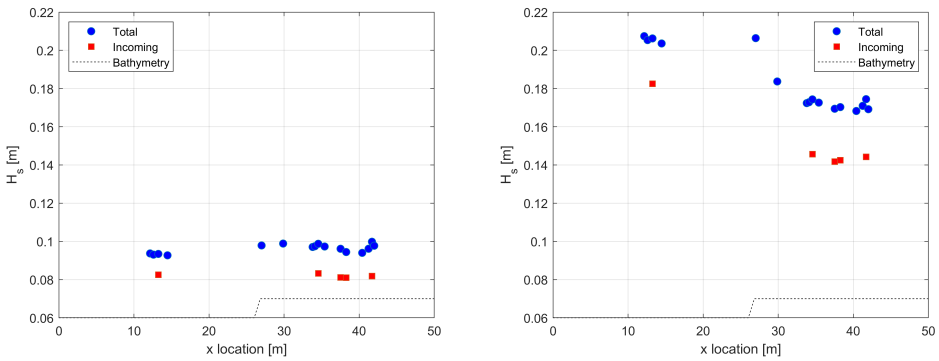

Figure 5.2: Variation in significant wave height along the flume, depicting (left) a non-breaking wave condition, corresponding to testID h80H10T25 and (right) a breaking wave condition corresponding to testID h80H22T25 test case. Distinguishing between total significant wave heights (blue) and incident significant wave heights (red). Bathymetry is represented for illustrative purposes only and is not to scale.

resulting from the decrease in water depth.

Additionally the wave set-up was obtained by computing the mean of the total surface elevation time series ($\bar{\eta}(x,t)$). Figure 5.3 shows the result of the set-up for both test cases. The values are in line with the theory, where waves start shoaling, set-down is measured, and where waves start breaking set-up is measured. The scatter of the data points in the right-hand figure is much greater than in the left-hand figure, which could be due to the fact that the y-axis scale yields a greater proportion of the total wave height in the right-hand figure ($H_s = 0.21m$) than in the left-hand figure ($H_s = 0.09m$). Noteworthy is that in the right-hand figure the measurement at x=42 results a significantly lower value than the group of measurements preceding it. This discrepancy might be due to the fact that this particular wave gauge exhibited unexpected deviations. Which was discovered when comparing the signal of this specific wave gauge (WHM13) to the signals of the wave gauges in front (WHM11, WHM12, WHM93). More information about this signal disturbance can be found in Appendix D. It is important to note that this deviating signal was only present at this specific wave gauge and only for a few tests.

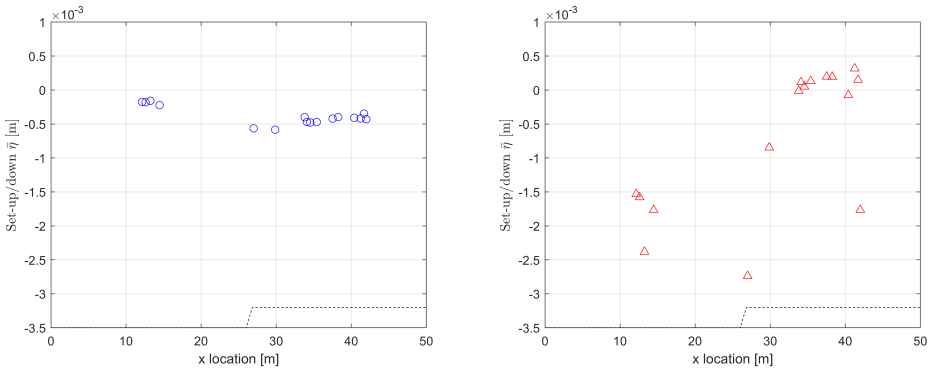

Figure 5.3: Set-up and set-down along the flume, depicting (left) a non-breaking test case with testID h80H10T25 and (right) a breaking test case with testID h80H22T25 test cases. Bathymetry is represented for illustrative purposes only and is not to scale.

Lastly the root mean square (rms) orbital velocity has been calculated according to:

$$U^{rms}(z) = \sqrt{\frac{1}{t_{end} - t_0} \int_{t_0}^{t_{end}} u(z)^2 dt} \tag{5.2}$$

Here U^{rms} gives a value averaged over the full time series. The root-mean-square (rms) orbital velocities for both breaking and non-breaking test cases are illustrated in Figure 5.4. The figure displays an increase in orbital velocity when comparing values in front of the foreshore (i.e., location 1) to those above the foreshore (i.e., locations 2-5). This can be attributed to the smaller water depth (h) at the latter locations, as the foreshore bed is +0.4 m higher than the flume bed, therefore the measurement at location 1 is performed at another depth of the velocity profile than at locations 2-5. The figure also reveals an increase in U^{rms} when comparing locations 2 (x=34.5m) and 3 (x=41.7m) to locations 4 (x=37.5m) and 5 (x=38.3m). This can be explained by the vertical positioning of the EMS devices. The z coordinates of the EMS measurements are as follows: location 1 z=0.05 m, locations 2 and 3 z=0.45m, and locations 4 and 5 z=0.65 m. All z coordinates are measured such that z=0 corresponds to the flume bed. Consequently, the devices at locations 4 and 5 measure the rms orbital velocity higher up in the flow velocity profile, resulting in larger values than those measured at locations 2 and 3.

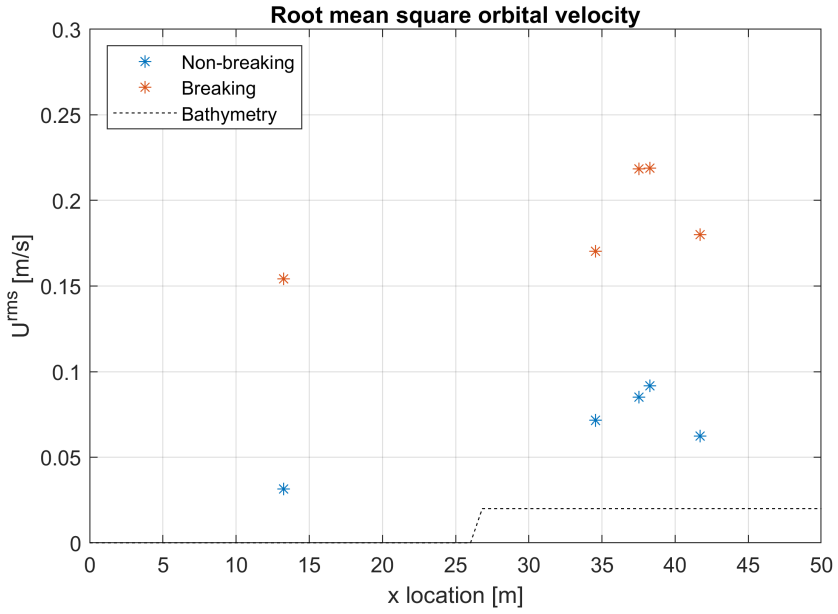

Figure 5.4: Root mean square orbital velocity $U^{rms}(z)$ [m/s] values along the flume length, depicting non-breaking (blue) and breaking (red) test cases with testID h80H10T25 and h80H22T25 respectively. The bathymetry is represented for illustrative purposes only and is not to scale.

5.2 Wave transmission over the artificial reef

In this section the measurements concerning the wave transmission coefficient are analysed. The first section focuses on the transmission coefficient of all tests combined, where no distinction between the wave conditions has been made. Later the influence of different wave parameters on the normalised transmission coefficient is studied and analysed.

5.2.1 Overall comparison of Transmission coefficient

Figure 5.5a shows an overview of the transmission coefficient calculated according to equation 4.27. The data set used to generate the box plot includes only to the wave conditions that were applied on all three structures. This corresponds to seven non-breaking test cases, as can be found in an overview in Table 5.1. The box plot does not allow for differentiation between various wave conditions.

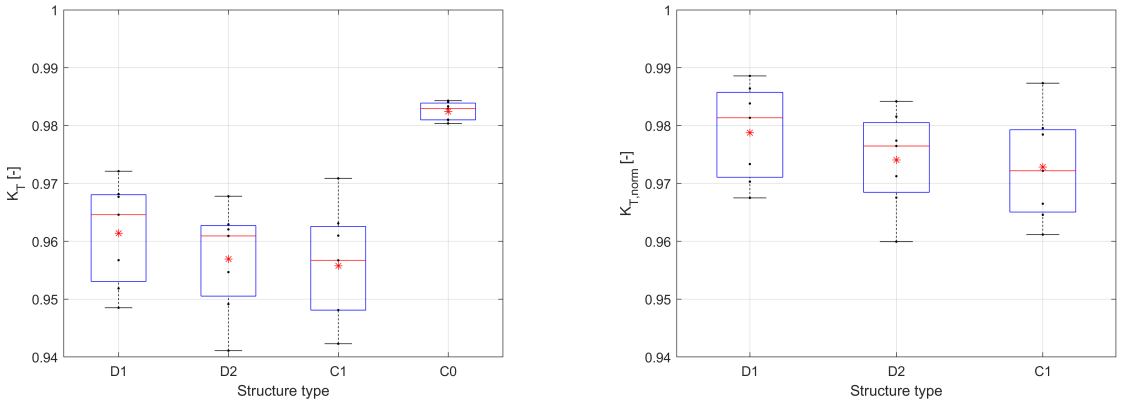

(a) *(b)*

*Figure 5.5: Box-plot of (a) K_T and (b) $K_{T,norm}$ computed over location 2 to 3. Only the tests that have been performed for each of the 3 structure types (D1, D2, C1) are plotted, resulting in exactly 7 data points per structure type. Corresponding to non-breaking cases only. The red line indicates the value of the median, while the red *-sign indicates the value of the mean*

It is noticeable that the K_T values of the reference tests (C0) have a relatively narrow range of data points when compared to the three structures (Design 1, Design 2 and Cubes). This observation suggests that transmission is relatively consistent across the baseline tests conducted in the absence of structures, and therefore no external factors appear to affect transmission. However, the figure does show some dissipation in the empty channel experiments, as the transmission coefficient range from 0.980 to 0.984, with a mean of 0.982. Nevertheless, the transmission in the empty channel experiments remains significantly higher than that observed in the presence of structures. Therefore, it can be concluded that the transmission in the empty channel experiments does not significantly affect the transmission coefficients associated with the other structures.

	TestID	h [m]	H_s [m]	T_p [s]	L [m]	h/H_s	H_s/L
1.	h70H5T5	0.3	0.05	4.9	8.38	6.2	0.006
2.	h75H5T5	0.35	0.05	5.2	9.51	7.4	0.005
3.	h80H5T5	0.4	0.05	5.2	10.12	8.4	0.005
4.	h80H5T4	0.4	0.05	4.1	8.00	8.5	0.006
5.	h80H5T25	0.4	0.05	2.5	4.70	8.6	0.010
6.	h80H75T25	0.4	0.07	2.5	4.74	5.9	0.014
7.	h80H10T25	0.4	0.09	2.5	4.74	4.4	0.019

Table 5.1: Overview of the seven non-breaking test cases that have been applied to all 3 structure types, h represents the water depth at the wave paddle, H_s the significant wave height at location 2, T_p the peak period at location 2, L the local wave length, h/H_s the relative water depth and H_s/l the wave steepness.

Figure 5.5b presents a box plot of the normalized transmission coefficient, as calculated by using Equation (4.28). Both box plots indicate that the transmission coefficients for the three structures span a similar range. The right-hand-side plot demonstrates that normalizing the data does not significantly impact the order of the mean and median. The median and mean values reveal that design 1 yields the highest values (mean $K_T = 0.961$ and $K_{T,norm} = 0.979$), while design 2's values are slightly lower (mean $K_T = 0.957$ and $K_{T,norm} = 0.974$), and the values for the cubes are the lowest (mean $K_T = 0.956$ and $K_{T,norm} = 0.973$). However, the difference between the structures is minimal, amounting $O(10^{-3})$.

5.2.2 Relative water depth

The relative water depth, defined as the ratio of water depth to significant wave height, can be expressed as h/H_s. Figure 5.6 demonstrates the influence of relative water depth on transmission and indicates that the transmission coefficient increases as relative water depth increases. An increase in relative water depth can be achieved through either an increase in water depth or a decrease in significant wave height. The lowest value of the normalised transmission coefficient is 0.966, corresponding to a relative water depth of $h/H_s = 6.2$ for the cubes, and the highest value is 0.989, corresponding to a relative water depth of $h/H_s = 8.4$ for design 1.

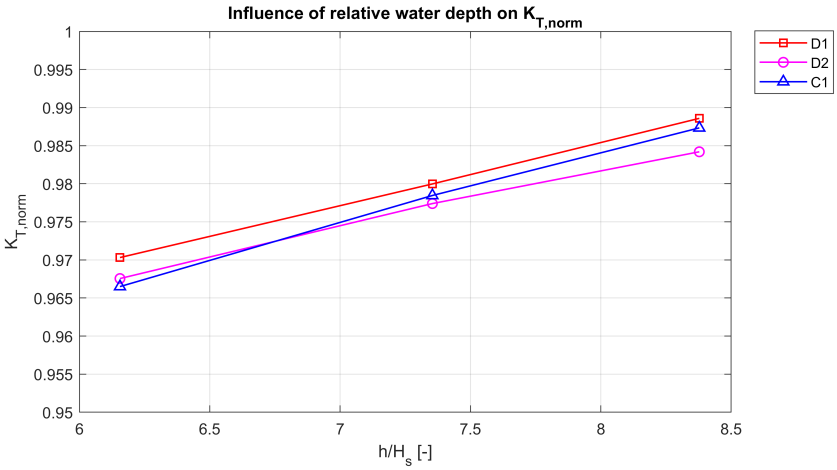

Figure 5.6: Influence of the relative water depth on the normalised wave transmission coefficient ($K_{T,norm}$) depicting the three different structures: Design 1 (red), Design 2 (pink), Cubes (blue).

Overall, the conducted tests demonstrate highly comparable results in the normalised transmission coefficient. The obtained values are of the same order of magnitude, indicating that no significant distinction can be established between the three distinct structure types. The plot shows that the line associated with the results of Design 1 (red) always lies above the line of Design 2 (pink).

5.2.3 Incoming wave steepness

Additionally the effect of incoming wave steepness to the normalised transmission coefficient was evaluated, where the incoming wave steepness corresponds to a ratio of significant wave height to the local wave length, according to H_s/L_{op}. Where L_{op} was computed according to

$$L_{op} = 2\pi/k \tag{5.3}$$

The wave number, denoted as k, is computed using an accurate approximation formula based on the linear dispersion relation and the approximation method proposed by Guo (2002). The effect of incoming wave steepness on the transmission coefficient is illustrated in Figure 5.7. The figure indicates a decrease in the transmission coefficient as wave steepness increases. The wave steepness is increased

by reducing the peak period (T_P), or by increasing the significant wave height (H_s) which both lead to shorter wave lengths and a higher degree of steepness. Again the three structures show similar magnitude of order in transmission coefficient and again the results of design 1 are systematically larger than the results of design 2.

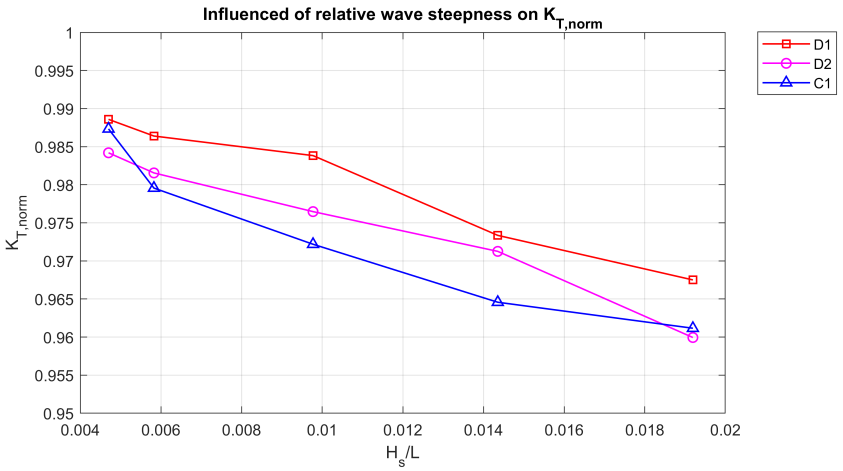

Figure 5.7: Influence of the incoming wave steepness on the wave transmission coefficient (K_T) depicting the three different structures: Design 1 (red), Design 2 (pink), Cubes (blue).

5.2.4 Relative reef length

The relative reef length, denoted as B/L, is defined as the ratio of reef length (B) to the local wave length (L). To investigate the impact of the reef length on the relative transmission coefficient, the length of the reef (B) was adjusted. The outcomes of these investigations are presented in Figure 5.8, which includes the 5 data points corresponding to the test case involving 1, 2, 3, and 4 rows of structure D2 and 8 rows comprising structures D1 and D2. The wave parameters, including the water depth (h), the significant wave height (H_s), and the peak period (T_P), have been kept constant at 0.4 m, 0.1 m, and 2.5 s, respectively.

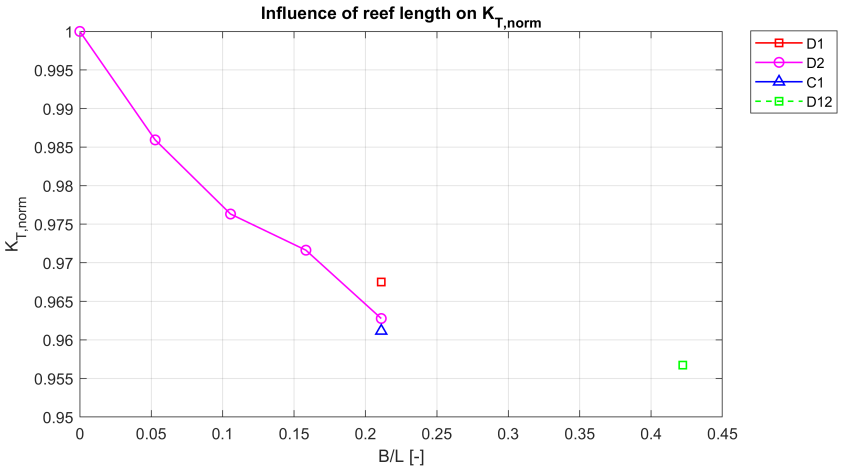

Figure 5.8: Influence of the relative reef length on the wave transmission coefficient (K_T) depicting the three different structures: Design 1 (red), Design 2 (pink), Cubes (blue). Also including an 8-row-long reef comprised of both structures D1 and D2 (green)

The results presented in the figure indicate that as the reef length increases, the wave transmission decreases. However, the rate of decrease varies with the reef length. Specifically, the decrease in wave transmission is relatively consistent when increasing from 0 row to 4 rows of the artificial reef, but the rate of decrease is less pronounced and does not follow the same trend when increasing up to 8 rows (B/L=0.42).

5.2.5 Reef set-up/density

To obtain information on the influence of reef set-up on transmission, three distinct set-ups were tested, where the reef coverage decreased from 100% to 63% to 31%. The reef coverage was computed according to the following equation:

$$Cov. = \frac{N_{structures}}{N_{max}} \tag{5.4}$$

In this equation $N_{structures}$ depicts the amount of structures that compose the reef and N_{max} is the maximum amount of structures that could fill that stretch of the reef. In the case of the wave flume of Deltares, this means that for a length of 2m and a fixed width of 1m the maximum amount of structures equals 32. See Figure 3.5(g) for a visual representation of this situation.

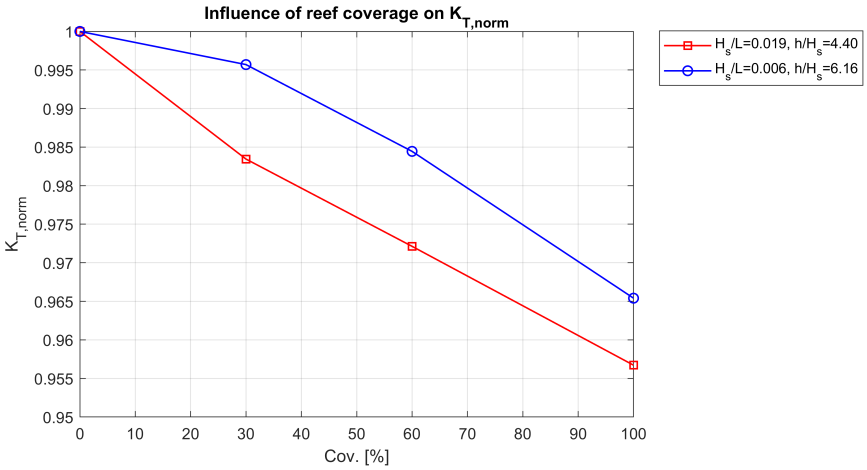

Figure 5.9: Influence of the reef coverage on the normalised wave transmission coefficient (K_T) depicting two different wave conditions. The reef stretches 2m and is comprised of both design 1 and 2 according to RL8-D12-A, RL8-D12-B, RL8-D12-C

Figure 5.9 illustrates the outcomes obtained from two distinct wave conditions, characterized by different values of the incoming wave steepness, H_s/L, and relative water depth, h/H_s. The plot demonstrates a decline in transmission as reef coverage increases. Notably, this decrease in transmission exhibits a similar trend in both test cases. However, the absolute value of the transmission is comparatively lower in the scenarios characterized by high wave steepness and lower relative water depth (red) than compared to the test case characterized by a low wave steepness and high relative water depth.

5.2.6 Combining wave parameters

Figure 5.10 depicts the impact of wave steepness (H_s/L) and relative water depth (h/H_s) on normalised wave transmission. The plot reveals that the normalised wave transmission is maximal when the relative water depth is highest and wave steepness is smallest. Conversely, transmission is minimal when water depth is lower and wave steepness is greater. Comparing the three figures, it is clear that there is no significant difference between the three structures in terms of maximum and minimum $K_{T,norm}$ values. However, as noted in the previous sections, the values of design 2 are all systematically lower than

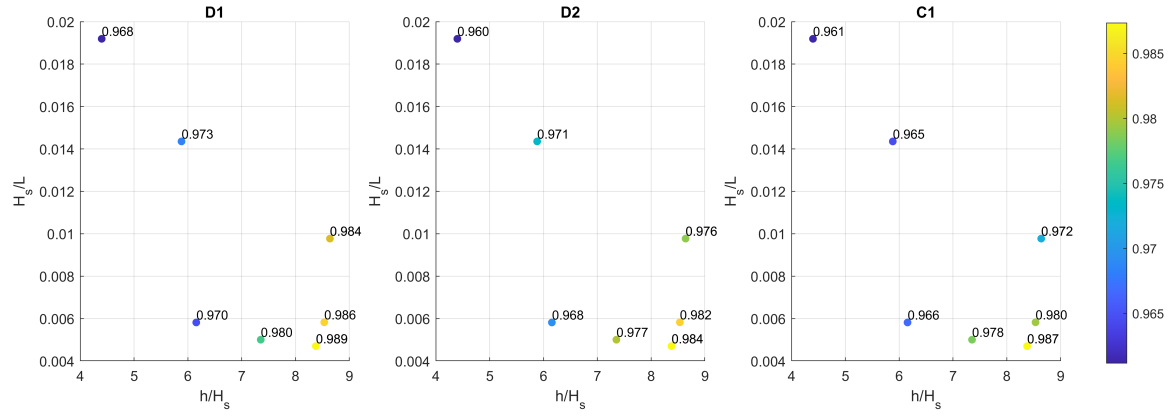

Figure 5.10: The effect of wave steepness H_s/L and relative water depth h/H_s on the normalized transmission coefficient K_T for the three structure types: design 1 (D1), design 2(D2) and cubes (C1)

those of design 1. This figure also shows that all values belonging to the cubes results are larger than the corresponding values of design 2. To quantify this systematic difference among the three structures a percentage difference can be computed according to:

$$\Delta K_T = \frac{\sum \left(\frac{K_{T,3} - K_{T,2}}{K_{T,2}} \right)}{N} \cdot 100\% \tag{5.5}$$

Here N denotes the total amount of results to be compared, which in this case is equal to 7. ΔK_T represents an average difference between two distinct structure types in percentage. ΔK_T has been computed with use of Equation (5.5), and the values show that indeed the results of design 1 show the largest values, because compared to design 2, the difference of the normalised K_T is 0.45% and compared to the cubes even 0.60%. When comparing the results of design 2 with the cubes, the value shows that the normalised K_T values of the cubes is just only -0.11% lower than those of design 2. Additionally, as can be seen from Figure 5.10 not all values are systematically lower for the cubes results compared to the corresponding values of the design 2 results. Some are larger for design 2 results than for the cubes test.

5.2.7 Summary wave transmission

- Overall comparison of the (normalised) transmission coefficients revealed no significant difference between the three structures. Design 1 exhibited the highest mean values for K_T and $K_{T,norm}$, while Design 2 and the cubes demonstrated slightly lower values. The difference between the structures was minimal, amounting to O(10^{-3}).
- The influence of relative water depth (h/H_s) on transmission showed an increase in the normalised transmission coefficient as relative water depth increased. The difference between the structures remained minimal.
- The effect of incoming wave steepness (H_s/L) on transmission indicated a decrease in the normalised transmission coefficient as wave steepness increased. Design 1 consistently showed higher results than Design 2, but the overall magnitude of order in normalised transmission coefficient was similar for all three structures.
- The impact of reef length on the normalised transmission coefficient revealed a decrease in wave transmission as the reef length increased. The rate of decrease was relatively constant from 0 to 4 rows, but the reef comprised of 8 rows did not follow the same trend.
- The influence of reef set-up on transmission demonstrated a decline in transmission as reef coverage increased. This trend was consistent across different wave conditions.

- The combined impact of wave steepness and relative water depth on the normalized wave transmission showed that transmission is maximal when the relative water depth is highest and wave steepness is smallest, and minimal when water depth is lower and wave steepness is greater.

5.3 Spectral evolution and dissipation

This section presents an investigation into the spectral dissipation of artificial reefs. The dissipation values were first calculated for all non-breaking test cases to enable comparison between different reef structures. In addition, two test cases were selected for a detailed analysis. Finally, the influence of different reef configurations on dissipation was examined.

5.3.1 Overall comparison of spectral dissipation

In Figure 5.11(a), the wave energy dissipation, as computed according to Equation (4.36), of all seven non-breaking test cases is presented per structure type. The mean dissipation values for the empty flume cases are significantly lower (mean(C0)=0.09$J/m^3/s$) compared to the structure tests (mean(D1)=0.23 $J/m^3/s$, mean(D2)=0.25 $J/m^3/s$ and mean(C1)=0.25 $J/m^3/s$), which indicates that the presence of structures has an influence on the dissipation. The range of dissipation for the empty flume tests lies between 0.04 $J/m^3/s$ and 0.18 $J/m^3/s$, indicating a variation in dissipation depending on the wave condition. In Figure 5.11(b) values for the relative dissipation have been plotted (Equation (4.37)) for the same seven non-breaking test conditions. The values presented in the right-hand figure (b) display a similar increase in mean relative dissipation values for the different structure types as compared to the left-hand figure (a). The outliers in the box plot are less extreme in relation to the range of data points because the dissipation has been related to the incoming energy flux at location 2. The mean values for relative dissipation in the right-hand figure (b) are mean(D1)=8.4%, mean(D2)=9.0%, and mean(C1)=9.0%. The empty flume relative dissipation is a factor 2 smaller, mean(C0)=3.6%. In both figures, the mean values are equal for D2 and C1, while the mean value for D1 is smaller by a fraction, namely 0.02 $J/m^3/s$ and 0.6 %.

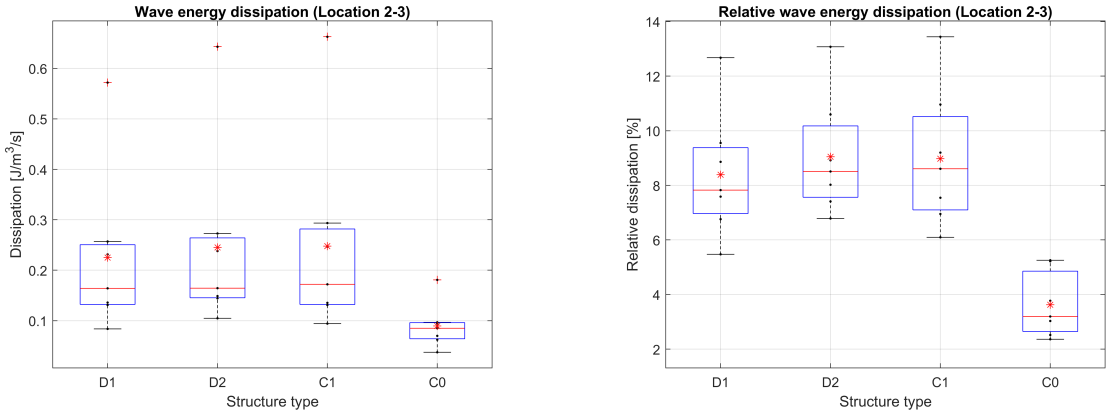

(a) *(b)*

*Figure 5.11: Box plots showing (a) an overview of wave energy dissipation for all non-breaking tests per structure type: Design 1 (D1), Design 2 (D2), Cubes (C1), empty flume (C0) over location 2 to 3. On the right plot (b) the relative dissipation is plotted. The red line indicates the location of the median, the red *-sign the location of the mean and the +-sign represents outliers.*

Figure 5.12 presents a bar chart depicting the relative dissipation values for the seven non-breaking test cases in relation to three distinct structure types (D1, D2, C1), as well as the reference case (C0). This chart exhibits the distribution of relative dissipation values across various test cases. The highest percentage of relative dissipation is observed in the test case with TestID h70H5T5 for all three

structure types, while the lowest relative dissipation value is identified in the test case with TestID h80H5T25. Additionally, the chart demonstrates the variation in relative dissipation for the reference tests across different test cases. A more comprehensive analysis of this phenomenon can be found inSection 6.3.2.

When comparing the three structures, there is no significant difference in absolute values. In almost all cases, design 1 resulted the smallest relative dissipation, however the difference is minimal. In test case h75H5T5, design 1 and design 2 show the same result and in test case h80H5T4 the cubes show a smaller result than design 1. It is noticeable that in the latter test case, the empty flume dissipation is relatively large compared to the dissipation when structures are present.

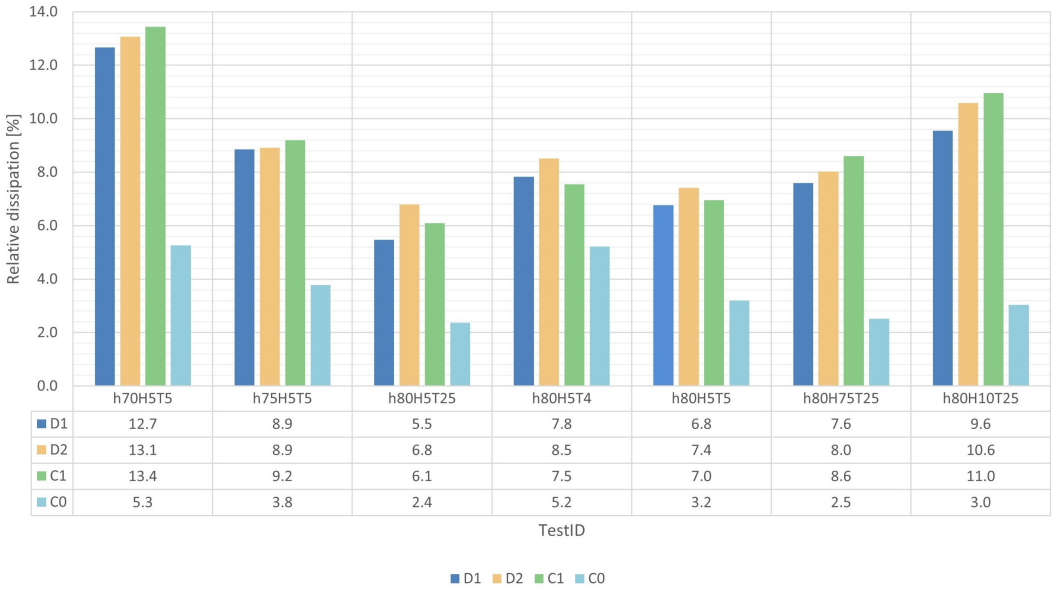

Figure 5.12: Bar chart of the relative dissipation of all seven non-breaking test cases per structure type: Design 1 (D1), design 2 (D2), cubes (C1) and empty flume (C0). Including a data table of the corresponding numbers, values are in %.

5.3.2 Analysis characteristic wave periods

The two test cases resulting the largest dissipation correspond to h70H5T5 and h80H10T25 (see Figure 5.12). Figure 5.13 shows the incident energy density spectra at location 2 and 3 per structure type (D1, D2, C1) and the reference case (C0) for test case h70H5T5. The wave parameters measured at location 2 for this test case corresponds to $R_c = 0.15m$, $H_s = 0.05m$, $T_p = 5s$. All four plots show a decrease of wave energy at the peak frequency, which equals $f_{peak} = 0.2Hz$ for the current test case, and an increase in energy at the higher frequencies, specifically around the first and second harmonic ($f = 0.4Hz$ & $f = 0.6Hz$).

The transformation of energy from the peak frequency towards the higher frequencies is also confirmed when comparing the mean wave period ($T_{m_{0,1}}$) and mean energy period ($T_{m_{-1,0}}$) at location 2 and 3. When comparing these characteristic wave periods of location 2 with location 3, the empty flume test shows that the mean wave period decreases from 3.17s to 2.67s and the mean energy period decreases from 4.20s to 3.80s. This indicates that there is an energy shift from the lower frequencies to the higher frequencies in the empty flume. An overview of the difference between these periods is presented inTable 5.2. The recorded values in the table suggest that the presence of the structures exerts an effect on the incoming spectrum such that the energy shift towards higher frequencies is more pronounced than that observed in the empty flume test, as evidenced by a greater decrease in periods.

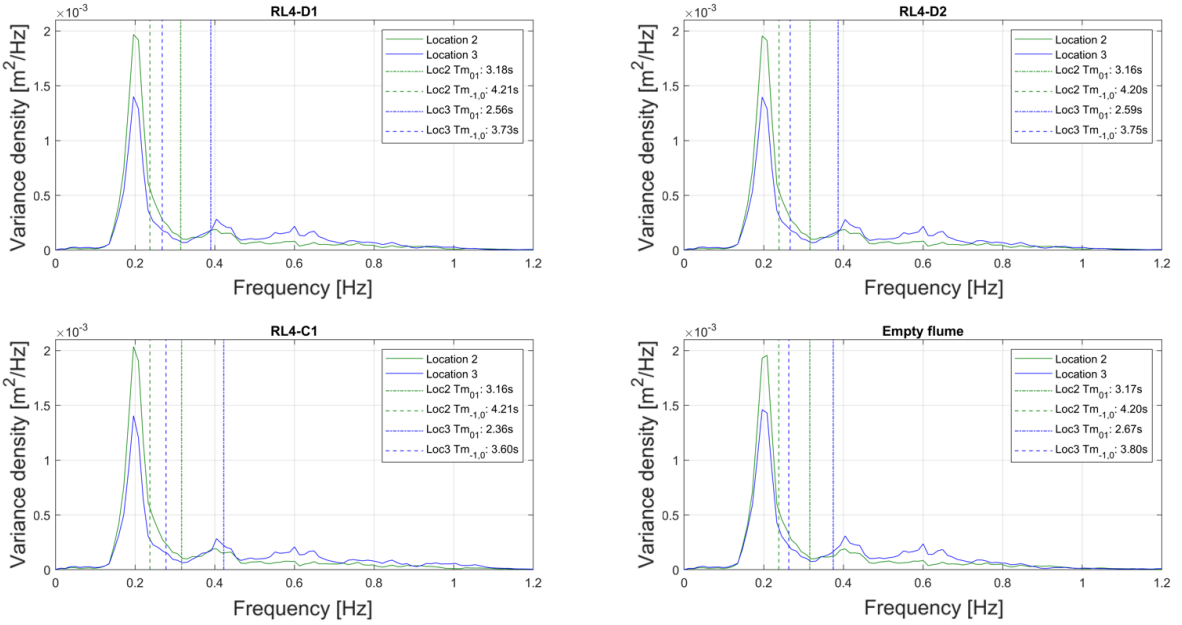

Figure 5.13: Plot of the incident energy density spectra at location 2 (green line) and 3 (blue line) per structure type: D1 (top left), D2 (top right), C1 (bottom left) and the reference case C0 (bottom right) for test case h70H5T5. The wave conditions for this test case correspond to $R_c = 0.15m$, $H_s = 0.05m$, $T_p = 5s$. The graphs also depict the mean wave period ($T_{m_{0,1}}$) and mean energy period ($T_{m_{-1,0}}$).

The energy shift to higher frequencies indicates waves with smaller periods are transmitted more compared to waves with larger periods. Among the three structure types, the difference in mean wave period is largest for the cubes, with $\Delta T_{m_{0,1}} = -0.61$ and smallest for design 2, with $\Delta T_{m_{0,1}} = -0.45$, and similarly the difference in mean energy period again is largest for the cubes, with $\Delta T_{m_{-1,0}} = -0.80$ and again smallest for design 2, with $\Delta T_{m_{-1,0}} = -0.45$. The difference between the different tests is fairly small, in the order of $O(10^{-1})$s.

	$\Delta T_{m_{0,1}}$ [s]	$\Delta T_{m_{-1,0}}$ [s]
Design 1	-0.62	-0.48
Design 2	-0.57	-0.45
Cubes	-0.80	-0.61
Empty flume	-0.50	-0.40

Table 5.2: Difference of mean wave period $\Delta T_{m_{0,1}}$ and mean energy period $\Delta T_{m_{-1,0}}$. Calculated by subtracting the incoming value (location 2) from the transmitted value (location 3). A positive value indicates an increase and a negative value a decrease. Corresponding to test case h70H5T5.

Similarly, Figure 5.14 shows the incident energy density spectra at location 2 and 3 per structure type (D1, D2, C1) and the reference case (C0), however now for test case h80H10T25. The wave parameters measured at location 2 for this test case corresponds to $R_c = 0.25m$, $H_s = 0.09m$, $T_p = 2.5s$. The three plots corresponding to the three structures show a decrease of wave energy at the peak frequency, which equals $f_{peak} = 0.4Hz$ for the current test case. The empty flume test does not show a similar decrease in energy at the peak frequency. This indicates that the structures induce dissipation around the peak frequency. Additionally all four graphs depict an energy shift at around f=0.75Hz towards f=0.85Hz.

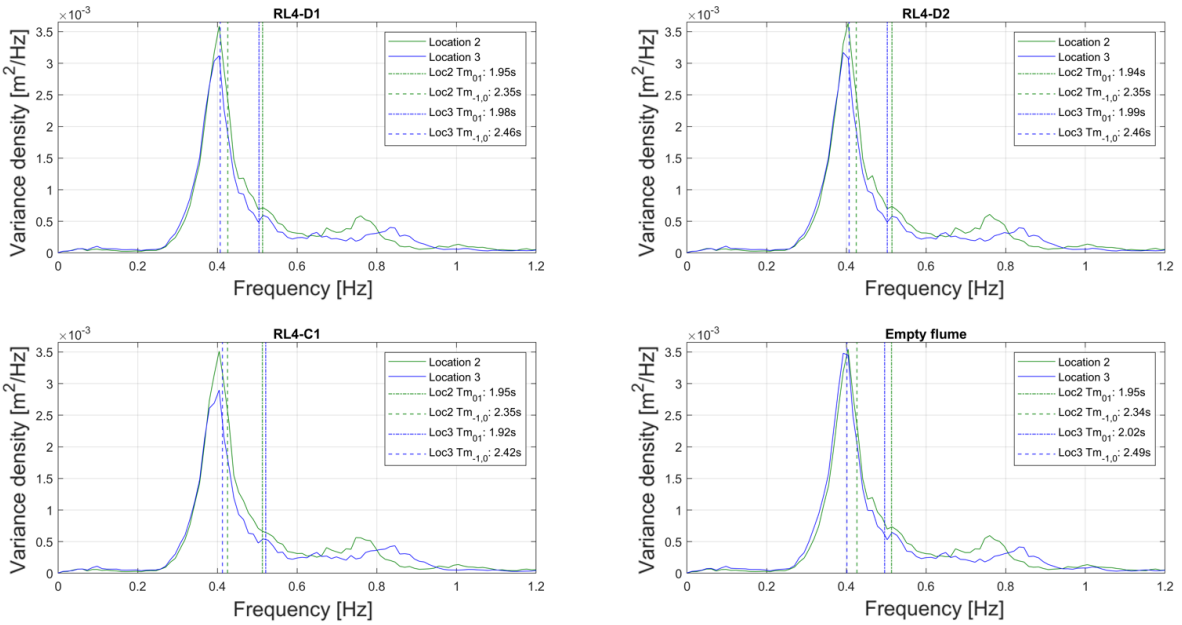

Figure 5.14: Plot of the incident energy density spectra at location 2 (green line) and 3 (blue line) per structure type: D1 (top left), D2 (top right), C1 (bottom left) and the reference case C0 (bottom right) for test case h80H10T25. The wave conditions for this test case correspond to $R_c = 0.25m$, $H_s = 0.09m$, $T_p = 2.5s$. *The graphs also depict the mean wave period (*$T_{m_{0,1}}$*) and mean energy period (*$T_{m_{-1,0}}$*).*

Again the mean wave period and mean spectral period have been computed and plotted in the figures as well. The empty flume test shows that the mean wave period increases from 1.95s to 2.02s and the mean energy period increases from 2.34s to 2.49s. This indicates that in the empty flume energy is transferred towards lower frequency. Again the differences between these characteristic wave periods of location 2 to location 3 of the four test cases have been computed and are provided in Table 5.3.

	$\Delta T_{m_{0,1}}$ [s]	$\Delta T_{m_{-1,0}}$ [s]
Design 1	0.03	0.11
Design 2	0.05	0.11
Cubes	-0.03	0.07
Empty flume	0.07	0.15

Table 5.3: Difference of mean wave period $\Delta T_{m_{0,1}}$ *and mean energy period* $\Delta T_{m_{-1,0}}$. *Calculated by subtracting the incoming value (location 2) from the transmitted value (location 3). A positive value indicates an increase and a negative value a decrease. Corresponding to test case h80H10T25.*

This table shows that the difference in mean wave period as well as mean energy period for the three structure types is smaller than for the empty flume, indicating that the transmitted (i.e. at location 3) mean wave and energy period is smaller for tests including a structure than the empty flume test, as the incoming period is (almost) equal for all cases. This implies that the presence of a structure influences the transmitted spectrum such that the energy shifts towards higher frequencies when comparing to the reference case, meaning that smaller waves are transmitted more due to the structures compared to an empty flume.

In Figure 5.15 (a) the ratio of the transmitted (i.e. at location 3) mean energy period of a specific structure ($T_{m_{-1,0}(structure)}$) divided by the mean energy period of the corresponding reference test ($T_{m_{-1,0}(empty)}$) is visualised in a scatter plot. The figure shows that the values are systematically smaller than 1, which indicates that including a structure in the flume reduces the mean energy period with respect to the period without a structure present. In other words, adding a structure will result in a shift of the energy towards the higher frequencies. Additionally Figure 5.15 (b) illustrates that the range of the mean energy period is largest for the cubes test, while it is smaller for design 1 and design 2 results. The mean of the scatter is largest for design 2 tests, with mean(D2)= 0.989, then design 1, with mean(D1)=0.986 and smallest for the cubes tests, with mean(C1)= 0.977. It should be noted however that the differences are very small.

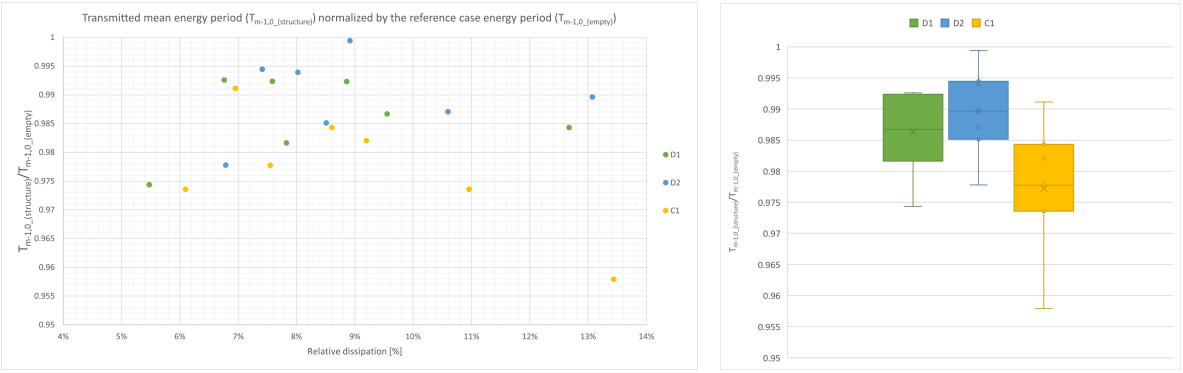

Figure 5.15: (a) Scatter plot of the transmitted (i.e. at location 3) mean energy period of a specific structure ($T_{m_{-1,0}(structure)}$) divided by the mean energy period of the corresponding reference test ($T_{m_{-1,0}(empty)}$) versus the relative spectral dissipation for the seven non-breaking test cases. (b) shows the box plot belonging to the scatter plot, to visualize the range in scatter. Both plots differentiate between the three structures: design 1 (D1), design 2 (D2) and cubes (C1)

5.3.3 Influence of reef lay-out on spectral dissipation

Multiple reef configurations were examined by modifying the reef coverage (labelled as RL8-D12-A, RL8-D12-B, and RL8-D12-C), where structures were removed resulting in a checkered pattern of reef lay-out (see Figure 3.5 and 3.6). The tests where the reef coverage was adjusted were conducted under two sets of wave conditions, namely (1) $R_c = 0.15m$, $H_s = 0.05m$, $T_p = 5s$ (h70H5T5) and (2) $R_c = 0.25m$, $H_s = 0.1m$, $T_p = 2.5s$ (h80H10T25).

The incoming energy density spectra at location 3 corresponding to the three reef lay-outs and the reference test of the empty flume are presented in Figure 5.16a. The difference in wave spectra reveals that an increase in reef coverage leads to a larger decrease in the peak frequency $f_{peak} = 0.4Hz$, while at the same time increasing the first harmonic $2f_{peak} = 0.8Hz$. Nevertheless, the increment of energy in the first harmonic is considerably smaller than the reduction at the peak. Additionally, the figure illustrates how the mean energy period adjusts according to the different reef settings. It shows that the incoming mean energy period (at location 2) equals 2.35s. The transmitted mean energy periods (at location 3) for all reef configurations are larger than the incoming, with $T_{m_{-1,0}(RL8-D12-A)} = 2.43s$, $T_{m_{-1,0}(RL8-D12-B)} = 2.46s$, and $T_{m_{-1,0}(RL8-D12-C)} = 2.47s$. Nevertheless, the empty flume test resulted in the largest value, namely $T_{m_{-1,0}(empty)} = 2.49s$. Therefore, it can be said that the transmitted mean energy period is affected by the presence of the reef and that it tends to decrease for increasing reef coverage, when compared to the empty flume test. In general, the transmitted mean period increases compared to the incoming mean energy period, but this increment reduces with larger reef coverage for this specific wave condition. An increase in mean energy period indicates that the energy shifts towards the lower frequencies and thus waves with smaller periods are transmitted.

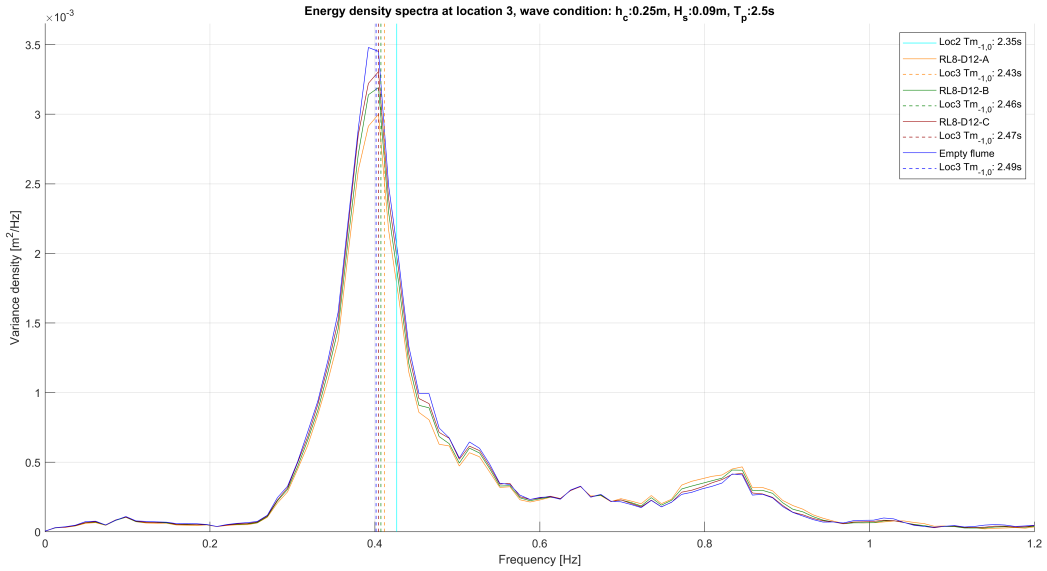

(a)

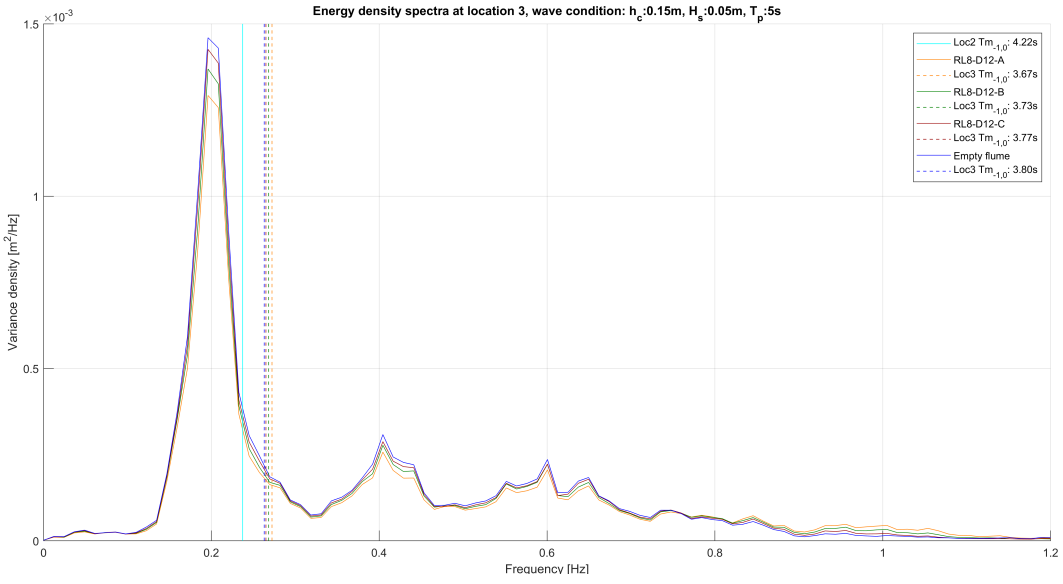

(b)

Figure 5.16: Energy density spectra at location 3 of decreasing reef coverage: RL8-D12-A=100%, RL8-D12-B=62.5%, and RL8-D12-C=31.25%. (a) Corresponding to the test cases with wave condition $R_c = 0.25m$, $H_s = 0.1m$, $T_p = 2.5s$ (h80H10T25) and (b) Corresponding to wave conditions $R_c = 0.15m$, $H_s = 0.05m$, $T_p = 5s$ (h70H5T5). Also including the incoming (at location 2) and transmitted (at location 3) mean energy periods ($T_{m_{-1,0}}$)

Similarly Figure 5.16b shows the same figure, but for test case h70H5T5 ($R_c = 0.15m$, $H_s = 0.05m$, $T_p = 5s$). Again the figure shows that an increase in reef coverage results in a larger decrease at the peak frequency $f_{peak} = 0.2Hz$, while at the same time a decrease in the first harmonic, or $2f_{peak} = 0.4Hz$. Again, the figure illustrates how the mean energy period adjusts according to the different reef settings. It shows that the incoming mean energy period (at location 2) equals 4.22s. The transmitted mean energy periods (at location 3) for all reef configurations are smaller than the incoming, with $T_{m_{-1,0}(RL8-D12-A)} = 3.67s$, $T_{m_{-1,0}(RL8-D12-B)} = 3.73s$, and $T_{m_{-1,0}(RL8-D12-C)} = 3.77s$. But, the empty flume test resulted in the largest value, namely $T_{m_{-1,0}(empty)} = 3.80s$. Therefore, it can be said that the transmitted mean energy period is affected by the presence of the reef and that it tends to decrease for increasing reef coverage. In general, the transmitted mean period decreases compared to the incoming mean energy period, but this reduction increases with increasing reef coverage for this specific wave condition. A decrease in mean energy period indicates that the energy shifts towards the higher frequencies and thus waves with larger periods are transmitted.

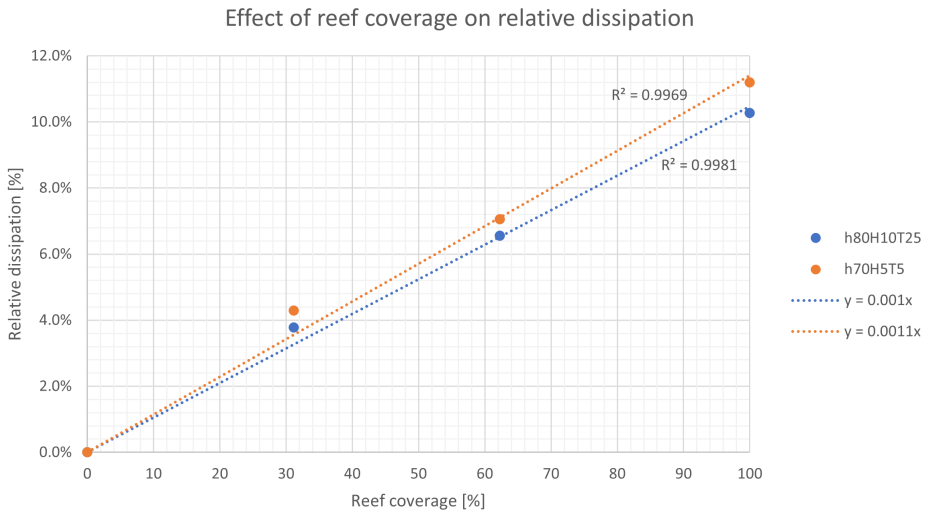

Figure 5.17: Figure showing the relationship between relative dissipation and reef coverage for two distinct test cases, namely h70H5T5 (orange) and h80H10T25 (blue). Including the linear trend lines, and their corresponding equation. The empty flume dissipation belonging to the currents test cases has been subtracted from the values such that a reef of 0% coverage results 0% relative dissipation.

In Figure 5.17 the relative spectral dissipation of the two different test cases are plotted against the reef coverage. The relative dissipation of the corresponding empty flume test has been subtracted from all values, so that the relative dissipation at a reef for 0% coverage induces 0% dissipation. Figure 5.12 showed that the relative dissipation of the empty flume test for test case h70H5T5 equals 5.3% and for h80H10T25 equals 3.0%.

The figure shows that for both test cases, the relative dissipation almost linearly increases with growing reef coverage. This is confirmed by large large value for the coefficient of determination (R^2) resulting from the linear trend, which equals $R^2 = 0.997$ for h70H5T5 and $R^2 = 0.998$ for h8H10T25. The plot also shows that the rate of increase is largest for test case h70H5T5, from the linear trends it can be found that the rate of increase is 10% higher than for test case h80H10T25. But the values are still very closely related.

5.3.4 Summary spectral evolution and dissipation

- The presence of artificial reef structures significantly influences wave energy dissipation, as mean dissipation values for empty flume cases are lower than those for structure tests.

- In most cases, design 1 results in the smallest relative dissipation. However, the differences between the three structures (D1, D2, and C1) are minimal.
- The existence of structures leads to a shift in energy towards higher frequencies, signifying that a greater number of waves with shorter periods are transmitted in comparison to a flume without structures.
- For the test with wave conditions: $R_c = 0.25m$, $H_s = 0.09m$, $T_p = 2.5s$ the incoming wave spectra at location 3 showed that an increasing reef coverage resulted in a larger decrease of energy at the peak frequency and simultaneously an increase around the first harmonic.
- For the test with wave conditions: $R_c = 0.15m$, $H_s = 0.05m$, $T_p = 5s$ the incoming wave spectrum at location 3 showed that an increasing reef coverage resulted in a larger decrease of energy at the peak frequency and a decrease in the first harmonic.
- For both test cases, the mean energy period as measured at location 3 tends to reduce with greater reef coverage compared to the empty flume. A decrease in mean energy period indicates that the energy shifts towards higher frequencies, and thus waves with smaller periods are transmitted.
- The reef layout affects spectral dissipation in a way that the relative dissipation increases linearly with increasing reef coverage. The rate of this increase is nearly identical for both test cases.

Chapter 6 | Discussion

6.1 Physical model

Scale effects in a physical model in a wave flume refer to the differences in the behavior of the fluid and the objects being tested between the model and the real-world application. Since it is impossible to correctly model all force relationships in physical hydraulic modelling, scale effects are always present when $n \neq 1$. The relevant question is whether or not scale effects can be neglected. In general, the smaller the scale, the more the incorrectly modelled force ratios deviate from the prototype ratios and the larger the expected scale effects (Briggs, 2013). However, even if scale effects increase with n in a particular study, a given value of n does not indicate whether scale effects can be neglected or not (Heller, 2011). In a physical model, the Reynolds number is usually lower than in the real-world application because of the reduced fluid velocity and viscosity. This can result in differences in the behavior of the fluid, such as the transition from laminar to turbulent flow occurring at a different point in the model compared to the real-world application.

In this study, Froude scaling was employed to replicate real-life conditions in a wave flume using a $n_L = 4$ scale model of artificial reefs. The characteristic length of the model was 10 cm. To assess the flow regime in the scale model, the Reynolds number (Re) was calculated. In the wave flume, freshwater was used, with a typical kinematic viscosity of $\nu_{\text{freshwater}} \approx 1.0 \times 10^{-6}, \text{m}^2/\text{s}$ (ITTC, 2011). For the scale model, the Reynolds number was found to be in the range of $\text{Re}_{\text{model}} = 10{,}000 - 40{,}000$. Generally, flows with Reynolds numbers below 2,000 are considered laminar, while those with Reynolds numbers above 4,000 are considered turbulent. The calculated Reynolds numbers indicate that the flow regime in the scale model is fully turbulent flow.

This discrepancy in flow regimes between the model and real-life scenario may have an impact on the accuracy and applicability of the experimental results. In particular, the turbulent flow behavior in the real-life scenario could lead to enhanced energy dissipation and mixing, which might not be fully captured in the scale model. As a consequence, it is essential to consider the differences in flow regimes when interpreting the results and extrapolating the findings from the scale model to real-life situations. In this study, a scale of $n = 4$ was applied which is fairly large, and would mean that the scale effects are relatively small.

6.2 Wave theory approximation

In the methodology outlined in Section 4.2, both decomposition techniques employed in the present investigation assume the applicability of linear wave theory. Linear wave theory disregards non-linear terms, presuming that the wave amplitude is considerably smaller than the wavelength and the water depth ($ak << 2\pi$ and $a << d$). However, the applicability of linear wave theory is limited to cases involving non-steep waves and non-shallow water conditions (Bosboom & Stive, 2021). It is important to note that the present study's findings were derived using linear wave theory, which may introduce minor inaccuracies and inconsistencies in instances of non-linear waves; this factor should be taken into account. However, a recently conducted study by de Ridder et al. (2023) in which a nonlinear wave separation method was refined and enhanced demonstrated that the differences between linear and nonlinear-based separation techniques were relatively minor with respect to their impact on calculated wave heights.

In this study, a wave separation technique based on multiple wave gauges was employed, wherein the least squares method was utilized to extract incident waves from the measurements. It is important to note that the accuracy of this separation method may be compromised for energy in lower frequencies,

as the wavelengths associated with these frequencies are considerably longer (with a maximum of approximately 10 m) than the distances between the wave gauges (1.60m above the foreshore). This limitation could potentially influence the conclusions drawn with respect to longer wave periods. However, it should be emphasized that this technique was applied exclusively in Section 4.2, where the effectiveness of two different wave extraction methods was evaluated. Subsequently, the co-located method was adopted for extracting incoming waves, as detailed from that point forward in the thesis. This transition to the co-located method mitigates the potential impact of the aforementioned limitation on the overall study outcomes.

6.3 Data analysis

This section discusses and justifies parts of the data analysis and the corresponding results. The main aim of this section is to establish whether the results are consistent with the literature and to explain any discrepancies in order to demonstrate the validity of the results.

6.3.1 Comparison with existing empirical formulae

The literature reports numerous empirical formulae for the computation of transmission coefficient. In this study only a specific amount of wave conditions were performed, as shown in Table 3.3. Consequently, several empirical formulae could not be applied in these scenarios, since the wave parameters exceeded the limitations imposed by these functions. However, the empirical equation to compute transmission coefficient as obtained by Seabrook & Hall (1998) is applicable to the test cases of the current study as the wave parameters were within the prescribed limits of this formula. The equation reads:

$$K_T = 1 - \left(e^{-0.65\frac{R_c}{H_i} - 1.09\frac{H_i}{B}} + 0.047\frac{BR_c}{LD_{n50}} + 0.067\frac{R_c H_i}{BD_{n50}} \right) \tag{6.1}$$

Where the limits of the equation are outlined below:

$$0 \leq \frac{BR_c}{LD_{n50}} \leq 7.08 \tag{6.2}$$

$$0 \leq \frac{R_c H_s}{BD_{n50}} \leq 2.4 \tag{6.3}$$

The wave parameters used in this study, result in a minimum and maximum value of the first limit corresponding to 0.106 and 1.106 as per Equation (6.2). For the second limit as per Equation (6.3) the limits of the wave parameters used in the current study correspond to 0.073 and 0.953.

Figure 6.1 shows a scatter plot of the measured K_T values to the calculated K_T values. This plot aims at understanding the similarities between the measured and computed transmission coefficients. The figure illustrates that the transmission coefficients measured during the wave flume tests in this thesis are rather in line with the calculated transmission coefficients when using the empirical equation by Seabrook & Hall (1998). The values are scattered around the line y=x indicating that the empirical equation fairly predicts the transmission coefficients. However, the figure also shows that for the lower predicted K_T values, the deviation from the line y=x increases, for all three structure types.

The figure also includes the Root Mean Square Error (RMSE) belonging to the scatter of the three different structure types. These values indicate that there is no significant difference when comparing the structure types individually to the predicted values of the Seabrook & Hall (1998) equation.

Relative submergence and water depth: $\mathbf{R_c/H_i}$ and $\mathbf{h/H_s}$
Moreover, the impact of the relative depth ratio (h/H_s) on the transmission coefficient was analyzed and depicted in Figure 6.1b. Note that in the original empirical formula by Seabrook & Hall (1998) this

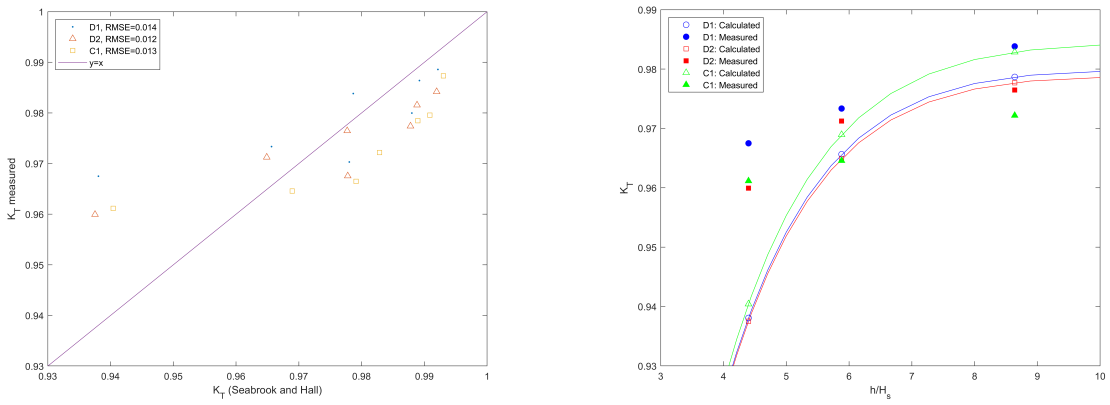

(a) *(b)*

Figure 6.1: Comparison of calculated K_T values using the empirical formula from Seabrook & Hall (1998) and measured normalised K_T (a) showing a scatter plot of the measured normalised transmission coefficient (K_T measured) and computed of the 7 non-breaking test cases. (b) The dependency of relative water depth h/Hs only including three test cases: h80H5T25, h80H75T25 and h80H10T25.

factor was included by a relative submergence ratio R_c/H_i where R_c was defined negative for submerged structures, however in this study it has been defined positive for submerged structures. This second definition has been applied to Figure 6.1b. The figure demonstrates that an augmentation in the h/H_s ratio is positively correlated with both the measured and computed transmission coefficients. Despite the general similarity in the trends of the measured and calculated transmission coefficients, noticeable discrepancies exist between the two sets of values. The divergence between the measured and computed transmission coefficients is particularly pronounced at lower relative depths. For such depths, the empirical formula put forward by Seabrook & Hall yields a markedly lower transmission coefficient compared to the measured values. Overall the results show that for increasing relative water depth, which is the same as a decreasing R_c/H_i, the transmission increases. This is in line with results from van der Meer (1990); d'Angremond et al. (1996); Seabrook & Hall (1998); Tomasicchio & D'alessandro (2013); Sindhu et al. (2015); Kurdistani et al. (2022).

Relative reef length: $\mathbf{B/H_i}$

Both d'Angremond et al. (1996) and Seabrook & Hall (1998) found that an increase in B/H_i ratio would lead to a decrease in the transmitted wave height. This trend is confirmed in the results of the current study. In Figure 5.8 this relationship is illustrated by plotting of the normalised transmission coefficient with respect to B/L instead of B/H_i. Using the second parameter would give the same trend as only the reef length (B) has been adjusted while the significant wave height (H_s) has remained constant. Additionally Kondo & Toma (1972) showed that the transmission coefficient declines as B/L increases, which is in line with the results of this study.

Wave steepness: S

Van der Meer & Daemen (1994); Tomasicchio & D'alessandro (2013); Sindhu et al. (2015) asserted that an increasing wave steepness (S) leads to a decreasing transmitted wave height. This trend is also corroborated in the present study, as depicted in Figure 5.7.

Nominal armor diameter: $\mathbf{D_{n50}}$

Furthermore Van der Meer & Daemen (1994) showed that a the nominal armor diameter of the rocks D_{n50} has an influence on the transmission coefficient via the dimensionless parameters H_i/D_{n50} and R_c/D_{n50}. As their research indicated that, for submerged structures, an increase in h_i/D_{n50} or R_c/D_{n50} results in reduced wave transmission. This statement implies that a larger D_{n50} would

lead to a higher transmission coefficient. However, this is not the case based on the results of the current study. The nominal armor diameter is largest for the cubes and smallest for design 2, but the test outcomes did not reveal a trend in which the cubes produced the highest transmission coefficient; in fact, the results were the opposite. This could imply that the different structures composing the reefs cannot be accurately represented by the nominal armor diameter D_{n50}. Figure 6.1b also shows the deviation of the three structure types as measured to the computed trend line.

Porosity: n
Porosity, denoted as n, was incorporated into the prediction method for K_T for the first time by Kurdistani et al. (2022). According to their findings, an increase in porosity leads to a decrease in transmittance. Similarly, Dick & Brebner (1968) demonstrated that for depth of submergence greater than 5%, a permeable breakwater transmits less wave energy compared to a solid one. In the current study, the depth submergence ranged between 50% and 62%. Furthermore, Huang et al. (2003) indicated that for wider porous breakwaters, an increase in porosity results in a decrease in transmitted wave height. However, the transmission and dissipation results obtained in the present study do not conform to these trends.

As evidenced by the results, the differences between the three structure types, and consequently their porosity values, are minimal, and no significant disparities were observed. On the other hand, Huang et al. (2003) also posited that if the breakwater width is small relative to the incoming wavelength, the structure's permeability does not significantly impact wave transformation. This observation could lead to the argument that the breakwaters in the current study were not sufficiently long. Nonetheless, an alternative explanation for this deviation might be that the reef types employed in this study differ substantially from submerged breakwaters, rendering them incomparable to these structures.

6.3.2 Empty flume dissipation

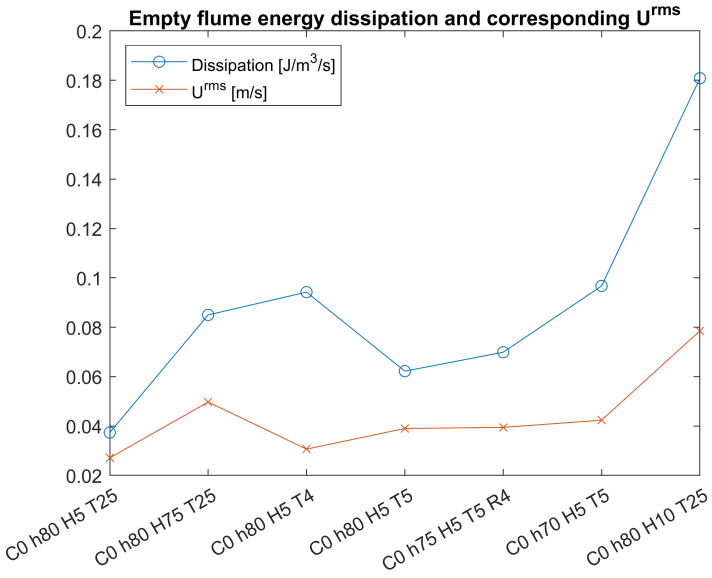

Figure 6.2: Figure indicating the distribution of the empty flume dissipation (blue) along with the measured root mean square orbital velocity in the flume (red).

As highlighted in Chapter 5, the data collected showcases the occurrence of dissipation in the empty flume. To account for variations in test conditions, the transmission coefficients were normalized. It was noted that the range of results for the empty flume was relatively narrow when compared to the outcomes of the tests conducted on the three structures. To gain a deeper understanding of the dissipation distribution in the empty flume, Figure 6.2 was generated.

The figure illustrates an increasing trend of dissipation with the rise in near-bed orbital velocity. This observation suggests that test cases with larger orbital velocities close to the bottom are more likely to be influenced by bottom roughness, resulting in the presence of dissipation in the empty flume test. However, the third test case in Figure 6.2, denoted by testID C0h80H5T4, deviates from this trend.

6.3.3 Reflection coefficient

To allow a better understanding of the transmission coefficients as researched in Section 5.2 the reflection coefficient is computed according to Equation (4.31). Figure 6.3 shows a bar chart with the computed reflection coefficients at location 2 of the seven non-breaking test cases distinguishing between the three structure types and also including the reference reflection coefficient resulting from the empty flume test.

The figure shows that the empty flume experiences a certain amount of reflection, this reflection can be attributed to the reflection from the wave absorber located at the end of the flume, but also due to the steep step down of the foreshore. This large empty flume reflection coefficient implies that the dimensions of the foreshore might not have been ideal, especially the steep bathymetry decrease down at the end of the foreshore might have had a larger influence in the reflection of waves. However, it is hard to quantify these values individually, instead a general reflection coefficient can be obtained that accounts for all the reflected waves as has been done in the figure. The empty flume reflection coefficient appears to be significantly larger for the first two tests, corresponding to testID h70H5T5 and h75H5T5, indicating that a combination of longer waves and smaller water depth are less effectively absorbed by the wave absorber.

Subsequently, the figure indicates that for 4 out of the 7 tests, the reflection coefficient is larger for tests with structures compared to the empty flume reflection coefficient. This implies that the presence of the structures induces more reflection, as one would expect. However, this is not the case for three test conditions, namely h80H10T25, h75H5T5, and h70H5T5. In these instances, the reflection coefficient is smaller in test cases with structures present than in the empty flume test cases, suggesting that the structures reduce reflection.

Furthermore, the figure demonstrates that the cube tests (yellow) consistently exhibit the highest reflection coefficients when comparing the three structures. Conversely, design 2 (blue) displays the lowest reflection coefficient in nearly all instances. Nonetheless, the reflection coefficients of design 1 and 2 are notably similar. The two complex designs possess greater porosity and rugosity than the cubes, which may suggest that reflection escalates with increasing porosity or rugosity. This observation aligns with the findings of Huang et al. (2003); Ting et al. (2004), who demonstrated that higher breakwater porosity leads to a reduction in the height of reflected waves.

Figure 6.4 shows the normalised transmission coefficients for the same tests. It could be argued that a large reflection coefficient in the cubes test may have caused the lower transmission coefficient, as larger reflection results in lower transmitted wave height and thus a smaller transmission coefficient. Additionally Design 2 consistently shows lower transmission and reflection coefficients compared to design 1. This suggests that Design 2 provides more effective dissipation compared to Design 1.

In the test case h80H10T25, it is evident that $K_{T,norm}$ is comparatively low in relation to other test results, and concurrently, $K_{R,2}$ is also small. This suggests that the reduced transmission may be attributed to increased dissipation, which is confirmed when examining Figure 5.12. However, this rationale does not apply to test case h70H5T5, where $K_{T,norm}$ is similarly lower, but $K_{R,2}$ is relatively larger. Consequently, one might argue that the low transmission value results from the high reflection coefficient, and a low dissipation value would be anticipated. Contrary to this expectation, the relative dissipation values for this test case are also significantly larger compared to the other test cases, as observed in Figure 5.12.

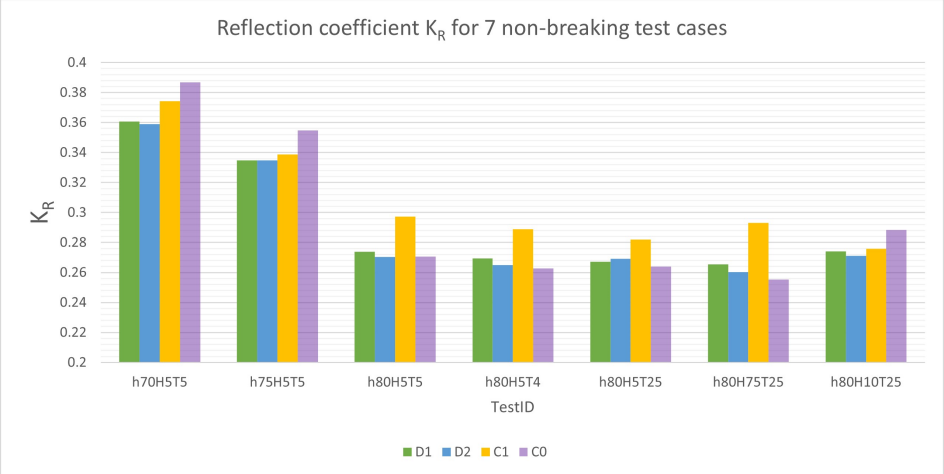

Figure 6.3: Reflection coefficient at location 2 for all seven non-breaking cases, of the three structures: Design 1 (D1), Design 2 (D2) and cubes (C1). As well as the empty flume (C0)

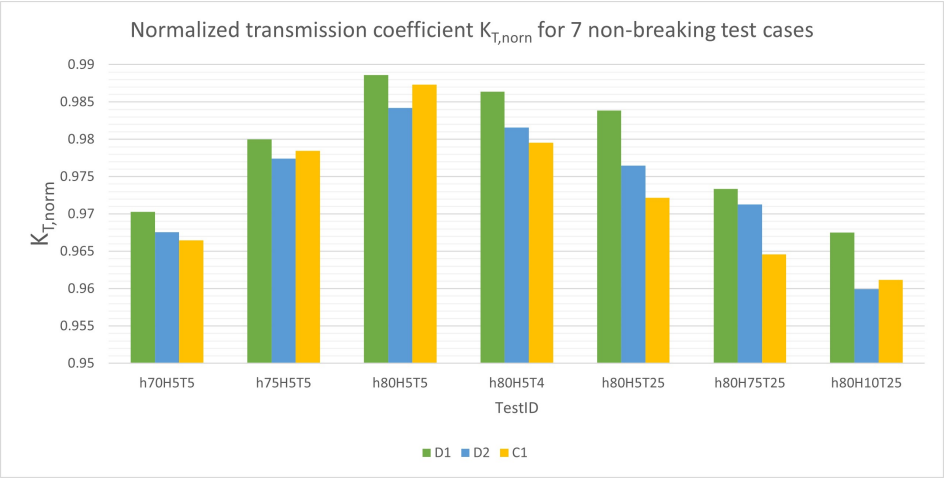

Figure 6.4: Normalised transmission coefficient for all seven non-breaking test cases, of the three structures: Design 1 (D1), Design 2 (D2) and cubes (C1).

Figure 6.5 shows a plot of the reflection coefficient at location two with respect to the relative reef length B/L. The figure shows that the reflection coefficient remains fairly constant for the reef comprised of solely design 2 structures for the range of B/L=0.05-0.22. This observation is in line with the findings of Ting et al. (2004), who stated that model width has little effect on wave reflection. However, Kondo & Toma (1972) showed that K_R does depend on B/L as it increases with increasing B/L ratio, where a maximum K_R occurs at B/L=0.2-0.25, before decreasing as the B/L ratio increases until B/L=0.6, where after it would remain constant. This first statement is not observed in the current study, however the reflection coefficient of the test with a 2m long reef comprise of design 1 and design 2 structures does show this decreasing trend as predicted by Kondo & Toma (1972).

6.3.4 Consistency wave spectra

As Table 3.3 indicates, many wave conditions have been tested several times, with only the structure changing. This section assists in finding the consistency of the wave conditions between these different test cases. This is done by measuring the variance density spectra at location 2 of the different tests with same wave conditions and comparing the difference. There are two test cases that will be analysed

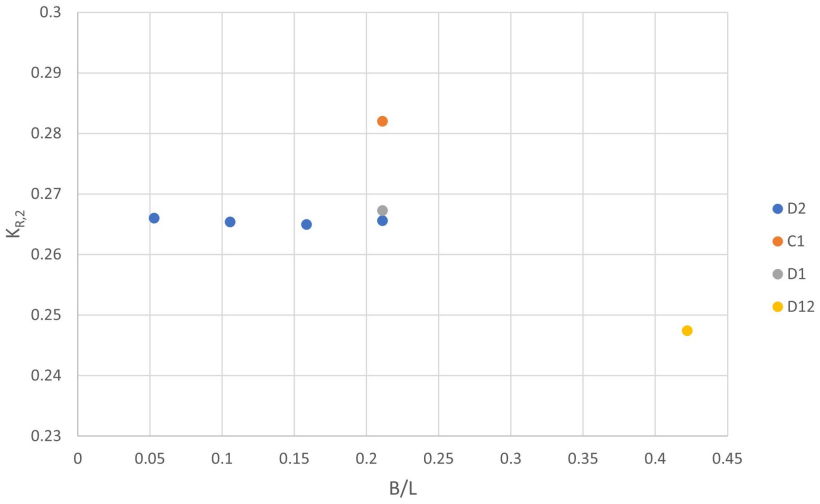

Figure 6.5: Plot of the reflection coefficient values at location 2 $K_{R,2}$ with respect to the relative reef length B/L. Corresponding to test case h80H10T25.

on consistency, namely h80H10T25 ($R_c = 0.25m$, $H_s = 0.09m$, $T_p = 2.5s$) and h70H5T5 ($R_c = 0.15m$, $H_s = 0.05m$, $T_p = 5s$). Both wave condition combinations have been applied to the following reef lay-outs: RL8-D12-A, RL8-D12-B, RL8-D12-C, RL4-D1, RL4-D2, RL4-C1, RL4-C0 (empty flume). Figure 6.6

Figure 6.6 shows the resulting variance density spectra of testID h80H10T25 for the seven different reef lay-out as mentioned above. The figure shows that the energy density spectra at location 2 are highly similar. The figure includes energy flux values, as calculated from each data set. These values range between 5.96 to 6.07 $J/m^3/s$. Similarly, Figure 6.7 shows the resulting variance density spectra of testID h70H5T5. The figure shows that the spectra are highly similar. The energy flux has been computed for each individual data set, showing again consistency in results. The energy flux values range from 2.29 to 2.33 $J/m^3/s$.

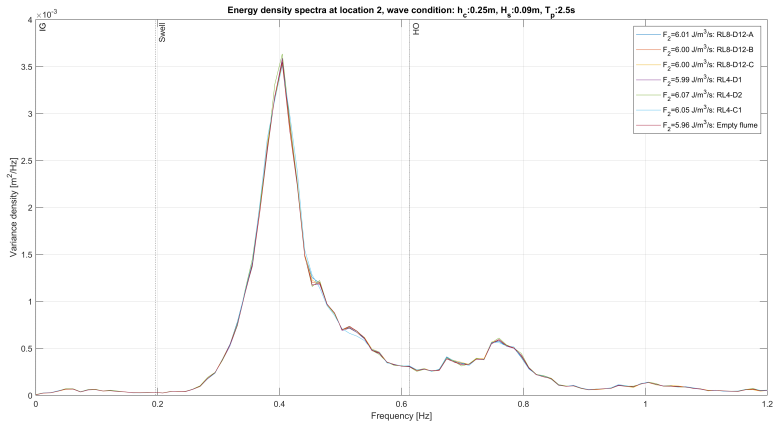

Figure 6.6: Incident energy density spectrum of 7 different reef lay-outs at location 2 corresponding to test case h80H10T25 ($R_c = 0.25m$, $H_s = 0.09m$, $T_p = 2.5s$). Including Energy flux ($F_2 = C_g E$)

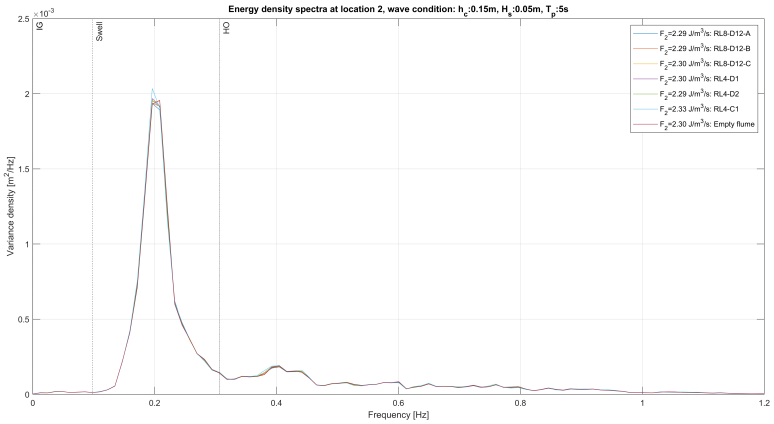

Figure 6.7: Incident energy density spectrum of 7 different reef lay-outs at location 2 corresponding to test case h70H5T5 ($R_c = 0.15m$, $H_s = 0.05m$, $T_p = 5s$). Including Energy flux ($F_2 = C_g E$)

6.3.5 Evolution of characteristic wave periods and wave run-up

As demonstrated by Van Gent (1999), wave run-up exhibits a higher value for waves with longer periods compared to those with shorter periods. In this study, wave run-up refers to the vertical extent of wave uprush on a shoreline or structure above the still water level, representing the maximum elevation attained by a wave on a beach, seawall, or other coastal structure. The findings presented in Section 5.3.2 reveal that the mean energy period $T_{m-1,0}$ at location 3 is consistently smaller for all tests incorporating artificial reefs compared to those the mean energy period in the empty flume tests. This reduction in the mean energy period indicates an energy shift towards higher frequencies, implying that waves with larger periods are filtered, and only waves with shorter periods transmit over the structure. Consequently, it can be inferred that the artificial reefs influence wave run-up at locations shoreward of the reefs, leading to a decrease in run-up values.

Chapter 7 | Conclusions and Recommendations

7.1 Conclusions

In this section the conclusion to the main research question will be given. This is done by first answering the sub-questions as stated in Chapter 1.

1. What is the added value of structural complexity in natural coral reefs, and how is it quantified?

According to the literature, structural complexity is expected to be positively associated with species richness, coral recovery, live coral cover and coastal protection. Due to the large variation in shelters, cavities and branching of coral reefs, many different sizes of shelters and niches allow different species to coexist. This wide variation is a result of the geometric complexity. In addition, coral growth is expected to be enhanced due to the structural complexity of reefs. This is because the greater number of cavities allows broken pieces of coral to remain trapped in these spaces rather than floating away. In addition, geometric complexity has been shown to be positively correlated with reef resilience. Finally, natural coral reefs are a natural form of coastal protection, as they can have a positive effect on the transmission and dissipation of wave energy. Studies have shown that this is a result of the roughness of coral reefs, which is an effect of the structural complexity of reefs.

There is no single definition of structural complexity as it can be encompassed with many features. Depending on the objective of the research, structural complexity in reefs is often quantified using multiple parameters. This allows different features to be combined. Among many parameters, porosity, rugosity and fractal dimension are the most commonly used to measure the structural complexity of coral reefs.

- **Porosity** is defined by the ratio of cavities volume to the occupied volume, or also called the volume of the bounding box
- **Rugosity** can be measured using the 'Chain-tape method', which is widely used on natural coral, as it is an in-situ and low cost method. To obtain the rugosity index with this method, a chain of known length is laid along the contours of the seabed. The ratio of its draped length to its undraped length gives a rugosity value.
- **Fractal dimension** is a measure that defines the way of branching of a structure or translates the way an object fills the space.

2. On which hydrodynamic processes does the structural complexity of coral have an influence, and how can tests in a wave tank be best designed to investigate this?

The bathymetry change of natural coral reefs can often be divided into three regions: (1) a steep sloping fore reef, follows by a (2) reef flat, where the water depth is low and the bottom slope is minimal, and finally (3) a deeper lagoon. This third region is only present in Barrier reefs and Atoll type reefs, but not in fringing reef types.When an onshore propagating wave length is roughly equal to the water depth, it starts to interact with the changing bathymetry of the forereef. The wave initially begins to steepen due to a process known as shoaling, until eventually at a specific critical water depth, the wave breaks. Wave breaking is thus an effect of decreasing water depth.

After the largest waves have broken, only waves with height ratios that are smaller than the breaker limit will continue to propagate towards the coast over the reef flat. The relatively small waves that

are free to pass the reef crest and propagate over the reef flat will also dissipate, only not due to wave breaking but due to bottom friction caused by the hydraulic rough reef. Studies have proven that the large structural complexity of coral reefs results in high hydraulic roughness and subsequently greater frictional dissipation of waves.

In this study, wave flume tests were conducted using various artificial reef types. These artificial reefs were composed exclusively of three distinct structures with differing structural complexity. Since structural complexity primarily affects wave dissipation through bottom friction, the tests were designed to prevent incoming waves from breaking on top of the artificial reefs. This approach ensured that dissipation could be attributed to friction rather than wave breaking. Consequently, the irregular wave conditions implemented in the physical model tests of this study were as follows:

- Crest submergence R_c: [0.15; 0.20; 0.25] m
- Significant wave height H_s: [0.05; 0.07; 0.09] m
- Peak period T_p: [2.5;4.1;4.9;5.2] s
- Wave steepness S: 0.005-0.019

3. In what way is the wave transmission influenced by different wave parameters and do the different structures show a different behaviour?

In the current study three reef types with the same dimensions have been tested on the transmission coefficient. These reefs were made of of three distinct structures. The three structures used in this thesis were two geometrically complex structures, named design 1 and 2, with porosity and rugosity values according to Table 7.1. The third structure acted as a non-complex reef consisting of cubes with zero porosity and zero rugosity.

Design	Porosity	Rugosity
1	67	2.02
2	73	2.18

Table 7.1: Structural complexity parameters of the two designs

The tests conducted in the present study demonstrated that an increase in relative water depth leads to an increase in the transmission coefficient. The relative water depth is defined as the ratio of the water depth in front of the reef (h) to the significant wave height (H_s), expressed as h/H_s. This implies that an increase in water depth and/or a decrease in significant wave height results in a larger transmitted wave height.

Similarly, the results revealed that, for the tested conditions, wave steepness has a negative impact on the transmission coefficient, as it was observed that waves with a larger wave steepness yielded lower transmitted wave heights, indicating that the transmission coefficient is smaller for steeper incoming waves. Wave steepness is defined as the ratio of the incoming significant wave height (H_s) to the local wave length (L), denoted as H_s/L. This suggests that an increase in incoming wave height and/or a decrease in wave length leads to lower transmitted wave heights.

Upon comparing the results of the three structures individually, the absolute values of the transmission coefficient did not reveal a significant difference between the distinct structures for the tested conditions. The findings suggested that the transmission coefficient for this specific reef configuration, extending merely one meter, is of the same order of magnitude for all three structures, with an order of magnitude

of K_T=$O(10^{-3})$. While the results demonstrated that design 1 consistently exhibited the largest transmission coefficient among the three structure types, the difference was quite minimal.

4. In what way is the wave transmission influenced by different reef set-ups?

In this study, reef coverage is measured as a ratio of the number of structures present in the reef area to the maximum number of structures that can fit in the area, defined as $N_{structures}/N_{max}$. The reef coverage was altered according to [0; 31.3, 62.5; 100] %, where the maximum reef coverage is defined as 100%. This corresponds to a reef composed of the maximum number of structures possible for that stretch, which in this study equaled 2m. The results demonstrated that as the reef coverage increased, the transmission coefficient decreased, following an almost linear trend. This trend was consistent across two different wave conditions, as this test set-up was conducted for two distinct wave conditions:

1. S=0.006, h/H_s=6.2
2. S=0.019, h/H_s=4.4

The findings indicated that the test corresponding to the higher wave steepness ($S = H_s/L$) and lower relative water depth (h/H_s) exhibited lower values of the transmission coefficient. Consequently, the significant wave height of incoming waves with larger steepness and smaller relative water depth are more effectively reduced.

Secondly, the effect of the relative reef length was examined for a reef consisting solely of design 2 structures with constant incoming wave parameters of R_c = 0.25m, H_s = 0.1m, and T_p = 2.5s. The relative reef length is the ratio of the reef crest width (B) to the wavelength (L), defined as B/L. The reef length was systematically increased by adding a row of solely design 2 structures per test, varying from 1 to 4 rows. The test results demonstrated that the transmission coefficient decreases linearly as the relative reef length increases, ranging from K_T=0.985 for B/L=0.05 to K_T=0.963 for B/L=0.21. However, a reef composed of design 1 and design 2 structures with a relative length of B/L=0.42, consisting of 8 rows, did not follow the same linear trend. The transmission coefficient for this test was K_T=0.957, and thus followed a smaller rate of decrease.

5. How does the presence of different artificial reef structures affect the spectral evolution and dissipation?

The presence of different artificial reef structures has a significant influence on the spectral dissipation values in non-breaking test cases. The mean dissipation values for the empty flume cases are significantly lower than those for the structure tests. The presence of structures leads to an increase in mean relative dissipation values. When comparing the three structures (D1, D2, and C1), there is no significant difference in relative dissipation values. In almost all cases, design 1 resulted in the smallest relative dissipation, although the difference is minimal. Overall, the presence of structures affects the dissipation, with different structures showing minimal variations in their impact on the spectral dissipation values.

The results revealed that the mean energy period $T_{m-1,0}$ behind the reef was consistently lower for tests involving an artificial reef compared to the corresponding reference test, where the flume was empty. A reduction in mean energy period suggests a shift in energy towards higher frequencies, indicating the transmission of smaller waves. The mean of the $T_{m-1,0}$ values corresponding to the test cases was highest for Design 2 results and lowest for the cubes results, implying that the reef composed of cubes transmits smaller waves than the reef consisting of Design 2 structures. However, it should be noted that the absolute differences are minimal.

6. How do various reef configurations influence the spectral evolution and dissipation under different wave conditions?

he findings of this section of the thesis demonstrate that reef coverage influences the spectral evolution. Two distinct sets of wave conditions were employed for this part of the tests. The wave conditions with $R_c = 0.25$m, $H_s = 0.1$m, and $T_p = 2.5$s indicated that, at location 3, increasing reef coverage led to a greater reduction in energy at the peak frequency and a simultaneous increase around the first harmonic. However, the energy increment in the first harmonic is considerably smaller than the reduction at the peak. For the test with wave conditions $R_c = 0.15$m, $H_s = 0.05$m, and $T_p = 5$s, the incoming wave spectrum at location 3 revealed that increasing reef coverage resulted in a larger decrease in energy at the peak frequency and a reduction in the first harmonic.

Overall, reef coverage plays a crucial role in determining the spectral evolution under different wave conditions, as $T_{m-1,0}$ reduces with greater reef coverage compared to the empty flume. A decrease in mean energy period indicates that the energy shifts towards higher frequencies, and thus waves with smaller periods are transmitted.

Additionally, The reef coverage affects the relative spectral dissipation values in a way that the relative dissipation increases linearly with increasing reef coverage. The rate of this increase is nearly identical for both test cases.

What is the relationship between structural complexity of elements in artificial reefs and their effectiveness in dissipating and attenuating wave energy?

In this thesis, physical model tests were conducted exclusively under non-breaking wave conditions, examining various reef types characterized by different structural complexity values. The results of these tests reveal that structural complexity does not have a significant impact on wave transmission. The three reefs, each with distinct structural complexity values and a length of 1m, exhibited high transmission, with coefficients ranging between 0.96 and 0.99 across various non-breaking wave conditions. Design 1 had the highest mean transmission coefficient, with $K_{T,norm}$=0.98, while Design 2 and the cubes had equal mean coefficients of $K_{T,norm}$=0.97.

Furthermore, the findings of this study indicate no significant differences in dissipation results when comparing the three structure types with varying complexity values. Overall, the dissipation ranged from 5.5% to 13.5% of the incoming wave energy for the three structures. The mean spectral energy dissipation was lowest for Design 1, at 8.1%, and higher for Design 2 and the cubes, both equal to 9.0%. Reef coverage was found to have a positive impact on transmission reduction and spectral wave dissipation. With increasing reef coverage, a linear decrease in transmission coefficient was observed, accompanied by a simultaneous increase in dissipation.

In conclusion, although the wave attenuation effects are similar and the differences between the designs are minimal, the environmental advantages offered by a highly structurally complex reef indicate that it should be viewed as a viable solution.

7.2 Recommendations

- **Overtopping**
  During the experimental phase of the project conducted at Deltares, additional two weeks of tests were carried out to investigate the impact of the artificial reef on the overtopping. These tests yielded a substantial amount of data, which, unfortunately, could not be analyzed within the scope of this thesis. Nonetheless, examining this data would provide valuable insights into the practical effectiveness of the artificial reef in reducing overtopping. Therefore, future research

could focus on analyzing this data to gain a more comprehensive understanding of the impact of the artificial reef on reducing overtopping. Such an analysis could contribute to the optimization of artificial reef designs.

- **Numerical modelling**
  In the course of this study, a considerable amount of data has been gathered and analyzed. These data can serve as a valuable input for numerical modelling, as they can be used as control measurements to adjust the model to. By obtaining an accurate numerical model, it would be possible to gather data much more quickly than through physical model tests, and at a lower cost. This would make it possible to explore a wider range of scenarios and to test the effectiveness of different reef designs under varying wave conditions. The availability of reliable numerical models could also facilitate the development of more efficient and effective reef designs, leading to more sustainable coastal protection strategies in the future. Therefore, it is recommended that the data collected in this study be made available to researchers and engineers involved in numerical modelling of artificial reef systems.

- **Including structural complexity in empirical formula**
  As discussed in this thesis, numerous empirical equations exist to predict the transmission coefficient for any type of submerged breakwater. Nevertheless, these equations do not account for structural complexity, as highlighted in this thesis. Physical model tests could be conducted to determine an empirical formula that accounts for structural complexity, such as porosity and rugosity. In this context, Coastruction, the company involved in this research, possesses a 3D printer, which could be advantageous in producing multiple differently shaped structures and evaluating them on a certain structural complexity scale. This could aid in including this parameter into existing empirical formulas, enhancing their accuracy and applicability.

- **Stability**
  In order to deploy the investigated structures as submerged breakwaters or to fill empty spaces in live coral to enhance biodiversity, it is crucial to obtain information about their stability. The present study primarily focused on non-breaking test cases. However, if these structures are to be deployed in locations where the primary objective is wave attenuation, it is essential to subject them to wave conditions that generate large forces on the structures. It is important to note that such wave conditions were not simulated in this study. Therefore, further investigation is necessary to obtain a more comprehensive understanding of the stability of these structures under more extreme wave conditions.

References

Allen, G. R. (2008). Conservation hotspots of biodiversity and endemism for indo-pacific coral reef fishes.

Andersen, T. L., Clavero, M., Frigaard, P., Losada, M., & Puyol, J. (2016). A new active absorption system and its performance to linear and non-linear waves. *Coastal Engineering*, *114*, 47–60.

Andersen, T. L., & Eldrup, M. R. (2021). Estimation of incident and reflected components in nonlinear regular waves over sloping foreshores. *Coastal Engineering*, *169*, 103974.

Armono, H. D. (2004). Wave transmission over hemispherical shape artificial reefs. In *Marine technology conference.*

Baine, M. (2001). Artificial reefs: a review of their design, application, management and performance. *Ocean & Coastal Management*, *44*(3-4), 241–259.

Beetham, E. P., & Kench, P. S. (2014). Wave energy gradients and shoreline change on vabbinfaru platform, maldives. *Geomorphology*, *209*, 98–110.

Bellwood, D. R., Hughes, T. P., Folke, C., & Nyström, M. (2004). Confronting the coral reef crisis. *Nature*, *429*(6994), 827–833.

Bleck, M. (2006). Wave attenuation by artificial reefs. *PIANC magazine" on course" nr 125*.

Bosboom, J., & Stive, M. J. (2021). *Coastal dynamics.* TU Delft Open.

Bozec, Y.-M., Alvarez-Filip, L., & Mumby, P. J. (2015). The dynamics of architectural complexity on coral reefs under climate change. *Global change biology*, *21*(1), 223–235.

Brancasi, A., Leone, E., Francone, A., Scaravaglione, G., & Tomasicchio, G. R. (2022). On formulae for wave transmission at submerged and low-crested breakwaters. *Journal of Marine Science and Engineering*, *10*(12), 1986.

Briggs, M. (2013, 09). Basics of physical modeling in coastal and hydraulic engineering. *US Army Engineer Research and Development Center, Coastal & Hydraulics Laboratory*, *XIII*, 11.

Buckley, M. L., Lowe, R. J., Hansen, J. E., & Van Dongeren, A. R. (2015). Dynamics of wave setup over a steeply sloping fringing reef. *Journal of Physical Oceanography*, *45*(12), 3005–3023.

Carlot, J., Vousdoukas, M., Rovere, A., Karambas, T., Lenihan, H. S., Kayal, M., ... Parravicini, V. (2023). Coral reef structural complexity loss exposes coastlines to waves. *Scientific Reports*, *13*(1), 1683.

Cesar, H., Burke, L., & Pet-Soede, L. (2003). *The economics of worldwide coral reef degradation.* International Coral Reef Action Network.

Coker, D. J., Wilson, S. K., & Pratchett, M. S. (2014). Importance of live coral habitat for reef fishes. *Reviews in Fish Biology and Fisheries*, *24*, 89–126.

Costa, M. B., Araújo, M., Araújo, T. C., & Siegle, E. (2016). Influence of reef geometry on wave attenuation on a brazilian coral reef. *Geomorphology*, *253*, 318–327.

d'Angremond, K., Van Der Meer, J. W., & De Jong, R. J. (1996). Wave transmission at low-crested structures. In *Coastal engineering 1996* (pp. 2418–2427).

de Ridder, M. P., Kramer, J., den Bieman, J. P., & Wenneker, I. (2023). Validation and practical application of nonlinear wave decomposition methods for irregular waves. *Coastal Engineering*, *183*, 104311. Retrieved from https://www.sciencedirect.com/science/article/pii/S0378383923000352 doi: https://doi.org/10.1016/j.coastaleng.2023.104311

Deltares. (2012a). Instrument, Wave height meter, version 1.1.

Deltares. (2012b). Programmable electromagnetic liquid velocity meter, version 1.1.

Deltares. (2012c). Instrument, Wave height and direction meter, version 1.1.

Deltares. (2015, Feb). *Scheldt flume.* Retrieved from https://www.deltares.nl/en/facilities/scheldt-flume/

Dick, T. M., & Brebner, A. (1968). Solid and permeable submerged breakwaters. In *Coastal engineering 1968* (pp. 1141–1158).

East, H. K., Perry, C. T., Beetham, E. P., Kench, P. S., & Liang, Y. (2020). Modelling reef hydrodynamics and sediment mobility under sea level rise in atoll reef island systems. *Global and Planetary Change*, *192*, 103196.

Ferrario, F., Beck, M. W., Storlazzi, C. D., Micheli, F., Shepard, C. C., & Airoldi, L. (2014). The effectiveness of coral reefs for coastal hazard risk reduction and adaptation. *Nature communications*, *5*(1), 1–9.

Galvin, C. J. (1972). Wave breaking in shallow water. *Waves on beaches and resulting sediment transport*, 413–456.

Goda, Y., & Ahrens, J. P. (2009). New formulation of wave transmission over and through low-crested structures. In *Coastal engineering 2008: (in 5 volumes)* (pp. 3530–3541). World Scientific.

Graham, N. A. J., & Nash, K. L. (2013). The importance of structural complexity in coral reef ecosystems. *Coral reefs*, *32*(2), 315–326.

Guo, J. (2002). Simple and explicit solution of wave dispersion equation. *Coastal Engineering*, *45*(2), 71–74.

Guza, R., Thornton, E., & Holman, R. (1984). Swash on steep and shallow beaches. In *Coastal engineering 1984* (pp. 708–723).

Harangozo, S. (1992). Flooding in the maldives and its implications for the global sea level rise debate. *Geophysical Monograph Series*, *69*, 95–99.

Harris, D. L., Rovere, A., Casella, E., Power, H., Canavesio, R., Collin, A., ... Parravicini, V. (2018). Coral reef structural complexity provides important coastal protection from waves under rising sea levels. *Science advances*, *4*(2), eaao4350.

Hata, T., Madin, J. S., Cumbo, V. R., Denny, M., Figueiredo, J., Harii, S., ... Baird, A. H. (2017). Coral larvae are poor swimmers and require fine-scale reef structure to settle. *Scientific reports*, *7*(1), 1–9.

Heller, V. (2011). Scale effects in physical hydraulic engineering models. *Journal of Hydraulic Research*, *49*(3), 293–306.

Holthuijsen, L. H. (2010). *Waves in oceanic and coastal waters.* Cambridge university press.

House, J. E., Brambilla, V., Bidaut, L. M., Christie, A. P., Pizarro, O., Madin, J. S., & Dornelas, M. (2018). Moving to 3d: relationships between coral planar area, surface area and volume. *PeerJ*, *6*, e4280.

Huang, C.-J., Chang, H.-H., & Hwung, H.-H. (2003). Structural permeability effects on the interaction of a solitary wave and a submerged breakwater. *Coastal engineering*, *49*(1-2), 1–24.

ITTC. (2011). International towing tank conference - recommended procedures: Fresh water and seawater properties.

Jonsson, I. G. (1967). Wave boundary layers and friction factors. In *Coastal engineering 1966* (pp. 127–148).

Kench, P. S., Brander, R. W., Parnell, K. E., & McLean, R. F. (2006). Wave energy gradients across a maldivian atoll: Implications for island geomorphology. *Geomorphology*, *81*(1-2), 1–17.

Kench, P. S., Brander, R. W., Parnell, K. E., & O'Callaghan, J. (2009). Seasonal variations in wave characteristics around a coral reef island, south maalhosmadulu atoll, maldives. *Marine Geology*, *262*(1-4), 116–129.

Knudby, A., & LeDrew, E. (2007). Measuring structural complexity on coral reefs. In *Proceedings of the american acadamy of underwater sciences 26th symposium* (pp. 181–188).

Kondo, H., & Toma, S. (1972). Reflection and transmission for a porous structure. In *Coastal engineering 1972* (pp. 1847–1866).

Kurdistani, S. M., Tomasicchio, G. R., Felice, D., & Francone, A. (2022). Formula for wave transmission at submerged homogeneous porous breakwaters. *Ocean Engineering*, *266*, 113053.

Leujak, W., & Ormond, R. (2007). Comparative accuracy and efficiency of six coral community survey methods. *Journal of experimental marine biology and ecology*, *351*(1-2), 168–187.

Lin, C.-Y., & Huang, C.-J. (2004). Decomposition of incident and reflected higher harmonic waves using four wave gauges. *Coastal engineering*, *51*(5-6), 395–406.

Lowe, R. J., Falter, J. L., Bandet, M. D., Pawlak, G., Atkinson, M. J., Monismith, S. G., & Koseff, J. R. (2005). Spectral wave dissipation over a barrier reef. *Journal of Geophysical Research: Oceans*, *110*(C4).

Lowe, R. J., Falter, J. L., Koseff, J. R., Monismith, S. G., & Atkinson, M. J. (2007). Spectral wave flow attenuation within submerged canopies: Implications for wave energy dissipation. *Journal of Geophysical Research: Oceans*, *112*(C5).

Madsen, O. S. (1994). Spectral wave-current bottom boundary layer flows. In *Coastal engineering 1994* (pp. 384–398).

Mansard, E. P., & Funke, E. (1980). The measurement of incident and reflected spectra using a least squares method. In *Coastal engineering 1980* (pp. 154–172).

Monismith, S. G., Rogers, J. S., Koweek, D., & Dunbar, R. B. (2015). Frictional wave dissipation on a remarkably rough reef. *Geophysical Research Letters*, *42*(10), 4063–4071.

Mörner, N.-A., Tooley, M., & Possnert, G. (2004). New perspectives for the future of the maldives. *Global and planetary change*, *40*(1-2), 177–182.

Nelson, R. (1996). Hydraulic roughness of coral reef platforms. *Applied Ocean Research*, *18*(5), 265–274.

Nielsen, P. (1992). *Coastal bottom boundary layers and sediment transport* (Vol. 4). World scientific.

Nunes, V., & Pawlak, G. (2008). Observations of bed roughness of a coral reef. *Journal of Coastal Research*(24 (10024)), 39–50.

Osinga, R., Schutter, M., Griffioen, B., Wijffels, R. H., Verreth, J. A., Shafir, S., ... Lavorano, S. (2011). The biology and economics of coral growth. *Marine biotechnology*, *13*, 658–671.

Pomeroy, A. W., Ghisalberti, M., Peterson, M., & Farooji, V. E. (2023). A framework to quantify flow through coral reefs of varying coral cover and morphology. *PloS one*, *18*(1), e0279623.

Pörtner, H.-O., Roberts, D. C., Adams, H., Adler, C., Aldunce, P., Ali, E., ... others (2022). Climate change 2022: Impacts, adaptation and vulnerability. *IPCC Sixth Assessment Report*.

Reichert, J., Backes, A. R., Schubert, P., & Wilke, T. (2017). The power of 3d fractal dimensions for comparative shape and structural complexity analyses of irregularly shaped organisms. *Methods in Ecology and Evolution*, *8*(12), 1650–1658.

Ribas-Deulofeu, L., Château, P.-A., Denis, V., & Chen, C. A. (2021). Portraying gradients of structural complexity in coral reefs using fine-scale depth profiles. *Frontiers in Marine Science*, NA–NA.

Riera, E. (2020). *Towards a purposeful construction of a new generation of artificial reefs: Comparative analyses of the intrinsic factors favouring their colonization from micro to macro-scale* (Unpublished doctoral dissertation). Université Côte d'Azur.

Safari, M. D. (2018). A short review of submerged breakwaters. In *Matec web of conferences* (Vol. 203, p. 01005).

Seabrook, S., & Hall, K. (1998). Design equation for transmission at submerged rubblemound breakwaters. *Journal of Coastal Research*, 102–106.

Sherman, R. L., Gilliam, D. S., & Spieler, R. E. (2002). Artificial reef design: void space, complexity, and attractants. *ICES Journal of Marine Science*, *59*(suppl), S196–S200.

Sindhu, S., Shirlal, K. G., et al. (2015). Prediction of wave transmission characteristics at submerged reef breakwater. *Procedia Engineering*, *116*, 262–268.

Sorokin, Y. I. (2013). *Coral reef ecology* (Vol. 102). Springer Science & Business Media.

Ting, C.-L., Lin, M.-C., & Cheng, C.-Y. (2004). Porosity effects on non-breaking surface waves over permeable submerged breakwaters. *Coastal engineering*, *50*(4), 213–224.

Tomasicchio, G. R., & D'alessandro, F. (2013). Wave energy transmission through and over low crested breakwaters. *Journal of Coastal Research*(65 (10065)), 398–403.

UNEP. (2009). *London convention and protocol unep: Guidelines for the placement of artificial reefs.* United Nations Environment Programme (UNEP) London.

van der Meer, J. W. (1990). *Data on wave transmission due to overtopping.* Delft Hydraulics.

Van der Meer, J. W., & Daemen, I. F. (1994). Stability and wave transmission at low-crested rubble-mound structures. *Journal of waterway, port, coastal, and ocean engineering*, *120*(1), 1–19.

Van Gent, M. (1999). Wave run-up and wave overtopping for double peaked wave energy spectra. *H3351*.

Walbridge, S., Slocum, N., Pobuda, M., & Wright, D. J. (2018). Unified geomorphological analysis workflows with benthic terrain modeler. *Geosciences*, *8*(3), 94.

Yanovski, R., Nelson, P. A., & Abelson, A. (2017). Structural complexity in coral reefs: examination of a novel evaluation tool on different spatial scales. *Frontiers in Ecology and Evolution*, *5*, 27.

Yao, Y., Yang, X., Liu, W., & He, T. (2021). The effect of reef roughness on monochromatic wave breaking and transmission over fringing reefs. *Marine Georesources & Geotechnology*, *39*(3), 354–364.

Young, G., Dey, S., Rogers, A., & Exton, D. (2017). Cost and time-effective method for multi-scale measures of rugosity, fractal dimension, and vector dispersion from coral reef 3d models. *PloS one*, *12*(4), e0175341.

Young, I. (1999). Seasonal variability of the global ocean wind and wave climate. *International Journal of Climatology: A Journal of the Royal Meteorological Society*, *19*(9), 931–950.

Zawada, K. J., Dornelas, M., & Madin, J. S. (2019). Quantifying coral morphology. *Coral Reefs*, *38*(6), 1281–1292.

Zelt, J., & Skjelbreia, J. E. (1992). Estimating incident and reflected wave fields using an arbitrary number of wave gauges. In *Coastal engineering 1992* (pp. 777–789).

Appendix A | Foreshore assessment

Using a one-dimensional SWASH model, numerical models using a number of possible combinations of foreshore height and water depth have been created and run through the software. A visualisation of the impact of the height of the foreshore on the Ursell number can be found in Figure A.1. These figures show with a constant water depth, an increase in possible peak periods with an increase of the foreshore height.

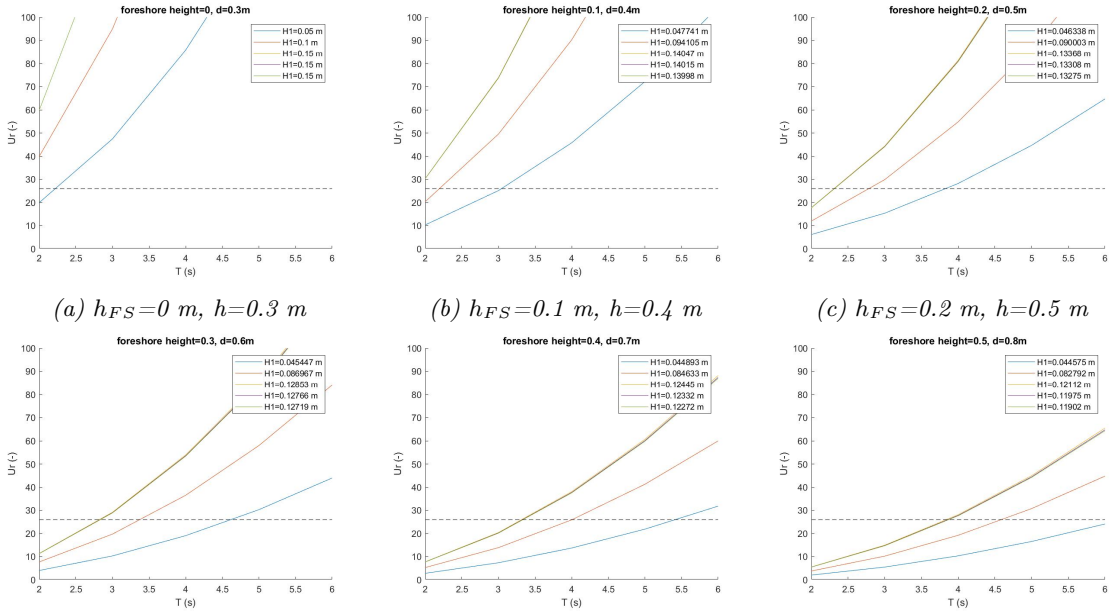

(a) h_{FS}=0 m, h=0.3 m *(b) h_{FS}=0.1 m, h=0.4 m* *(c) h_{FS}=0.2 m, h=0.5 m*

(d) h_{FS}=0.3 m, h=0.6 m *(e) h_{FS}=0.4 m, h=0.7 m* *(f) h_{FS}=0.5 m, h=0.8 m*

Figure A.1: Plots of Ursell values to peak period (Tp), displaying the possible Tp values for different foreshore height (h_{FS}) and water depth (h) combinations. The water depth above the foreshore is equal to 0.3 m in all situations.

Additionally, measured reef flat depths from the Maldives have been included in this assessment. From the field studies performed by Kench et al. (2006, 2009); Beetham & Kench (2014); East et al. (2020), which have been extensively discussed in Section 2.1.1, it can be concluded that the reef flat depth at the Maldives is maximum 1.5 m. Taking the above into account, the decision had been made to include a foreshore with a height of **40 cm** in the flume.

Next to the height, the slope of the foreshore has a large impact on the wave transformation. A SWASH 1D model of the wave flume including the foreshore has been generated. In this numerical model, various wave conditions have been simulated, using two different slopes. Namely a 1:1 (45 deg) and a 1:10 (6 deg) slope. These SWASH simulations are performed to have a feeling of the influence of the different slopes on the wave breaking and shoaling on the foreshore.

Figure A.2 shows the significant wave height of a few wave conditions over the wave flume. This plot shows that the wave conditions at the flume with a foreshore slope of 1:1 will be largely reflected by the steep slope, while the 1:10 slope plots show much less reflection. Additionally, the plot shows that the remaining Hs at the foreshore flat is just a little lower for the 1:1 slope than for the 1:10 slope. This holds only for the breaking wave condition and does not hold for the non-breaking wave condition,

here the remaining H_s at the flat are equal. Lastly the plot shows that the wave height remains stable at about 25m for the breaking wave condition on the 1:1 slope and at 28m on the 1:10 slope.

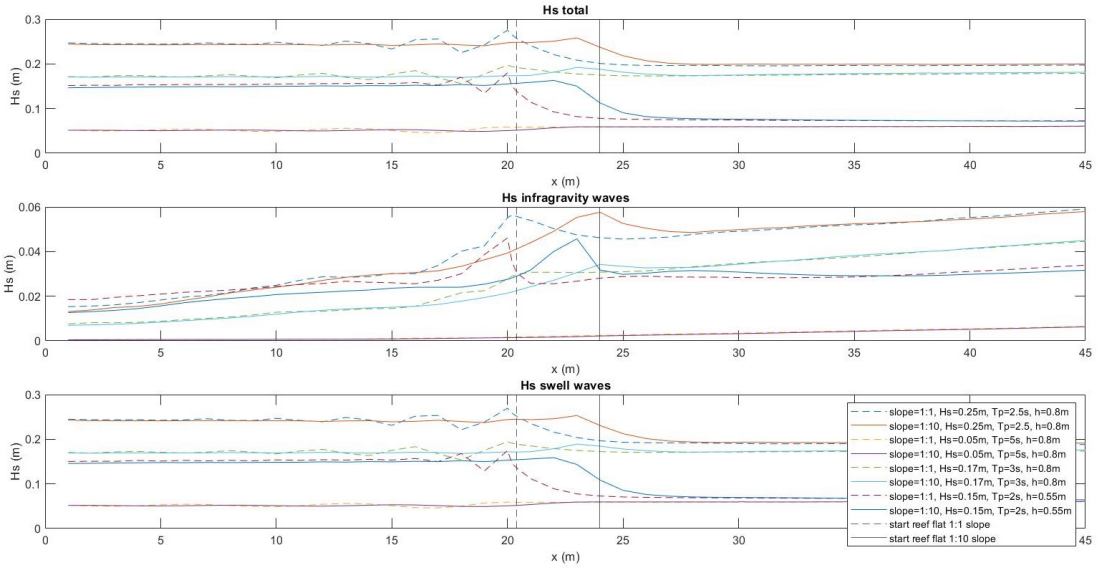

Figure A.2: Plot of significant wave height (H_s) for different wave conditions with a foreshore slope of 1:1 and 1:10.

Appendix B | Printing process

Coastruction has developed a 3D concrete printer that utilizes powder-bed technology to print concrete elements. Unlike extrusion technology, powder-bed technology enables printing of overhanging parts, resulting in fewer design limitations. The printer can print an area up to 250 mm x 250 mm x 150 mm with a printing resolution of 2.5mm. The printing technology allows printing with only a dry material and water. This dry material can be any powder that reacts and hardens with a liquid. Coastruction often prints using cement, sand and water. They have done tests with a large variety of aggregates, such as dolomite sand, aragonite sand, quartz sand, beach sand and recycled concrete. For the binder, Coastruction uses cement, CEM III to be precise. This kind of cement is commonly known as marine cement and provides a lower carbon footprint than the common used Portland cement.

The 3D printing process can be divided into four distinct phases, with each phase having its specific considerations. These phases are divided into (1) designing, (2) printing, (3) cleaning and (4) curing. The phases are illustrated below, along with the most significant aspects associated with each phase.

1. In order to produce the desired object using 3D printing, a design must first be created. This design can be generated through a variety of means, such as the creation of a 3D model using computer-aided design (CAD) software or the creation of a physical model using materials like clay that can be scanned into a 3D modeling program. The 3d model is then processed by a slicer, which divides the model in layers, and generates machine instructions for each one of them.

2. When the 3D model is ready and checked for errors, it can be send to the printer software. Prior to printing, the material needs to be prepared. The dry material often is a mixture of sand and cement with a specific ratio. Then the printing process can start, this is done by laying a first layer of dry material, each layer is exactly 2.5 mm thick. After the layer of dry material is deposited on top of the 25x25 cm area, the nozzle starts depositing water drops at the specific locations according to the 3D model. Figure B.2 show what this looks like in reality. When all water has been precisely deposited according to the layer, the bottom of the printed material lowers exactly 2.5 mm, which coincides with the layer thickness. This creates an empty layer at the top of the material, which is filed with new dry material by the printer. This process is then repeated layer by layer until the desired print is ready, the maximum height of the structure is thus 15 cm. See Figure B.1 for a visualisation of this layer repetition.

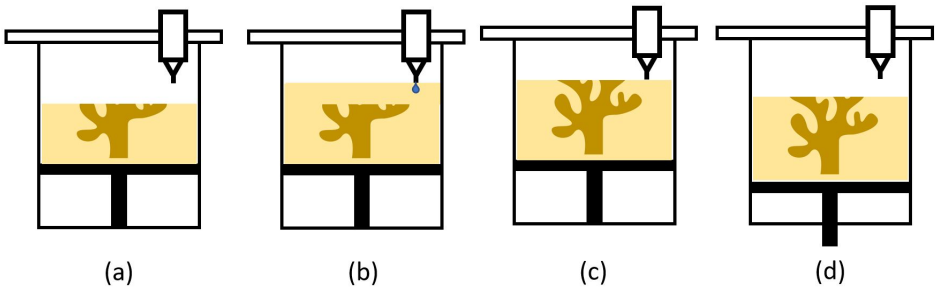

Figure B.1: Figure depicting the different steps per layer. (a) the material is lowered, creating space for new dry material, (b) new material being deposited on the top layer, (c) the nozzle precisely deposited water at the area of interest, (d) the bottom is lowered, so the process can be repeated from (a).

3. After the printer is done with printing the last layer, the print is ready. A stainless steel box filled with material, both dry and wet, is left over. This box needs to be placed in a closed off space, which is regulated to a specific temperature of 25 to 28 degrees Celsius. The box needs to be placed in this warm climate for at least 12 hours depending on the material, so that the material that has reacted with the water hardens out. After the material has hardened out in

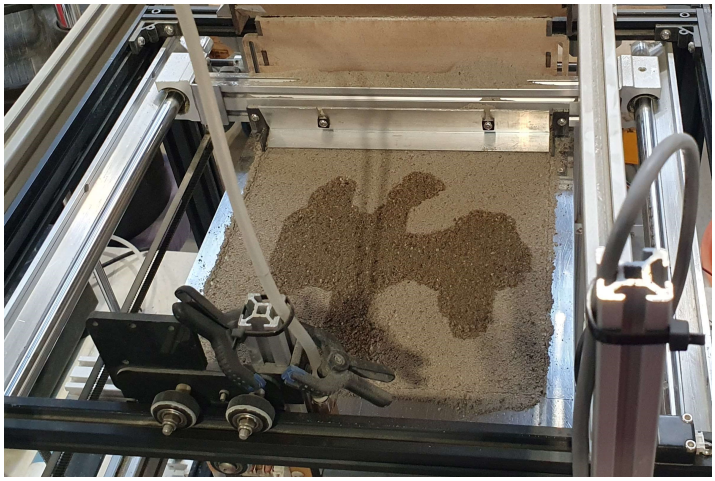

Figure B.2: Printing process showing one layer of water deposited in the specific shape.

the warm space, it can be taken out and the cleaning process can begin. The stainless steel box includes material that has hardened and material that has not reacted (with the water). With brushes and tools, the unused dry material is wiped of until only the hard concrete remains. Figure B.3 shows what this process looks like.

(a) *(b)* *(c)*

Figure B.3: Pictures depicting the result of the cleaning process of the structures from beginning (a) to end (c).

4. After the print is cleaned and only the hardened concrete shape is remaining, the structure needs to be placed in water. This is necessary for the concrete to harden out to its final strength. The structure needs to remain for 5 days in water. After the five days have past, the structures are ready to be used for its specific use.

Appendix C | Test cases

In Table C.1 an overview of all the test conditions that have been performed in this study can be found.

Test number	R_c [m]	H_s [m]	T_p [s]	Breaking	Structure	Reef lay-out
1	0.15	0.05	2.5	NB	C0	empty flume
2	0.15	0.05	2.5	NB	D1	RL4-D1
3	0.15	0.05	2.5	NB	D2	RL4-D2
4	0.15	0.05	2.5	NB	C1	RL4-C1
5	0.15	0.05	5.0	NB	C0	empty flume
6	0.15	0.05	5.0	NB	C1	RL4-C1
7	0.15	0.05	5.0	NB	D1	RL4-D1
8	0.15	0.05	5.0	NB	D2	RL4-D2
9	0.15	0.05	5.0	NB	D1 & D2	RL8-D12-A
10	0.15	0.05	5.0	NB	D1 & D2	RL8-D12-B
11	0.15	0.05	5.0	NB	D1 & D2	RL8-D12-C
12	0.15	0.20	2.5	B	C0	empty flume
13	0.15	0.20	2.5	B	D2	RL1-D2
14	0.15	0.20	2.5	B	D2	RL4-D2
15	0.2	0.05	5.0	NB	C0	empty flume
16	0.2	0.05	5.0	NB	D1	RL4-D1
17	0.2	0.05	5.0	NB	D2	RL4-D2
18	0.2	0.05	5.0	NB	C1	RL4-C1
19	0.25	0.05	2.5	NB	C0	empty flume
20	0.25	0.05	2.5	NB	D1	RL4-D1
21	0.25	0.05	2.5	NB	D2	RL4-D2
22	0.25	0.05	2.5	NB	C1	RL4-C1
23	0.25	0.05	4.0	NB	C0	empty flume
24	0.25	0.05	4.0	NB	D1	RL4-D1
25	0.25	0.05	4.0	NB	D2	RL4-D2
26	0.25	0.05	4.0	NB	C1	RL4-C1
27	0.25	0.05	5.0	NB	C0	empty flume
28	0.25	0.05	5.0	NB	D1	RL4-D1
29	0.25	0.05	5.0	NB	D2	RL4-D2
30	0.25	0.05	5.0	NB	C1	RL4-C1
31	0.25	0.075	2.5	NB	C0	empty flume
32	0.25	0.075	2.5	NB	D1	RL4-D1
33	0.25	0.075	2.5	NB	D2	RL4-D2
34	0.25	0.075	2.5	NB	C1	RL4-C1
35	0.25	0.10	2.5	NB	C0	empty flume
36	0.25	0.10	2.5	NB	D1	RL4-D1
37	0.25	0.10	2.5	NB	D2	RL1-D2
38	0.25	0.10	2.5	NB	D2	RL2-D2
39	0.25	0.10	2.5	NB	D2	RL3-D2

Test number	R_c [m]	H_s [m]	T_p [s]	Breaking	Structure	Reef lay-out
40	0.25	0.10	2.5	NB	D2	RL4-D2
41	0.25	0.10	2.5	NB	C1	RL4-C1
42	0.25	0.10	2.5	NB	D1 & D2	RL8-D12-A
43	0.25	0.10	2.5	NB	D1 & D2	RL8-D12-B
44	0.25	0.10	2.5	NB	D1 & D2	RL8-D12-C
45	0.25	0.22	2.5	B	C0	empty flume
46	0.25	0.22	2.5	B	D2	RL1-D2,
47	0.25	0.22	2.5	B	D2	RL4-D2,

Table C.1: Overview of the wave conditions for all test cases as applied in the steering file for the wave paddle, with a total of 47 tests. Crest submergence: R_c, Significant wave height H_s, peak period T_p, structure C0: empty flume, D1: design 1, D2: design 2, C1: cubes

Appendix D | Signal disturbance

Upon analysing the surface elevation time series obtained from all the wave gauges, perturbations were found in some specific cases. In this Appendix more detail about this is given.

The surface elevation time series were analysed for each wave gauge, and when plotting the time series corresponding to the wave gauge group at location 3, so WHM11, WHM12, WHM93 and WHM13, it was discovered that the signal of WHM13 showed unexpected deviations compared to the other three wave gauges positioned nearby. Figure D.1 shows what these signal irregularities looked like. The figure also demonstrates that the signal of the other three wave gauges do not show abnormalities.

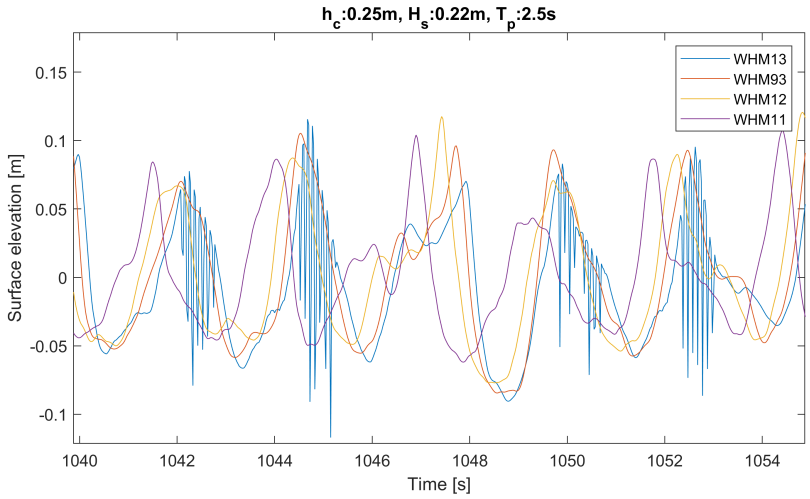

Figure D.1: Water surface elevation time series of the group of four wave gauges located at location 3: WHM11, WHM12, WHM93, WHM13. Only showing a short time range. The signals are obtained from the empty flume test case with wave condition label h80H22T25

The amplitude of the vibrations is of the same magnitude as the 'undisturbed' wave amplitude, as can be seen in the figure. This indicates that these vibration cannot be explained by a small movement of the probe due to the wave impact. If this would have been the case, the amplitude of the vibration would be expected to be much lower as well as more wave gauges would show the same kind of vibration in the signal, however this is clearly not the case. Therefore this disturbed signal is most likely a result of a defective wave gauge.

After carefully checking the surface elevation time series of each wave gauge and test case, it was found that only one wave gauge was showing results including the above named perturbations. This was the wave gauge labelled as WHM13 (Figure 3.2). This wave gauge is the last wave gauge, or the wave gauge located furthest away from the wave maker. This gauge was not used in the data analysis part of this study, because the collocated decomposition technique was used to extract incoming and reflected waves, which was possible at WHM91, WHM92 and WHM93 only.

It was also found that the irregular signal was only present for specific wave conditions only, namely h80H22T25, h70H22T25 and h80H10T25. These test cases correspond to wave conditions with the 3 largest significant wave heights. The wave gauge was apparently prone to large waves which disturbed the measurement for that specific wave gauge.